

EDITORIAL

Taking root (p. 01-03)

IN-DEPTH REVIEW

Ulnar peripheral tears of the triangular fibrocartilage complex: multiplanar approach of injury patterns with focus on CT arthrography (p. 04-16)

FULL RESEARCH ARTICLES

Validation of the Ultrasound Neck Node Reporting and Data System (UNN-RADS) for predicting lymph node metastases in thyroid cancer (p. 17-26)

Paramagnetic rim lesions on 1.5T and 3.0T MRI in Mexican patients with multiple sclerosis (p. 27-35)

A descending enhancement pattern on CEM is associated with invasive breast cancer: the first Mexican experience (p. 36-44)

US duplex findings in chronic venous insufficiency of the lower limbs in 500 Mexican patients (p. 45-55)

BRIEF RESEARCH ARTICLE

Unifocal, multifocal, or multicentric breast cancer distribution patterns on multiplanar breast MRI: a technical note (p. 56-61)

CASE REPORT

US findings of uterine and ovarian herniation through the Nuck canal: a case report (p. 62-65)

IMAGES IN RADIOLOGY

CTA findings in chronic coarctation of the aorta (p. 66-68)



PERMANER

www.permaner.com

Official Journal of the



FEDERACIÓN MEXICANA DE RADIOLOGÍA E IMAGEN, A.C

Carestream

Meet the
NEW
member
of the family

DRX-Rise

It's amazing!



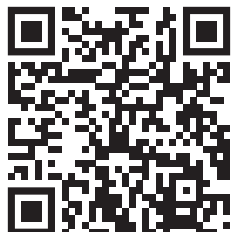
We have **EQUIPMENT** for all **YOUR NEEDS**



Right for **Today...** Ready for *Tomorrow.*



Scan the QR
and visit
the Virtual Hospital



A simple step to digital radiography



i550z

Digital Radiography Systems



+52 686-568-1904

WhatsApp - +520686-606-4076

www.laicoinfo.com

Mexicali, BC Mexico



DDR

DYNAMIC DIGITAL RADIOGRAPHY

Dynamic Digital Radiology (DDR) enables clinicians to observe the dynamic motion of anatomical structures over time, enhancing diagnostic capabilities. DDR provides a view of anatomy in motion, with a large field of view and low radiation dose.

DDR is a promising platform for AI (Artificial Intelligence) applications. DDR is not fluoroscopy;



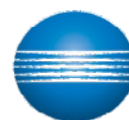
DDR is X-ray that Moves!

xraythatmoves.com

exa

Scalable and customizable to the exact requirements of your practice, our leading IT solutions manage medical imaging and patient data right across the healthcare spectrum, including PACS, RIS, specialty viewers and Billing.

Our Healthcare IT software solutions are packed with the all the speed, security and flexibility you need, anytime/anywhere viewing and a single integrated database across all modules.



KONICA MINOLTA

contact us: kmhalatinoamerica@konicaminolta.com



Journal of the Mexican Federation of Radiology and Imaging

J Mex Fed Radiol Imaging

Volume 3. Number 1, January-March 2024

ISSN: 2938-1215

eISSN: 2696-8444

The *Journal of the Mexican Federation of Radiology and Imaging* (JMEXFRI) is the official journal of the Federación Mexicana de Radiología e Imagen. The aim of the journal is to disseminate scientific knowledge and technological developments for innovation in diagnostic and therapeutic radiology with original articles on basic and clinical aspects of modern radiology in an international context with global impact. JMEXFRI is published in American English with 4 issues per year (print and online) and the first issue was published in the first quarter of 2022. Articles undergo a rigorous, double-blind peer-review process. Publication of articles in JMEXFRI is free of charge and all published articles are open access.

The journal publishes the following types of manuscripts: *Full Research Article, Pictorial Essay, Brief Research Article, Technical Note, In-Depth Review, Case Report, Images in Radiology, and Editorial.*

EDITORIAL BOARD

EDITOR-IN-CHIEF

Mauricio Figueroa-Sanchez, M.D.

Department of Radiology, Antiguo Hospital Civil de Guadalajara "Fray Antonio Alcalde", Guadalajara, Jal., Mexico

ASSOCIATE EDITORS

Gerardo E. Ornelas-Cortinas, M.D.

*Centro Universitario de Imagen Diagnostica, Hospital Universitario
"Dr. Jose E. Gonzalez", Monterrey, N.L., Mexico*

Araceli Cue-Castro, M.D.

*Department of Computed Tomography, Hospital General
"Dr. Enrique Cabrera" SEDESA, Mexico City, Mexico*

Oscar A. Chavez-Barba, M.D.

*Department of Radiology,
Antiguo Hospital Civil de Guadalajara "Fray Antonio Alcalde",
Guadalajara, Jal., Mexico*

Ana M. Contreras-Navarro, M.D., M.Sc., Ph.D.

*Scientific Writing Workshop, JMEXFRI,
Zapopan, Jal., Mexico*

David Garza-Cruz, M.D.

*Department of Radiology, Hospital Angeles,
Torreon, Coah., Mexico*

J. Mario Bernal-Ramirez, M.D.

*Department of Medical Clinics, Centro Universitario de
Ciencias de la Salud, Universidad de Guadalajara,
Guadalajara, Jal., Mexico*

SCIENTIFIC TRANSLATOR EDITOR

Sergio Lozano-Rodriguez, M.D.

Research Office of the Vice Dean, Hospital Universitario "Dr. Jose E. Gonzalez", Monterrey, N.L., Mexico

BIostatISTICS ADVISER

Cesar N. Cristancho-Rojas, M.D., M.Sc.

School of Public Health, Oregon Health & Science University, Portland, OR., USA

DESIGN ADVISER

Jorge Mendez-Palacios, B.Sc.

Design Area, JMEXFRI. Zapopan, Jal., Mexico

NATIONAL EDITORIAL BOARD

HEAD AND NECK RADIOLOGY

Mario A. Campos-Coy, M.D.

*Centro Universitario de Imagen Diagnostica,
Hospital Universitario "Dr. Jose E. Gonzalez",
Monterrey, N.L., Mexico*

Eduardo D. Sarda-Inman, M.D.

*Diagnostico Especializado por Imagen,
Zapopan, Jal., Mexico*

GASTROINTESTINAL RADIOLOGY

Araceli Cue-Castro, M.D.

*Department of Computed Tomography,
Hospital General "Dr. Enrique Cabrera" SEDESA,
Mexico City, Mexico*

Adrian Negreros-Osuna, M.D., Ph.D.

*Departamento de Radiologia,
Hospital Regional ISSSTE Monterrey,
Monterrey, N.L., Mexico*

Oscar A. Chavez-Barba, M.D.

*Department of Radiology,
Antiguo Hospital Civil de Guadalajara
"Fray Antonio Alcade",
Guadalajara, Jal., Mexico*

OBSTETRIC AND GYNECOLOGIC RADIOLOGY

Dante R. Casale-Menier, M.D.

*Department of Radiology and Imaging,
Hospital Angeles,
Ciudad Juarez, Chih., Mexico*

Roberto J. Carrales-Cuellar, M.D.

*Department of Ecographic Diagnosis,
Radiologia Especializada,
Guadalajara, Jal., Mexico*

BREAST RADIOLOGY

David F. Perez-Montemayor, M.D.

*General Direction,
Centro de Imagenologia Integral IMAX,
Tampico, Tamps., Mexico*

Beatriz Gonzalez-Ulloa, M.D.

*Department of Breast Imaging,
Diagnostico Especializado por Imagen,
Guadalajara, Jal., Mexico*

Margarita L. Garza-Montemayor, M.D.

*Departamento de Imagen Diagnostica,
Centro de Cancer de Mama,
Hospital Zambrano Hellion, Tec Salud,
Monterrey, N.L., Mexico*

Karla M. Nuñez-Barragan, M.D.

*Women's Imaging Department,
Doctors Hospital East Auna
Monterrey, N. L., Mexico*

NUCLEAR AND MOLECULAR MEDICINE

Hugo E. Solis-Lara, M.D.

*Centro de Imagen Molecular,
Hospital Christus Muguerza Alta Especialidad,
Monterrey, N.L., Mexico*

NEURORADIOLOGY

Jorge Paz-Gutierrez, M.D.

*Department of Magnetic Resonance,
Centro Medico Puerta de Hierro,
Zapopan, Jal., Mexico*

Azalea Garza-Baez, M.D.

*Department of Radiology and Imaging,
Hospital Zambrano Hellion,
Tecnologico de Monterrey,
Monterrey, N.L., Mexico*

Perla M. Salgado-Lujambio, M.D.

*Direccion de Enseñanza,
Instituto Nacional de Neurologia y
Neurocirugia "Manuel Velasco Suarez"
Mexico City, Mexico*

PEDIATRIC RADIOLOGY

Aida Perez-Lara, M.D.

*Department of Radiology, Hospital Español,
Mexico City, Mexico*

MUSCULOSKELETAL RADIOLOGY

Oscar A. Chavez-Barba, M.D.

*Department of Radiology, Antiguo Hospital Civil
de Guadalajara "Fray Antonio Alcade",
Guadalajara, Jal., Mexico*

J. Francisco Diaz-Fernandez, M.D.

*Department of Radiology,
Hospital General "Agustin O'Horan",
Merida, Yuc., Mexico*

CHEST AND CARDIOVASCULAR RADIOLOGY

Sergio A. Criales-Vera, M.D.

*Department of Radiology and Imaging,
Instituto Nacional de Cardiologia "Ignacio Chavez",
Mexico City, Mexico*

Harold Goerne, M.D.

*Department of Radiology, Hospital de Pediatria,
Instituto Mexicano del Seguro Social,
Guadalajara, Jal., Mexico*

Luis F. Alva-Lopez, M.D.

*Department of Radiology, Hospital Medica Sur,
Mexico City, Mexico*

GENITOURINARY RADIOLOGY

Sergio B. Peregrina-Gonzalez, M.D.

*Consultorio de Imagen,
Guadalajara, Jal., Mexico*

Araceli Cue-Castro, M.D.

*Department of Computed Tomography,
Hospital General "Dr. Enrique Cabrera" SEDESA,
Mexico City, Mexico*

Adrian Negreros-Osuna, M.D.

*Departamento de Radiologia,
Hospital Regional ISSSTE Monterrey,
Monterrey, N.L., Mexico*

Benjamin Conde-Castro, M.D.

*Faculty of Medicine,
Universidad Nacional Autónoma de Mexico,
Mexico City, Mexico*

ULTRASOUND

Rosa M. Alanis-Salazar, M.D.

*Departamento de Radiologia, UMF Guadalupe, ISSSTE,
Monterrey, NL., Mexico*

Victor M. Rodriguez-Peralta, M.D.

*Department of Radiology,
Fundacion de Cancer de Mama (FUCAM),
Oaxaca, Oax., Mexico*

David Garza-Cruz, M.D.

*Department of Radiology, Hospital Angeles,
Torreon, Coah., Mexico*

Manuel Hernandez-Cruz, M.D.

*Area de Ultrasonido,
Unidad de Ultrasonido Diagnostico,
Puebla, Pue. Mexico*

VASCULAR AND INTERVENTIONAL RADIOLOGY

Guillermo Elizondo-Riojas, M.D., Ph.D.

*Centro Universitario de Imagen Diagnostica,
Hospital Universitario "Dr. Jose E. Gonzalez",
Monterrey, N.L., Mexico*

Raul A. De Luna-Vega, M.D.

*Centro Universitario de Imagen Diagnostica,
Hospital Universitario "Dr. Jose E. Gonzalez",
Monterrey, N.L., Mexico*

ARTIFICIAL INTELLIGENCE

Guillermo Elizondo-Riojas, M.D., Ph.D.

*Centro Universitario de Imagen Diagnostica,
Hospital Universitario "Dr. Jose E. Gonzalez",
Monterrey, N.L., Mexico*

Adrian Negreros-Osuna, M.D.

*Departamento de Radiología,
Hospital Regional ISSSTE Monterrey,
Monterrey, N.L., Mexico*

J. Mario Bernal-Ramirez, M.D.

*Department of Medical Clinics,
Centro Universitario de Ciencias de la Salud,
Universidad de Guadalajara,
Guadalajara, Jal., Mexico*

Benjamin Conde-Castro, M.D.

*Faculty of Medicine,
Universidad Nacional Autonoma de México,
Mexico City, Mexico*

JUNIOR EDITORIAL BOARD

J. Mario Bernal-Ramirez, M.D.

*Department of Medical Clinics,
Centro Universitario de Ciencias de la Salud,
Universidad de Guadalajara,
Guadalajara, Jal., Mexico*

Ana K. Luna-Marroquin, M.D.

*Centro Universitario de Imagen Diagnostica,
Hospital Universitario "Dr. Jose E. Gonzalez",
Monterrey, N.L., Mexico*

M. Lourdes Garcia-Colmenero, M.D.

*Departamento de Radiologia,
Hospital Angeles Pedregal,
Ciudad de Mexico, Mexico*

Xavier A. Gonzalez-Ballesteros, M.D.

*Departamento de Radiologia,
Hospital San Angel Inn Universidad,
Ciudad de Mexico, Mexico*

Adriana Parada-Gallardo, M.D.

*Department of Radiology,
Hospital General de Zapopan,
Zapopan, Jal., Mexico*

INTERNATIONAL EDITORIAL BOARD

HEAD AND NECK RADIOLOGY

Richard H. Wiggins, M.D.

*Department of Radiology and Imaging Sciences, School
of Medicine, University of Utah,
Salt Lake City, UT., USA*

Amy Juliano, M.D.

*Department of Radiology,
Massachusetts Eye and Ear,
Harvard Medical School,
Boston, MA., USA*

GASTROINTESTINAL RADIOLOGY

Jorge A. Soto, M.D.

*Department of Radiology, Boston Medical Center,
Boston, MA., USA*

Jorge Elias Jr. Ph.D.

*Departamento de Imagenes Medicas,
Oncologia e Hematologia,
Faculdade de Medicina Ribeirao Preto,
Universidade Sao Paulo Ribeirao Preto,
Sao Paolo, Brazil*

Valdair F. Muglia, M.D.

*Faculdade de Medicina de Ribeirão Preto,
Universidade de São Paulo, Ribeirão Preto,
Sao Paolo, Brazil*

Carlo Catalano, M.D.

*Department of Diagnostic Radiology
La Sapienza University of Rome
Rome, Italy*

OBSTETRIC AND GYNECOLOGIC RADIOLOGY

Luciana Pardini Chamie, M.D., Ph.D.
*Centro de Diagnostico Ultrasonografico
Especializado en Imagen de la Mujer,
Sao Paulo, Brazil*

BREAST RADIOLOGY

Javier Romero-Enciso, M.D.
*Department of Radiology,
Fundacion Santa Fe,
Bogota, Colombia*

NUCLEAR AND MOLECULAR MEDICINE

Begoña Martinez-Sanchis, M.D.
*Department of Nuclear Medicine,
Hospital Universitario y Politecnico La Fe,
Valencia, Spain*

Cesar N. Cristancho-Rojas, M.D., M.Sc.
*School of Public Health,
Oregon Health & Science University,
Portland, OR., USA*

NEURORADIOLOGY

Roy F. Riascos-Castaneda, M.D.
*Department of Radiology and Neurosurgery,
Memorial Hermann Hospital System,
Houston, TX., USA*

Rafael Rojas-Jasso, M.D.
*Department of Radiology, Beth Israel,
Deaconess Medical Center,
Boston, MA., USA*

Henrique Carrete Jr., M.D., Ph.D.
*Department of Diagnostic Imaging,
Universidade de Sao Paulo,
Sao Paulo, Brazil*

Carlos Torres, M.D.
*Department of Diagnostic Imaging,
The Ottawa Hospital,
Ottawa, Canada*

MUSCULOSKELETAL RADIOLOGY

Javier Fernandez-Jara, M.D.
*Department of Radiology,
Hospital Universitario Sanitas La Zarzuela,
Madrid, Spain*

Jose Luis del Cura, M.D.
*Radiodiagnosis Service,
Hospital Universitario Donostia,
San Sebastian-Donostia, Spain*

Diego F. Lemos, M.D.
*Department of Radiology,
University of Vermont Medical Center,
Burlington, VT, USA*

PEDIATRIC RADIOLOGY

George Bisset, M.D.
*Department of Radiology, Children's Hospital
Pennsylvania, PA., USA*

Sara Reis Teixeira, M.D., Ph.D.
*Department of Radiology, Children's Hospital
Pennsylvania, PA. USA*

CHEST AND CARDIOVASCULAR RADIOLOGY

Fernando R. Gutierrez, M.D.
*Department of Radiology and Cardiothoracic Imaging,
The Mallinckrodt Institute of Radiology,
St. Louis, MO., USA*

Jorge Carrillo-Bayona, M.D.
*Department of Radiology,
Hospital Universitario Mayor,
Bogota, Colombia*

Carlos S. Restrepo, M.D.
*Department of Cardiothoracic Radiology,
Texas University,
San Antonio, TX., USA*

Sebastian Rossini, M.D.

*Department of Radiology,
Instituto Radiologico Mater Dei,
Buenos Aires, Argentina*

Santiago Martinez-Jimenez, M.D.
*Department of Radiology,
Saint Luke's Hospital of Kansas City,
Kansas City, KS., USA*

L. Antonio Sosa-Lozano, M.D.
*Department of Cardiothoracic Radiology,
Medical College of Wisconsin,
Milwaukee, WI., USA*

GENITOURINARY RADIOLOGY

Daniela Stoisa, M.D.
*Department of Radiology, Diagnostico Medico Oroño,
Rosario, Santa Fe, Argentina*

Valdair F. Muglia, M.D.
*Faculdade de Medicina de Ribeirao Preto,
Universidade de Sao Paulo Ribeirao Preto,
Sao Paulo, Brazil*

ULTRASOUND

Edward G. Grant, M.D.
*Department of Radiology, USC Norris Cancer Center,
Los Angeles, CA., USA*

Juan P. Niedmann-Espinosa, M.D.
*Department of Ecotomography,
Clinica Alemana de Santiago,
Santiago de Chile, Chile*

VASCULAR AND INTERVENTIONAL RADIOLOGY

Manuel Cifrian-Perez, M.D., Ph.D.
*Imaging Clinic Department,
Hospital Universitario y Politecnico La Fe,
Valencia, Spain*

ARTIFICIAL INTELLIGENCE

Leonor Cerda-Alberich, Ph.D.
*Imaging Clinic Department,
Hospital Universitario y Politecnico La Fe,
Valencia, Spain*

Felipe Campos Kitamura, M.D., Ph.D.
*Dasalnova, Dasa,
Sao Paulo, Brazil*

GRAPHICAL ABSTRACTS COMMITTEE

Oscar A. Chavez-Barba, M.D.
*Department of Radiology,
Antiguo Hospital Civil de Guadalajara
"Fray Antonio Alcalde",
Guadalajara, Jal., Mexico*

Adriana Parada-Gallardo, M.D.
*Department of Radiology,
Hospital General de Zapopan,
Zapopan, Jal., Mexico*

J.M. Ignacio Lopez-Mendez, M.D.
*Department of Radiology and Imaging,
Hospital de Especialidades, CMNO
Instituto Mexicano del Seguro Social,
Guadalajara, Jal., Mexico*

Juan Pablo Lopez-Gutierrez, M.D.
*Department of Radiology and Imaging,
Hospital General de Zona 3,
Instituto Mexicano del Seguro Social
Aguascalientes, Ags., Mexico*

Gerardo Llamas-Linares, M.D.
*Centro Universitario de Imagen Diagnostica,
Hospital Universitario "Dr. Jose E. Gonzalez",
Monterrey, N.L., Mexico*

Alejandra I. Castillo-Cervantes, M.D.
*Centro Universitario de Imagen Diagnostica,
Hospital Universitario "Dr. Jose E. Gonzalez",
Monterrey, N.L., Mexico*

A. Sofia Sanchez-Gomez, M.D.

*Department of Radiology,
Grupo RIO Centro Integral de Diagnostico Medico.
Guadalajara, Jal., Mexico*

SOCIAL MEDIA COMMITTEE

Guillermo Elizondo-Riojas, M.D., Ph.D.
*Centro Universitario de Imagen Diagnostica,
Hospital Universitario "Dr. Jose E. Gonzalez",
Monterrey, N.L., Mexico*

Oscar A. Chavez-Barba, M.D.
*Department of Radiology,
Antiguo Hospital Civil de Guadalajara
"Fray Antonio Alcalde",
Guadalajara, Jal., Mexico*

J. Mario Bernal-Ramirez, M.D.
*Department of Medical Clinics,
Centro Universitario de Ciencias de la Salud,
Universidad de Guadalajara,
Guadalajara, Jal., Mexico*

Adriana Parada-Gallardo, M.D.
*Department of Radiology,
Hospital General de Zapopan,
Zapopan, Jal., Mexico*

RADIOLOGICAL AND CLINICAL CORRELATION BOARD

GASTROENTEROLOGY

Linda E. Muñoz-Espinosa, M.D., Ph.D.
*Liver Unit, Hospital Universitario
"Dr. Jose E. Gonzalez",
Monterrey, N.L., Mexico*

David Marti-Aguado, M.D., Ph.D.
*Servicio Medicina Digestiva,
Hospital Clinico Universitario,
Valencia, Spain*

GASTROINTESTINAL AND GENERAL SURGERY

Carlos Nuño-Guzman, M.D., M.Sc.
*Department of Surgery,
Antiguo Hospital Civil de Guadalajara
"Fray Antonio Alcalde",
Guadalajara, Jal., Mexico*

OBSTETRICS AND GINECOLOGY

Sergio Fajardo-Dueñas, M.D., M.Sc.
*Division of Obstetrics and Gynecology,
Nuevo Hospital Civil de Guadalajara,
Guadalajara, Jal., Mexico*

NEUROLOGY

Jose L. Ruiz-Sandoval, M.D., M.Sc.
*Department of Neurology,
Antiguo Hospital Civil de Guadalajara
"Fray Antonio Alcalde",
Guadalajara, Jal., Mexico*

RHEUMATOLOGY

Monica Vazquez del Mercado-Espinosa, M.D., Ph.D.
*Division of Medicine,
Nuevo Hospital Civil de Guadalajara,
Guadalajara, Jal., Mexico*

CARDIOLOGY-PNEUMOLOGY

Jose M. Hernandez, M.D.
*Department of Ecocardiography, Doctors Hospital,
Monterrey, N.L., Mexico*

PATHOLOGICAL ANATOMY

Marco A. Ponce-Camacho, M.D., Ph.D.
*Department of Cytopathology, Doctors Hospital,
Monterrey, N.L., Mexico*

ENDOCRINOLOGY

Jesus Zacarias Villarreal-Perez, M.D.
Department of Endocrinology,
Hospital Universitario "Dr. Jose E. Gonzalez",
Monterrey, N.L., Mexico

HEMATOLOGY

Carlos R. Best-Aguilera, M.D.
Department of Hematology,
Hospital General de Occidente. Secretaria de Salud
Zapopan, Jal., Mexico

PEDIATRIC NEUROLOGY

Daniel Perez-Rulfo Ibarra, M.D., Ph.D.
Departamento de Pediatría,
Antiguo Hospital Civil de Guadalajara
"Fray Antonio Alcalde",
Guadalajara, Jal., Mexico

GYNECOLOGICAL UROLOGY

Patricia I. Velazquez-Castellanos, M.D., M.Sc.
Department of Gynecology and Obstetrics,
Antiguo Hospital Civil de Guadalajara
"Fray Antonio Alcalde",
Guadalajara. Jal., Mexico



Original papers should be deposited in their electronic version through the following URL:

<https://publisher.jmexfri.permanyer.com>



PERMANYER
www.permanyer.com

Permalyer Mexico

Temistocles, 315
Col. Polanco, Del. Miguel Hidalgo
11560 Ciudad de Mexico
mexico@permalyer.com

Permalyer

Mallorca, 310 – Barcelona (Cataluña), España
permalyer@permalyer.com

ISSN: 2696-8444

Ref.: 10130AMEX241



www.permalyer.com

Reproductions for commercial purposes:

Without the prior written consent of the publisher, no part of this publication may be reproduced, stored in a retrievable medium or transmitted, in any form or by any means, electronic, mechanical, photocopying, recording or otherwise, for commercial purposes.

Journal of the Mexican Federation of Radiology and Imaging is an open access publication with the Creative Commons license
CC BY-NC-ND (<http://creativecommons.org/licenses/by-nc-nd/4.0/>).

The opinions, findings, and conclusions are those of the authors. The editors and publisher are not responsible
and shall not be liable for the contents published in the journal.

© 2024 Federacion Mexicana de Radiologia e Imagen, AC. Published by Permalyer.

Taking root

Sanjeev Bhalla^{id*} and Fernando Gutierrez^{id}

Cardiothoracic Imaging Section, Mallinckrodt Institute of Radiology, Washington University School of Medicine, St Louis, Missouri, United States of America

"It is in the roots, not the branches, that a tree has greatest strength"

Matshona Dhliwayo

A few years ago, we were consulted on a nodule in a very prominent person who had a new diagnosis of breast cancer. The nodule had a smooth border with macroscopic fat and popcorn calcification. In other words, it was a classic hamartoma. But computer-aided detection using artificial intelligence had flagged the nodule. It showed enhancement on dynamic contrast CT, which was also concerning to the original reader. Maybe further imaging was warranted after all this was an important patient. Despite our certainty in diagnosis, the team decided to pursue an FDG-PET CT, which was equivocal. Kurtosis data were also equivocal. Amidst the cloud of doubt that had formed, anxiety increased. Eventually, the nodule was resected. The original reader later called us to inform that the nodule on final pathology was indeed a hamartoma. They seemed surprised.

This case is one we often reflect on in this time of expanding diagnostic techniques and rapid change in our specialty, especially in the era of artificial intelligence. Everyone seems to be looking for the magic bullet. Maybe dual-energy CT or textural analysis could have prevented surgery? Probably not. What if we had used more artificial intelligence? The key in this case would have been confidence in the classic CT findings of this fairly common nodule. An approach to the solitary nodule based on experience, science, and observation is what could have spared the patient her surgery.

Over the past decades, we have seen the rapid evolution of cardiothoracic imaging. Technology has changed exponentially. When CT was first introduced at the Mallinckrodt Institute of Radiology, the cardiothoracic imaging section was simply the chest section under the leadership of our friend and mentor, Stuart Sagel. At that time, a chest CT took over 30 min, and the images took hours to be reconstructed. Stuart infused a unique ability in the section and culture to embrace new technology but in the context of healthy skepticism and a solid educational foundation. We remember showing him one of the first pulmonary embolism protocols. We had been so focused on fine reconstructions that we missed the embolism. Stuart did not. He reminded us that, while we were focused on making pretty pictures, he had remained steadfast in reading the images. More sophisticated acquisitions and analyses of the image have also been achieved. Yet, the approach has remained fairly constant.

A strong approach, rooted in the experience of those who have practiced before us, allows for a meaningful integration of new technology. One of the questions that always arises in our training program of over 70 Radiology residents is how to develop the approach. This approach comes from four key paths. The first path includes mentored observations of many examinations. The ability to ask questions and understand the thought processes of those who have preceded us in the specialty allows us to lay the foundations of an approach. Interpretation of cases built on that foundation allows for continued refinement and iteration of the

***Corresponding author:**

Sanjeev Bhalla
E-mail: bhallas@wustl.edu

Received for publication: 07-01-2024

Accepted for publication: 08-01-2024

DOI: 10.24875/JMeXFRI.M24000066

Available online: 22-03-2024

J Mex Fed Radiol Imaging. 2024;3(1):1-3

www.JMeXFRI.com

2696-8444 / © 2024 Federación Mexicana de Radiología e Imagen, A.C. Published by Permanyer. This is an open access article under the CC BY-NC-ND (<https://creativecommons.org/licenses/by-nc-nd/4.0/>).

approach, making it individualized while simultaneously being rooted in the past. This volume must take two forms: daily clinical practice, which is more closely observed, and on-call volume, which allows for longer periods of questions and exploration. Both volumes are so important in allowing a trainee to understand how to approach clinical cases and when to ask for help.

The approach is also built on understanding of the development of critical thinking skills. Sometimes, these critical thinking skills are based on the ability to assess published literature through journal clubs and group discussions. More often, the ability to critically analyze an image is refined by taking unknown cases in front of peers and mentors. In these unknown case conferences, one can learn to deal with the anxiety of confronting an unknown case, while simultaneously having a logical method that allows for a reasonable differential diagnosis and management plan. In many parts of the world, there has been an increase in trying to avoid unknown case conferences in public. The potential for embarrassment is high, and gaps in knowledge may be made public. However, we believe that acquiring this skill is necessary to build a strong foundational approach and does not have to be embarrassing. More often, we have observed that a skilled case taker is one of the greatest motivations for their peers and junior colleagues. It is also a critical part of what we all do as radiologists. This is an area where we have continually been surprised and pleased by what we have observed in the Latin American training programs during our visits. We are struck by the eagerness of trainees to participate in, taking unknown cases with their own faculty, as well as with visiting faculty. Although this approach may seem old-fashioned, it plays a crucial role in the development of critical thinking in radiology. In fact, in an era when oral board examinations have faded, organizations are revisiting how they can use modern technology to bring back this assessment method.

A third key element of foundation building relies on understanding the published literature and the clinical experience of experts in the specialty. This is most easily achieved by attending didactic conferences, given by the experts. Whether it be in the form of a noon conference, web-based sessions, or a national meeting, these nuggets can be very helpful for rapidly assimilating a large amount of radiology information. Listening to an expert review, the technical history of CT, for example, allows the listener to cover decades in minutes. Often, these didactic lectures are infused with practical observations and pearls that cannot be

found in any written material. The richness of the oral tradition in disseminating information is thriving within the Latin American community. Through our work with various US radiological societies, we have observed that when a program is offered in Spanish, the programs are often extremely well attended with question-and-answer sessions that may last as long as the original offerings. This great attendance reminds us of the perceived value of these didactic lectures.

The fourth path of foundation building comes from individual creativity. This may be from independent studying of existing materials, research in the specialty, and frankly, playing with the various tools and modalities, at our fingertips. Although it is tempting to believe that knowledge can be acquired only by participation in the clinical arena, one must remember that independent study, especially point-of-care learning, may be critical in bringing the clinical learning to the next level.

Understanding the importance of the experience of prior generations creates the foundation of a strong independent practice, and it also helps level the playing field. We have observed, during our numerous trips to Latin America and in our deep friendships with those who practice in Latin America, that the oral tradition and respect of prior generations are quite strong. Endearing terms such as maestro, professor, and doctorisimo affectionately remind us that the culture is one that values and embraces respect. These traits will allow Latin American radiologists to compete on the world stage and overcome any technological deficits. For newer radiologists, this means that focus in training must be on the four-step approach to radiology and should not solely focus on the newer techniques and technologies. It is easy to focus on what is lacking, but care must be given to appreciate what is present.

This four-step approach allows new technology to be incorporated meaningfully and with fiscal responsibility. This is crucial when each piece of new technology is battling for limited funds. Also, it cannot end when training is completed. We have found that we frequently follow the four paths even as professors who have long completed training. The forms, of course, are slightly different. But, we continually read cases with mentored guidance most often by asking questions of peers who may have had more experience with a given disease or modality. We practice critical thinking by presenting and attending multidisciplinary conferences. We must continually read and study on our own to understand some of the newer technologies. Finally, we find ourselves attending didactic lectures, given by colleagues

at our own institution and by others so that we can hear a well-formed synopsis of years of literature and publication. This continued building on the foundation allows us to understand the role of newer technologies in practice. For example, understanding the findings of pulmonary embolism CT and potential pitfalls allows one to carefully assess whether the added cost and images of dual-energy CT will provide additional value to daily interpretation of pulmonary embolism CT.

It is believed that Picasso once said, “Learn the rules like a pro, so you can break them like an artist.” This very much holds true in radiology. We strongly encourage respect for the foundational approach so that significant breakthroughs can occur. Significant developments can only happen when we have learned the foundational approaches of our specialty. We truly believe that the Latin experience is built on a solid foundation and sets the stage for artistic and meaningful innovation.

Ulnar peripheral tears of the triangular fibrocartilage complex: multiplanar approach of injury patterns with a focus on CT arthrography

Gonzalo A. Serrano-Belmar 

Department of Radiology, Clínica Alemana de Santiago, Vitacura, Chile

ABSTRACT

The triangular fibrocartilage complex (TFCC), specifically the distal radioulnar ligaments (DRULs) are the main stabilizing components of the distal radioulnar joint. These ligaments are formed by superficial and deep fibers that are inserted into the distal ulna in the styloid process and fovea, respectively. Therefore, four arms are inserted into the ulna, two superficial and two deep arms. The deep foveal arms are biomechanically more advantageous in maintaining joint stability. For this reason, determining the injury to these fibers is the most critical parameter to define when planning an eventual surgery. Different forces acting on the distal radioulnar joint stretch each of these DRUL components differently. If the various forces acting on these structures are excessive, it can determine an avulsion of the bone insertion. Which components may tear will depend on the predominant mechanism of injury, magnitude, and direction of the traumatic forces acting on the ulnar wrist. The CT arthrography, in case of an injury, can clearly define which component is involved. The purpose of this review was to demonstrate the detailed description of the different components affected and the tear patterns of peripheral ulnar TFCC that can be defined through a multiplanar approach in CT arthrography. This approach has not been previously exposed in the literature. The various injuries described utilizing the multiplanar approach could lead to a better clinical-radiological correlation and a change in patient management.

Keywords: Triangular fibrocartilage complex. Distal radioulnar ligaments. Deep foveal arms. CT arthrography.

INTRODUCTION

The triangular fibrocartilage complex (TFCC) has seven distinct components: the articular disc, the dorsal and palmar radioulnar ligaments, the ulnocarpal ligaments (ulnolunate and ulnotriquetral), the sub-sheath of the extensor carpi ulnaris tendon (ECU-ss), and the meniscus homologue¹ (Figure 1). Accurate diagnosis of peripheral tears of the TFCC has been a relevant topic in recent years². TFCC injuries are typically categorized

within the Palmer classification³. Palmer 1B lesions correspond to distal avulsions of the proximal or distal lamina. This type of injury is the one that most often goes unnoticed in imaging studies^{4,5}.

Palmer's classification has several limitations. Distal radioulnar ligament (DRUL) injuries are not categorized. Class 1B lesions have not been subclassified, depending on which component is specifically affected^{3,6}. Except for class 1C injuries (ulnocarpal ligament injury), all other peripheral injuries fall within class 1B injuries,

Corresponding author:

Gonzalo A. Serrano-Belmar

E-mail: serrano.gonzo@gmail.com

Received for publication: 08-01-2024

Accepted for publication: 12-01-2024

DOI: 10.24875/JMEXFRI.M24000067

Available online: 22-03-2024

J Mex Fed Radiol Imaging. 2024;3(1):4-16

www.JMEXFRI.com

2696-8444 / © 2024 Federación Mexicana de Radiología e Imagen, A.C. Published by Permanyer. This is an open access article under the CC BY-NC-ND (<https://creativecommons.org/licenses/by-nc-nd/4.0/>).

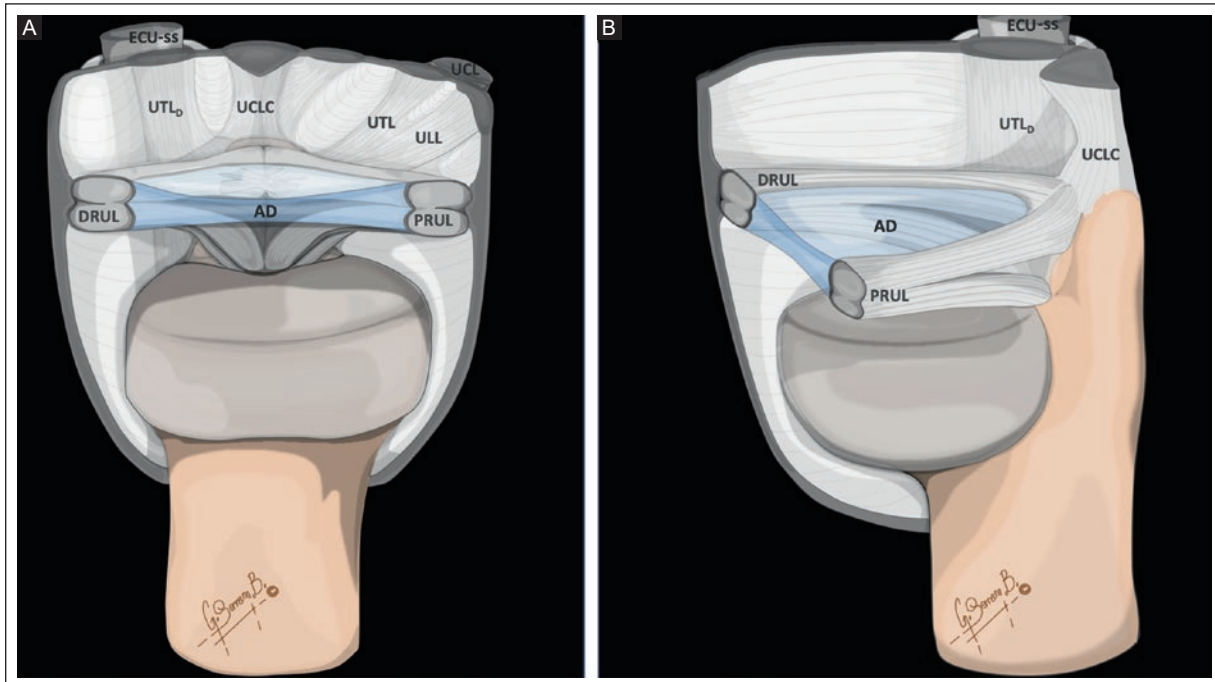


Figure 1. TFCC components. **A and B:** articular disc (AD), dorsal (DRUL), and palmar (PRUL) radioulnar ligaments, ulnocarpal ligaments (ulnolunate [ULL], ulnotriquetral [UTL], and ulnocapitate [UCL]), ECU tendon and sub-sheath (ECU-ss), dorsal ulnotriquetral ligament (UTLd), and meniscus homologue/ulnar collateral complex (UCLC).

TFCC: triangular fibrocartilage complex.

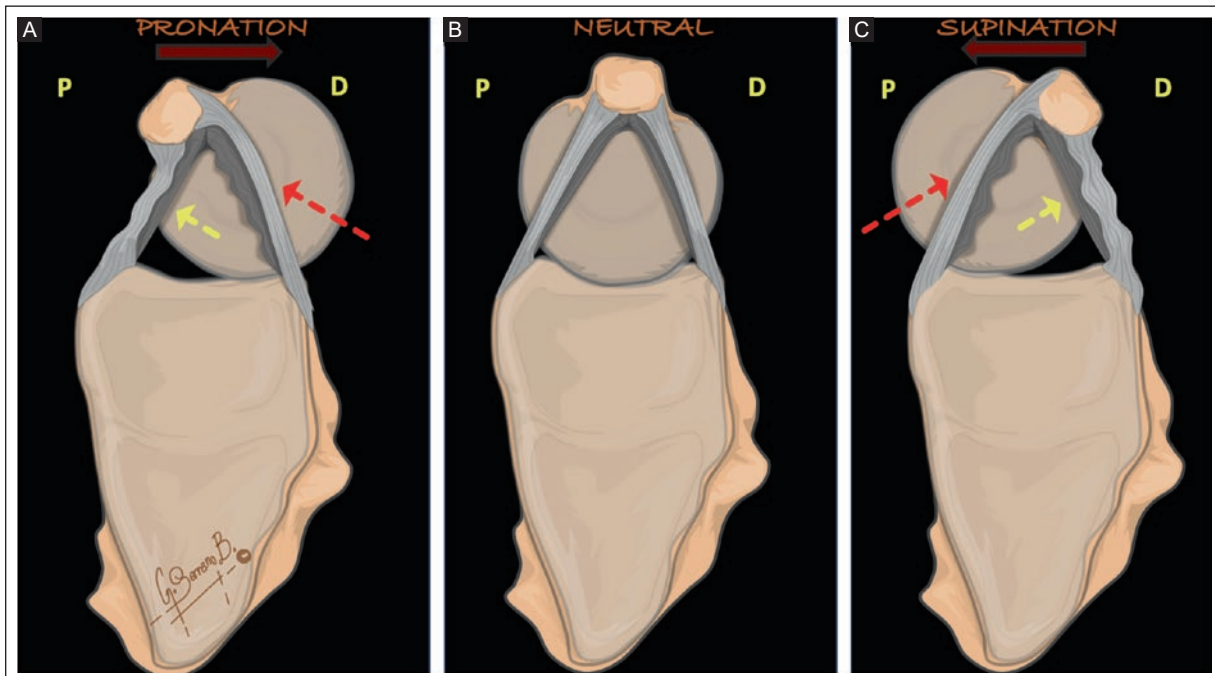


Figure 2. Anatomy and biomechanics of the peripheral ulnar TFCC. **A:** during pronation, the superficial dorsal (red arrow) and deep palmar (yellow arrow) fibers tighten. **B:** neutral position. **C:** in supination, the superficial palmar (red arrow) and deep dorsal (yellow arrow) fibers stretch. The obtuse orientation of the deep foveal fibers becomes mechanically more advantageous to stabilize the joint.

TFCC: triangular fibrocartilage complex.

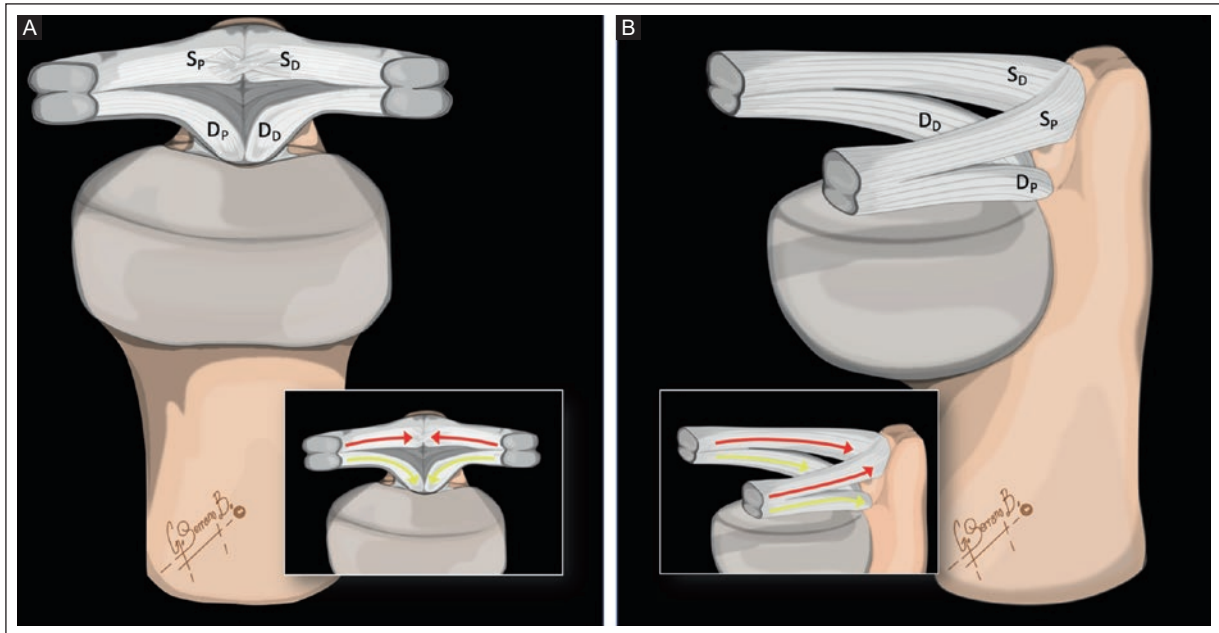


Figure 3. TFCC peripheral insertion. **A and B:** each distal radioulnar ligament is composed of a deep and superficial component; halfway between the radius and ulna, each ligament divides to extend peripherally toward the ulnar styloid and fovea. Therefore, the ulnar peripheral insertion has four arms: a deep palmar arm (D_p), a deep dorsal arm (D_d), a superficial palmar arm (S_p), and a superficial dorsal arm (S_d). TFCC: triangular fibrocartilage complex.

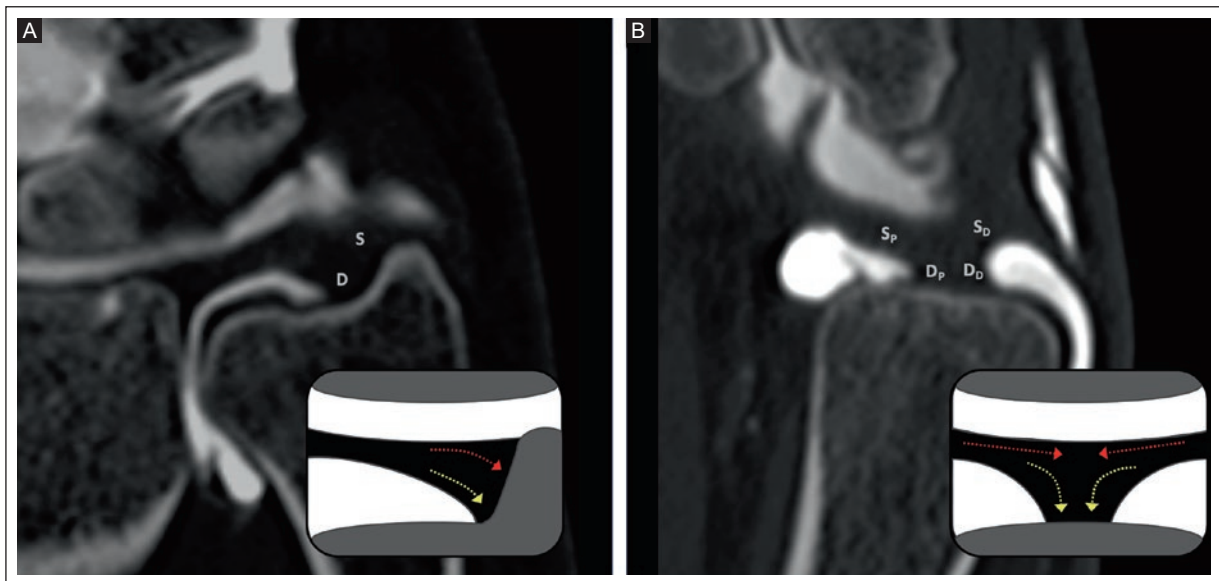


Figure 4. Ulnar insertional anatomy of the TFCC on CT arthrography. **A:** coronal plane. The peripheral ulnar insertion is observed as a single structure with the superficial styloid fibers (S) going toward the base and radial edge of the styloid process of the ulna (red arrow). The deep foveal fibers (D) are directed toward the ulnar fovea, which is a recess devoid of cartilage that lies between the ulnar styloid and the articular cartilage of the distal pole of the ulna. It is a richly vascularized area (yellow arrow). **B:** sagittal plane. Both superficial arms (red arrow) converge toward the ulnar styloid and appear as thickening zones on the periphery of the distal portion of the TFCC (S_p and S_d). The deep arms converge toward the ulnar fovea in an almost vertical orientation (yellow arrow), adopting a “fan morphology” with well-defined edges (D_p and D_d).

CT: computed tomography; D_d : deep dorsal; D_p : deep palmar; S_p : superficial palmar; S_d : superficial dorsal; TFCC: triangular fibrocartilage complex.

Table 1. Different ulnar injury patterns detected on CT arthrography

Tear patterns of the proximal foveal fibers
Tear of the deep palmar or dorsal foveal arm
Tear of both deep foveal arms
Tear patterns of the distal styloid fibers
Tear of the superficial palmar or dorsal styloid arm
Tear of both superficial styloid arms
Tear patterns of the proximal foveal and distal styloid fibers
Tear of the deep and superficial arms on the palmar or dorsal side (complete unilateral)
Tear of both deep foveal arms and one of the superficial styloid arms (palmar or dorsal)
Tear of the four arms of the ulnar insertion of the DRULs

CT: computed tomography; DRULs: dorsal radioulnar ligaments.

although they require different treatments⁷. Combined injuries are also not included, despite being frequently found⁶. Due to these limitations, in 2011, Atzei introduced a specifically targeted classification for ulnar side injuries, suggesting different therapeutic options for each one⁸. Radiologists face the difficult task of providing an adequate description of TFCC peripheral ulnar lesions, to estimate an injury that eventually requires surgical treatment³.

CT arthrography diagnostic role in TFCC injuries

Usually, in TFCC injuries, an imaging test's diagnostic performance is compared with arthroscopy, which has diagnostic and therapeutic capabilities⁹. The categorization of TFCC injuries is essential when deciding to perform surgery. Considering the limited applicability of DRUJ arthroscopy when the foveal fibers are intact, it is crucial to have a less invasive technique capable of providing diagnostic information before surgical exploration³. Palmer 1B injuries are one of the main reasons for requesting a wrist CT arthrography to precisely define the injury characteristics⁴.

CT arthrography has not been widely used despite its high spatial resolution¹⁰. This technique has shown an accuracy greater or at least equal to MR arthrography for the diagnosis of intrinsic ligament and TFCC injuries, with sensitivity, specificity, and precision close to 100%^{11,12}. It is a much faster technique, making it virtually devoid of motion artifacts^{4,9}. It allows high

accuracy to determine injuries, with practically perfect intra and interobserver agreement^{2,3,11,13}. Distension with contrast facilitates the differentiation of the distinct components of the TFCC, especially the foveal fibers, helping avoid performing unnecessary arthroscopies of the DRUJ^{2,14}. The ability to perform multi-planar reconstructions makes it even more valuable^{2,11,13,15}. Most patients tolerate the procedure well, and radiation exposure is not a significant concern with appropriate protocols^{16,17}.

Anatomy and biomechanics of the peripheral ulnar TFCC

The peripheral ulnar insertion of the TFCC is usually referred to as a styloid and foveal insertion through a distal and proximal lamina, respectively¹⁸. However, in a more detailed anatomic view, each DRUL is composed of a deep and superficial component, which divides half-way between the radius and ulna. The superficial arms on each side follow an almost horizontal direction toward the ulnar styloid, while the deep arms take a more vertical orientation toward the fovea^{19,20}. The superficial and deep arms on each side interdigitate at their distal insertion to form a conjoined ligament with two laminae⁴. Each arm can usually be individually followed on images. Some authors even describe an intermediate layer with crosslinked fibers²¹.

Different forces acting on the distal radioulnar joint stretch each of these DRUL components differently. During pronation and supination, the radius rotates around a fixed ulna, as well as some translation. The center of rotation passes through the ulnar fovea. During pronation, the superficial dorsal and deep palmar fibers are tightened, providing stability to the DRUJ. In supination, the superficial palmar and the deep dorsal fibers are stretched²² (Figure 2). The centric insertion of the deep fibers in the fovea and the epicentric insertion of the superficial fibers in the styloid allow a smooth transition between the structures²¹. Foveal fibers have a more advantageous position, playing a more significant role in the stability of the DRUJ compared with styloid fibers²².

Palmar instability of the radius, where the radius shows a palmar displacement relative to the ulna, is a form of DRUJ instability much more frequent than dorsal. In this sense, the deep palmar arm provides higher restriction to the palmar instability of the radius than the deep dorsal arm²³. These facts demonstrate a significant part of the importance of being able to differentiate which specific component of the ulnar TFCC is injured.

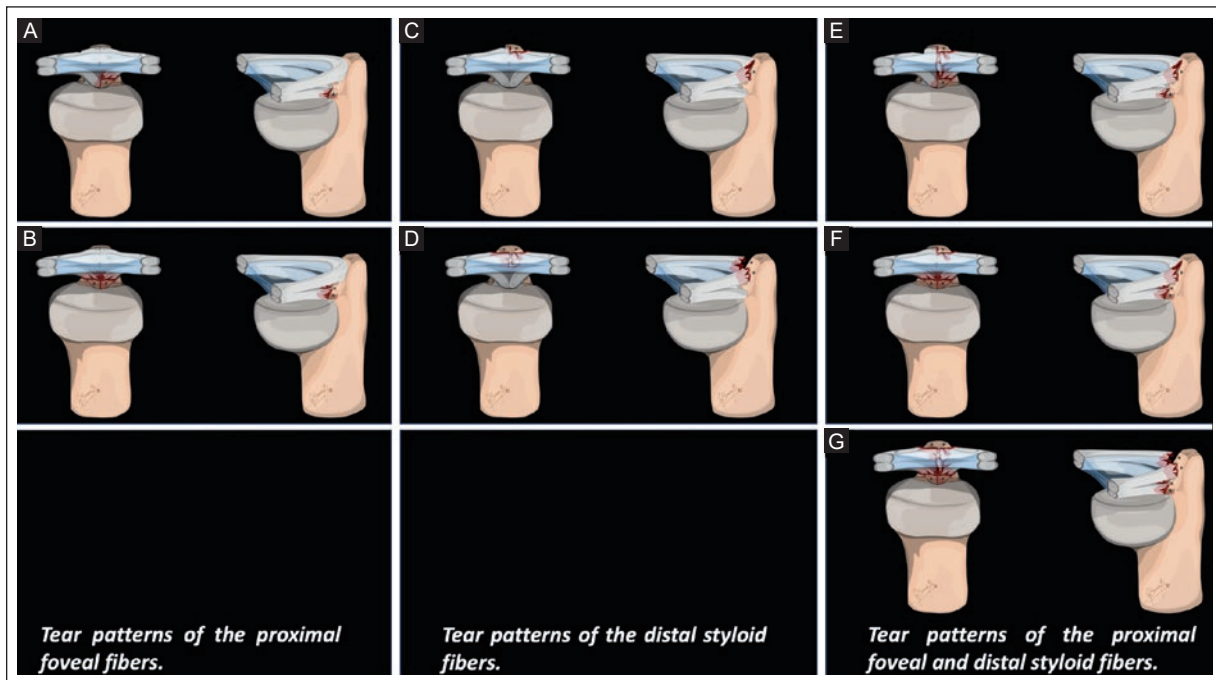


Figure 5. Schematic representation of the different ulnar injury patterns detected on CT arthrography. **A:** tear of the deep palmar or dorsal foveal arm. **B:** tear of both deep foveal arms. **C:** tear of the superficial palmar or dorsal styloid arm. **D:** tear of both superficial styloid arms. **E:** tear of the deep and superficial arms on the palmar or dorsal side (complete unilateral). **F:** tear of both deep foveal arms and one of the superficial styloid arms (palmar or dorsal). **G:** tear of the four arms of the ulnar insertion of the DRULs.

CT: computed tomography; DRULs: distal radioulnar ligaments.

Additionally, the ulnocarpal ligaments have a close relationship with the superficial and deep palmar arms at their distal insertion. The ulnotriquetral ligament attaches to the ulnar styloid along with the superficial palmar arm and the ulnocapitate ligament together with the deep palmar arm²⁴. Biomechanical studies have shown that the ulnocapitate ligament and the deep palmar arm become taut during extension and radial deviation of the wrist^{25,26}. For this reason, it could also be related to the injury mechanism of foveal avulsions. If the different forces acting on these structures are excessive, it may determine an avulsion from the bony insertion. Which components may tear will depend on the predominant mechanism of injury, magnitude, and direction of the traumatic forces acting on the ulnar wrist⁸.

Less attention has been paid to the relationship between the mechanism of injury and the specific anatomical characteristics of the peripheral insertion of the TFCC. Taking this into account, Moritomo et al.²⁷ hypothesized four basic mechanisms for foveal avulsions: (1) forced wrist extension with forearm pronation, tearing first the foveal insertion, and then the superficial dorsal arm; (2) forced extension of the wrist with the

forearm in supination, tearing first the foveal insertion, and then the superficial palmar arm; (3) forced pronation of the forearm, first tearing the superficial dorsal arm, and then the foveal insertion; and (4) forced supination of the forearm, first tearing the superficial palmar arm and then the foveal insertion. For them, this differentiation could change the surgical approach.

Therefore, in the context of the detailed information that can be provided and to better understand the different injury patterns identified in the CT arthrography, it might be convenient to consider the ulnar peripheral insertion as four insertions: a deep palmar arm, a deep dorsal arm, a superficial palmar arm, and a superficial dorsal arm²⁸ (Figure 3). Each of these can be injured individually or in association, as previously noted.

Ulnar peripheral insertion anatomy of the TFCC on CT arthrography

In both the coronal and sagittal planes, the different components of the peripheral ulnar insertion of the TFCC can be adequately evaluated with proper distension of the articular compartments by contrast. In coronal images, both the superficial styloid fibers and the deep

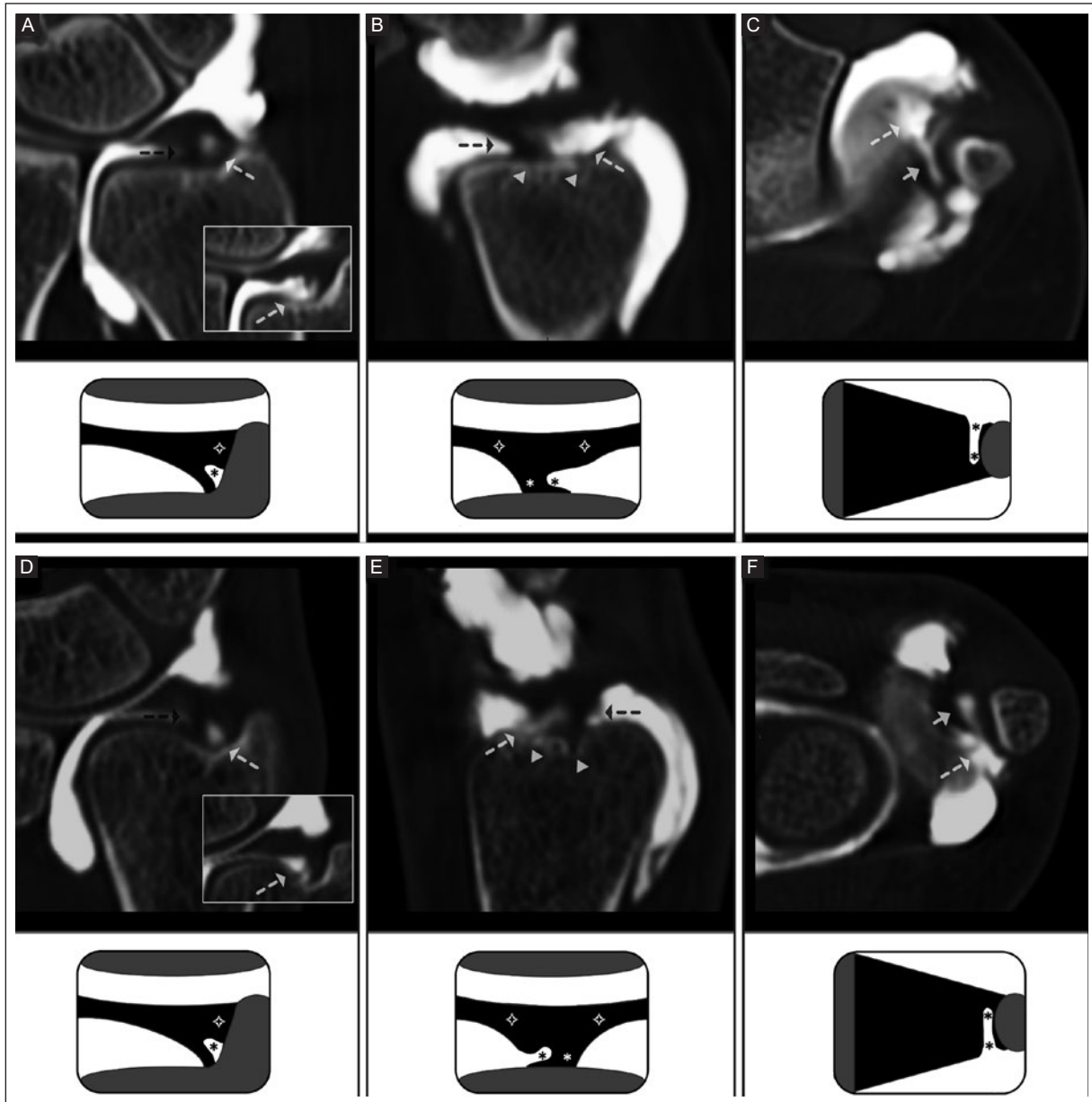


Figure 6. Tear of the deep palmar or dorsal foveal arm. *Upper panel:* **A:** coronal plane. Intraarticular contrast (white arrow) between the fibers at the base of the styloid and the deep foveal fibers (black arrow) is a completely abnormal finding. The coronal section plane is in a more dorsal position with the absence of the dorsal foveal deep fibers (the magnified view is shown). **B:** sagittal plane. Partial loss of the deep fibers “fan morphology” with contrast filtering the dorsal margin (white arrow) with preservation of the palmar margin (black arrow), confirming the tear of the deep dorsal arm. Vascular channels in the fovea (arrowheads). **C:** axial plane. Palmar-dorsal extension of the contrast, at the level of the defect (white long arrow) and extension between the superficial and deep arms in the palmar aspect (white short arrow). *Lower panel:* **D:** coronal, **E:** sagittal, and **F:** axial planes. Defect in this case involving the deep palmar arm (white arrows) is clearly demonstrated in the CT arthrography.

CT: computed tomography.

foveal fibers are seen as a unique hypodense structure. They can be individualized by their anatomical location depending on their insertion site in the radial margin of the ulnar styloid and toward the base of the ulnar styloid and fovea, respectively. On sagittal images, both

superficial arms converge toward the ulnar styloid and appear as thickening areas on the periphery of the distal portion of the TFCC. The distal lamina is the term used to describe the confluence and blending of the superficial palmar and dorsal fibers in their styloid insertion.

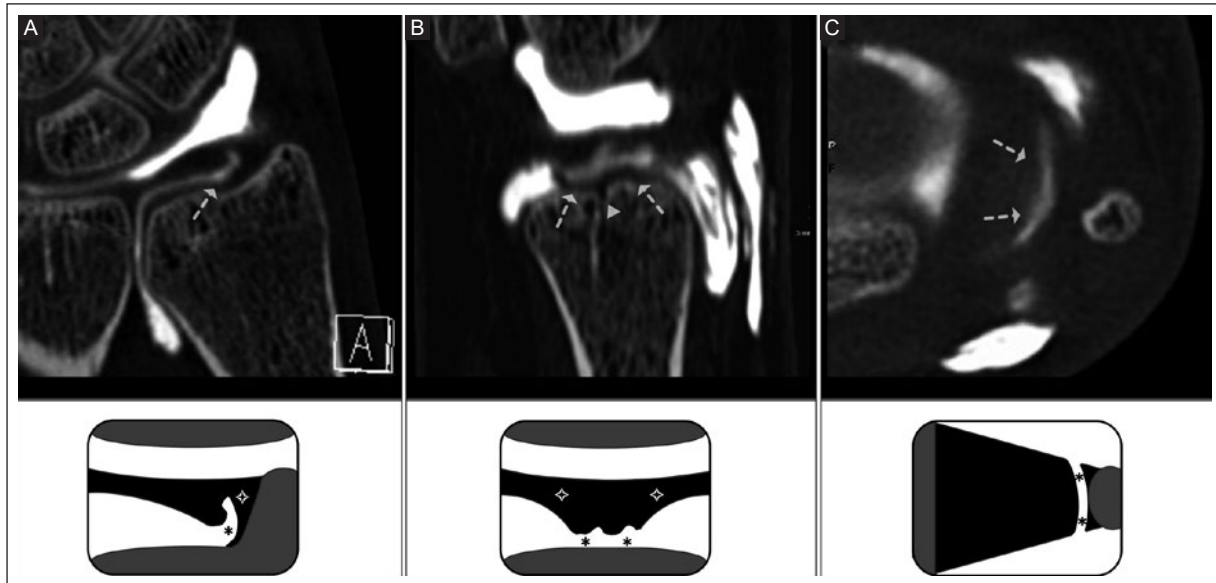


Figure 7. Tear of both deep foveal arms. **A:** coronal plane. Roundish defect involving the deep foveal fibers and those oriented to the base of the ulnar styloid (arrow). **B:** sagittal plane. Disruption of both deep arms with loss of “fan morphology” (white arrows). Vascular channel (arrowhead). **C:** axial plane. Palmar-dorsal extension of the defect (white arrows).

In contrast, the fibers of the deep arms of both radioulnar ligaments converge toward the ulnar fovea, in an almost vertical orientation, forming the proximal lamina. These fibers adopt a “fan morphology” with well-defined edges in the sagittal plane. This fan morphology must always be preserved; otherwise, loss of its expected appearance may represent a tear of the components of the foveal insertion (Figure 4). The axial plane is quite useful to demonstrate the dorsal palmar extension of the ulnar tears, as well as the longitudinal extension of the peripheral non-Palmer injuries frequently associated with these injuries.

Different ulnar injury patterns detected by CT arthrography

Table 1 and Figure 5 show the ulnar injury patterns detected by CT arthrography. The characteristics of these patterns are described below.

Tear patterns of the proximal foveal fibers

– Tear of the deep palmar or dorsal foveal arm

Foveal fibers (proximal lamina) are the main contributor to the stability of the DRUJ. When deciding on appropriate surgical treatment for repairable injuries of the ulnar insertion of the TFCC, the most important parameter is to define the tear of the foveal fibers²⁹.

A frequent mechanism of foveal injuries is hyperextension, usually preserving the dorsal superficial fibers. Tearing of the foveal fibers could represent an early stage of the injury, with later tearing of the remaining components²⁷.

In this tear pattern, it is essential to know the normal configuration of the fibers that run toward the ulnar fovea and not to confuse them with the nearby fibers at the base of the styloid process. In the coronal plane, contrast demarcates the ulnar fovea in the defect area, and a linear or roundish morphology of the defect is identified. The latter has shown high specificity (but low sensibility) for foveal tears in one study, with hand surgeons as exam readers¹³. The typical “fan morphology” is partially lost in the sagittal plane, with contrast filtering one of its margins representing the tear of the deep arm, either palmar or dorsal (Figure 6).

– Tear of both deep foveal arms

The approach is the same as for injuries to one of the deep arms. The sagittal plane (and axial) at the fovea level corroborates the dorsal-palmar extension of the tear, clarifying the tear of both deep arms. Linear or roundish (Figure 7) defects are found¹³. These roundish defects are more prominent. Based on the findings of the imaging exams, they also usually seem to involve the fibers directed toward the base of the styloid, probably assuming a higher degree of clinical

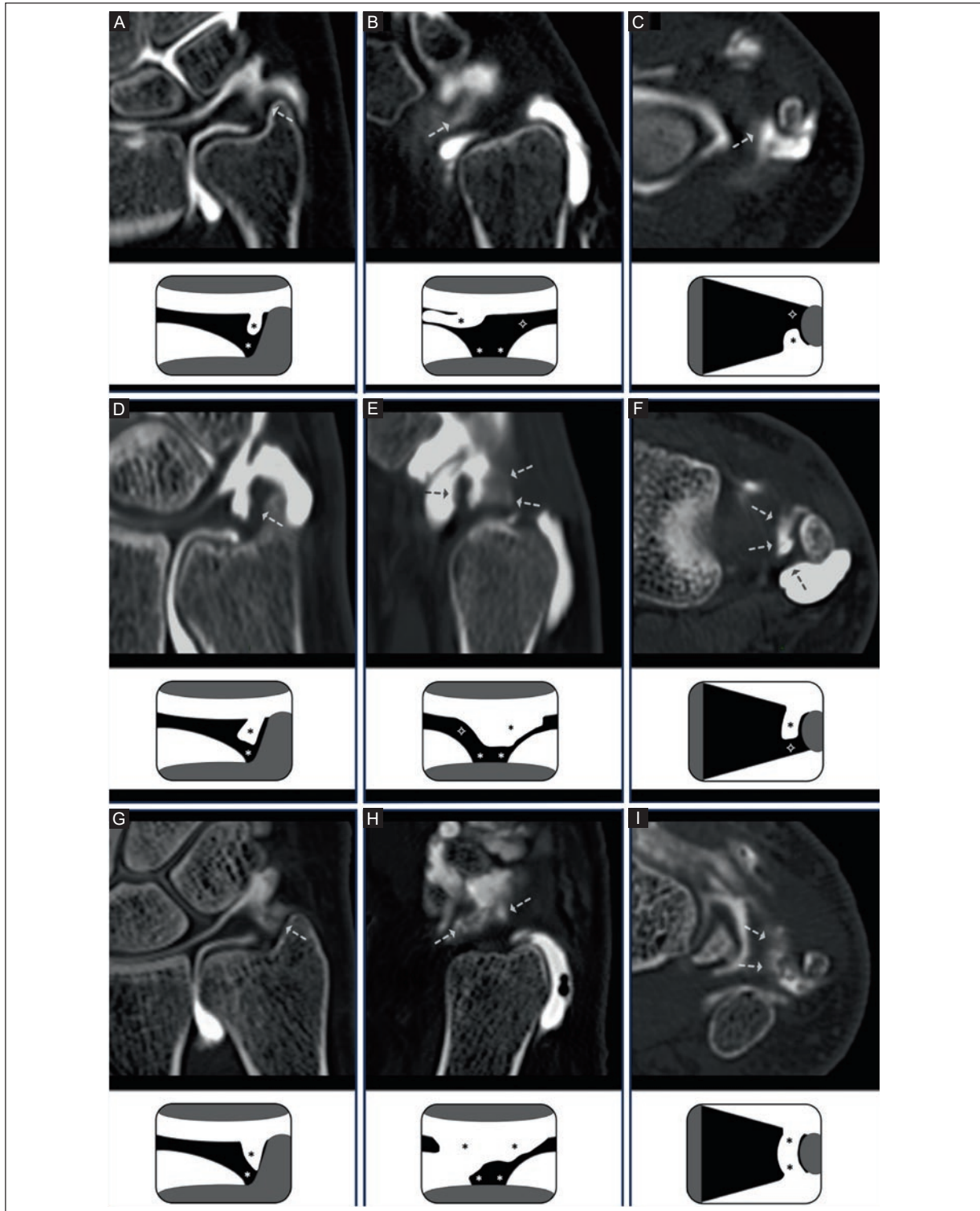


Figure 8. Tear of the superficial palmar or dorsal styloid arm. **Upper panel:** **A:** superficial fibers defect (white arrow), with frondiform grayish tissue partially occupying the tear, representing synovitis. **B:** sagittal plane. Defect is located in the anatomical site of the superficial palmar arm (white arrow). Preservation of “fan morphology.” **C:** axial plane. The defect location is confirmed at the level of the palmar fibers (white arrow). **Middle panel:** **D:** coronal plane. A prominent defect involves the superficial fibers, with contrast filling the tear (white arrow). **E:** sagittal plane. Extensive defect of the superficial fibers (white arrows) with at least partial preservation of the superficial palmar fibers (black arrow). **F:** axial plane. Continuity of the superficial palmar fibers inserting into the ulnar styloid (black arrow). Central and dorsal defect with wide contrast passage (white arrows). **Lower panel:** **G:** superficial fibers defect (white arrow), with frondiform grayish tissue representing synovitis. **H:** sagittal plane. Defect involving both superficial arms, with partial preservation of the dorsal arm (white arrows). Preservation of deep fibers “fan morphology.” **I:** axial plane. Palmar-dorsal extension of the defect (white arrows).

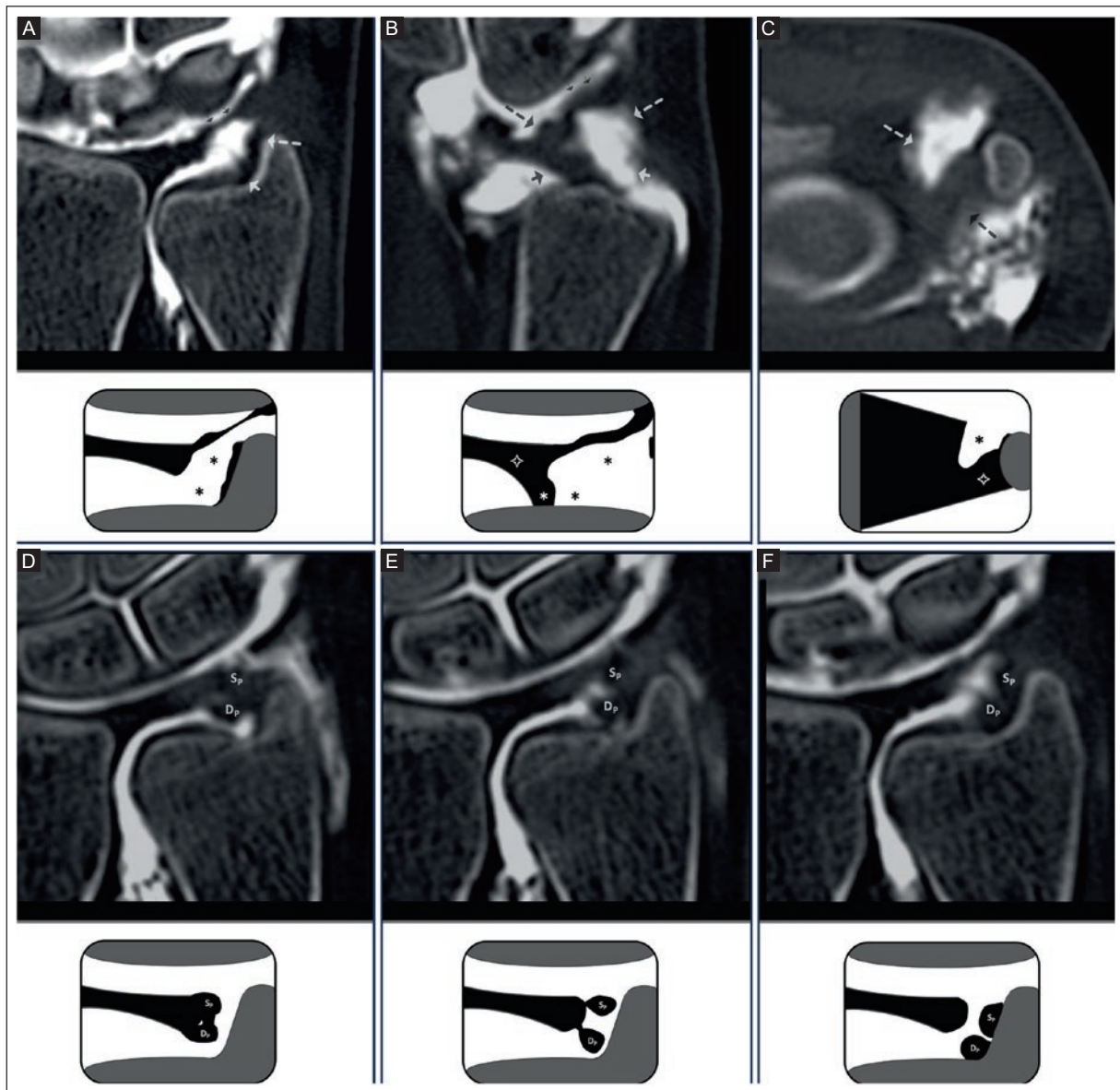


Figure 9. Tear of the deep and superficial arms on the palmar or dorsal side (complete unilateral tear). *Upper panel:* **A:** coronal plane. Complete defect of the superficial (long white arrow) and deep (short white arrow) fibers. Preservation of some thin superficial distal fibers (small black arrows). **B:** sagittal plane. The injury involves the superficial and deep dorsal arms (long and short white arrows) and maintaining the palmar arms (long and short black arrows). Thin superficial distal fibers are preserved, determining a non-communicating injury (small black arrows). **C:** axial plane. Extension of the dorsal defect (white arrow) with uninjured palmar fibers (black arrow). Variant of the Atzei class 2 lesion. *Lower panel:* **D-F:** in the sequential coronal slices from palmar to dorsal, the uninjured superficial palmar (S_p) and deep palmar (D_p) arms can be followed, directed toward their distal insertion in the styloid and fovea, respectively.

D_p: deep palmar; S_p: superficial palmar.

instability. Some remnant fibers may persist at the periphery of the defect. The same findings are made and corroborated in the axial plane.

In the case of a foveal tear (especially the palmar arm) with preservation of the superficial dorsal arm, visualization of the fovea can be difficult from an open dorsal approach, as it is necessary to section the floor of the ECU sheath and the superficial dorsal arm to gain

access to the fovea. This procedure leads to unnecessary iatrogenic sectioning of a distal radioulnar stabilizer to repair the fovea (the deep palmar and superficial dorsal arms stabilize the DRUJ in pronation). In these cases, some authors suggest using a palmar approach to access and repair the palmar foveal fibers³⁰. Therefore, the detailed information provided by the CT arthrography can eventually modify the surgical approach.

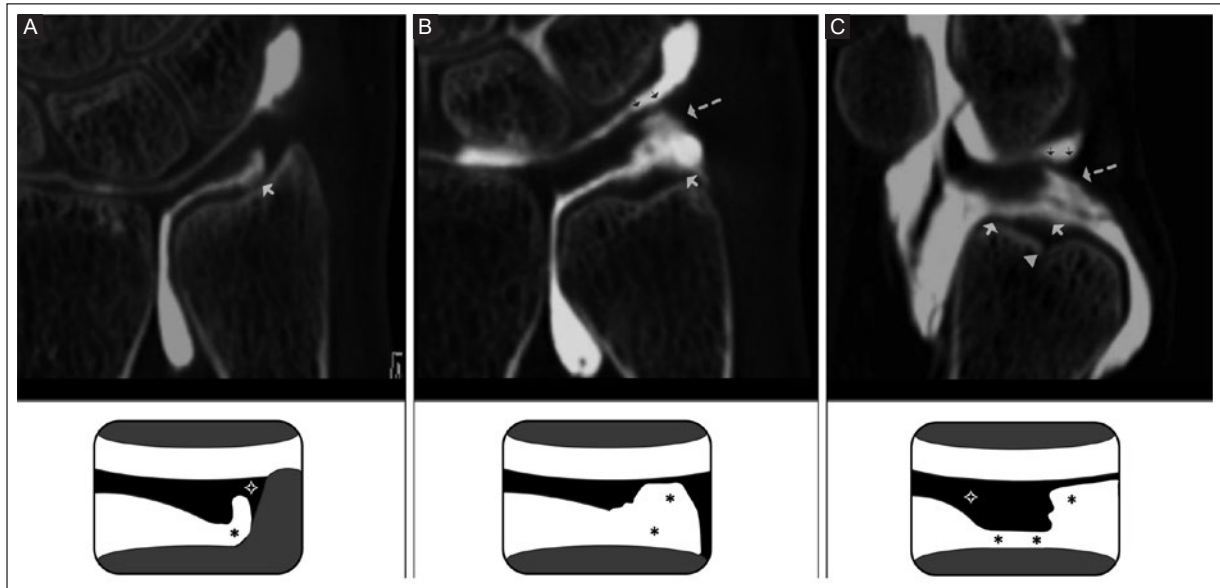


Figure 10. Tear of both deep foveal arms and one of the superficial styloid arms (palmar or dorsal). **A:** palmar coronal plane. Deep fibers defect (short white arrow). **B:** dorsal coronal plane. Complete defect of the superficial (long white arrow) and deep (short white arrow) fibers. Preservation of some thin superficial distal fibers (small black arrows). **C:** sagittal Plane. Defect of both deep arms (short white arrows) with loss of "fan morphology." Tear of the dorsal superficial fibers (long white arrow), with preservation of thin distal fibers, determining a non-communicating injury (small black arrows). Vascular channel (arrowhead). As some distal fibers remain intact, these injuries will not be directly visualized during wrist arthroscopy through the radiocarpal portals.

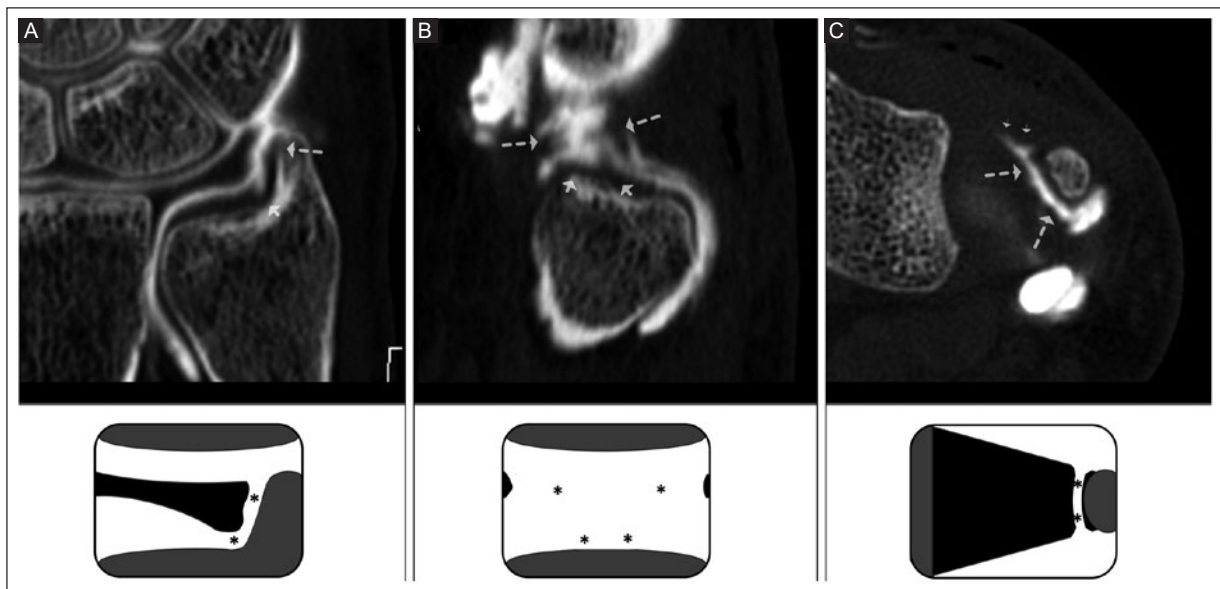


Figure 11. Tear of the four arms of the ulnar insertion of the DRULs. **A:** coronal plane. Complete defect of superficial (long white arrow) and deep (short white arrow) fibers with communication of the compartments, with slight retraction. **B:** sagittal plane. Defect of all four arms (long and short white arrows), with complete loss of peripheral attachment morphology. **C:** axial plane. Complete tear from dorsal to palmar (long white arrows), with an extension to the dorsal ulnar fibrocapsular junction (small white arrows).

DRULs: distal radioulnar ligaments.

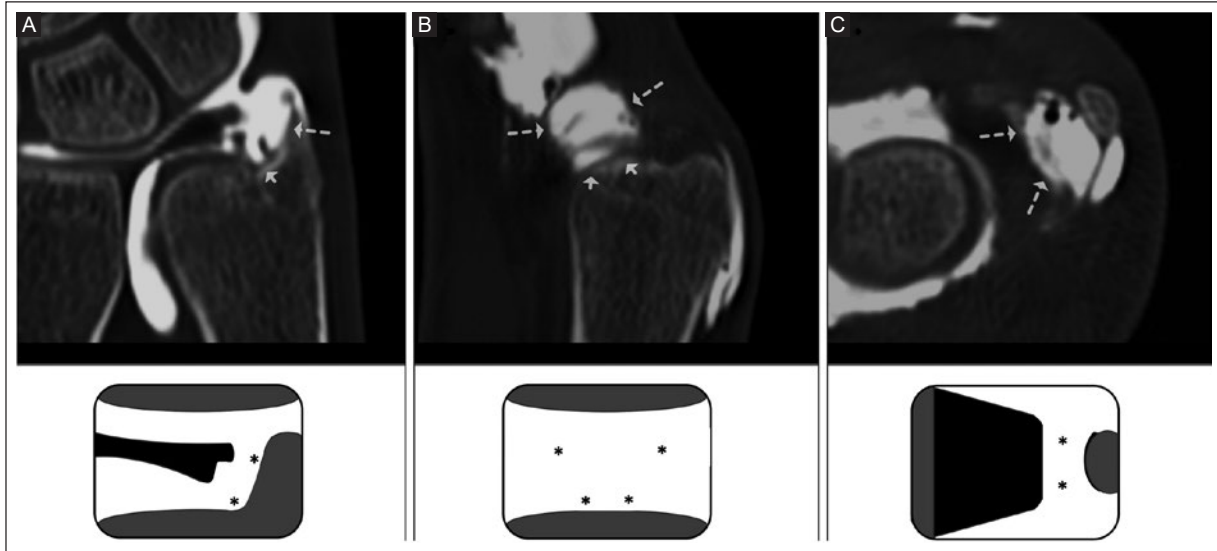


Figure 12. Tear of the four arms of the ulnar insertion of the DRULs with poor margins. **A:** coronal plane. Complete defect of both arms (long and short arrow), with retracted margin. Note the separation of the radioulnar joint, as a sign of joint instability. **B and C:** sagittal and axial planes. Extensive defect of the ulnar peripheral insertion can be clearly quantified.

DRULs: distal radioulnar ligaments.

Tear patterns of the distal styloid fibers

– Tear of the superficial palmar or dorsal styloid arm

The superficial arms (distal lamina) are inserted at the ulnar styloid's radial edge and can occupy its entire extension from the base to the tip³¹. The tear is frequently covered by synovitis in arthroscopies, requiring synovectomy for visualization^{6,7}. Although it does not necessarily cause significant instability when torn in isolation, it can cause ulnar wrist pain highly symptomatic⁶. In the multiplanar examination, the interruption of one of the superficial arms' fibers is observed with the same clarity as in tears of the foveal fibers. It is necessary to take into consideration that they may not fill homogeneously with contrast, partially occupied by a grayish frondiform tissue representing synovitis (Figure 8). The tear can be quite prominent and give the impression of compromising both arms. However, in the multiplanar approach, at least partial indemnity of one of the arms can be precisely identified.

– Tear of both superficial styloid arms

The defect of both superficial arms is confirmed by carefully examining all the imaging planes. It is only necessary to be careful with the abundant synovitis that frequently occupies them, making their identification sometimes tricky (Figure 8). Synovitis and the tear may extend to the pre-styloid recess⁷.

Tear patterns of the proximal foveal and distal styloid fibers

– Tear of the deep and superficial arms on the palmar or dorsal side (complete unilateral)

In this variety of injury patterns, a superficial analysis of the images in the coronal plane can be interpreted as a complete tear of the ulnar peripheral insertion of the TFCC; in the Atzei classification⁸, it might seem like a pure class 2 lesion. However, in a detailed multiplanar evaluation, preservation of the superficial and deep fibers of one of the sides will be confirmed, whether palmar or dorsal depending on the predominant mechanism of injury (Figure 9). This exceptionally detailed assessment of the components that are torn and preserved may perhaps explain in part why in class 2 injuries in the Atzei classification, the degree of instability of the distal radioulnar joint ranges from mild to severe. Probably, as we can demonstrate in the CT arthrography, there may be at least partial preservation of the fibers on one side, actually representing a variant of the Atzei class 2 lesion.

– Tear of both deep foveal arms and one of the superficial styloid arms (palmar or dorsal)

The excellent spatial resolution of the CT arthrography allows for quantifying the extent of a lesion quite accurately and corroborates the specific components of the peripheral insertion that are compromised and

preserved. Together with any of the superficial arms, either palmar or dorsal, injury to the foveal fibers can occur quite frequently in the context of peripheral ulnar tears. As proposed by Moritomo et al.²⁷, the combination of these could represent a mechanism of injury with an extension of the wrist, either in supination (injury to the foveal fibers first and then the superficial palmar arm) or in pronation (injury to the foveal fibers first and later the superficial dorsal arm). It is not uncommon that the injury to the superficial arms, which may be a high-grade tear, leaves some undamaged fibers on the ligament's distal surface that faces the radiocarpal compartment (Figure 10). This injury represents a non-communicating tear; therefore, there are some essential facts to emphasize. The first is the importance of always injecting contrast into the distal radioulnar compartment⁴. Otherwise, these lesions will go unnoticed. As some distal fibers remain intact, these injuries will not be visualized directly during wrist arthroscopy through the radiocarpal portals. In other words, according to Atzei's concept of the Iceberg⁸, we could be facing a significant tear from the biomechanical point of view, completely submerged underwater for the orthopedic surgeon's eyes. With an adequate description of the injury, this valuable information can become essential during surgical planning.

– **Tear of the four arms of the ulnar insertion of the DRUL's**

These injuries are usually, but not always, communicating injuries, with contrast passing between the radiocarpal and the distal radioulnar compartment¹³. They combine the findings of the previously mentioned patterns, with loss of continuity of the deep and superficial fibers in the coronal plane in the ulnar insertion. In the sagittal plane at the tear level, a complete distortion of the expected morphology will be seen in the peripheral ulnar portion of the TFCC, with the defect involving the four arms of the DRULs (Figure 11). These injuries are the ones that most commonly require surgical repair, given the degree of instability they produce^{7,32}. As with repairs elsewhere, they must be stress-free. Therefore, the description of the defect is essential, as substantial defects with poor-quality retracted segments will be more likely to be reconstructed than repaired with reinsertion⁷ (Figure 12).

CONCLUSION

CT arthrography is a highly capable imaging technique to evaluate TFCC injuries. When evaluating ulnar peripheral tears, the multiplanar approach allows a

detailed description of the different components affected. This approach to assessing ulnar TFCC injuries in imaging studies has not been described in the literature to the best of the author's knowledge. This information could be quite valuable to carry out a more reliable clinical-radiological correlation and become the starting point for future research studies. Furthermore, it may have implications at the time of surgical planning, even changing the surgical approach. Radiologists face the difficult task of providing an adequate description of the ulnar peripheral TFCC tears, and the approach presented in this article can significantly facilitate this task.

Funding

The authors declare that they did not receive any funding or support for this article.

Conflicts of interest

The authors declare no conflicts of interest.

Ethical disclosures

Protection of individuals. The author declares that no experiments were performed on humans or animals.

Confidentiality of data. The author declares that no patient data are included in this article.

Right to privacy and informed consent. The author declares that no patient data appear in this article.


Use of artificial intelligence. The author states that he did not use generative artificial intelligence to prepare this manuscript and/or create table, figures, or figure legends.

REFERENCES

1. Semisch M, Hagert E, Garcia-Elias M, Lluch A, Rein S. Histological Assessment of the Triangular Fibrocartilage Complex. *J Hand Surg Eur.* 2016;41(5):527-533. doi:10.1177/1753193415618391.
2. Kim S, Lee GY, Lee JS. Evaluation of the triangular fibrocartilage: comparison of two-compartment wrist CT arthrography using the distal radioulnar and radiocarpal joints and unicompartement wrist CT arthrography using the radiocarpal joint. *Br J Radiol.* 2019;92(1102):20190298. doi: 10.1259/bjr.20190298.
3. Grunz JP, Gietzen CH, Luetkens K, Wagner M, Kalb K, Bley TA, et al. The importance of radial multiplanar reconstructions for assessment of triangular fibrocartilage complex injury in CT arthrography of the wrist. *BMC Musculoskelet Disord.* 2020;21(1):286. doi:10.1186/s12891-020-03321-2.
4. Cerezal L, de Dios Berná-Mestre J, Canga A, Llopis E, Rolon A, Martín-Oliva X, et al. MR and CT arthrography of the wrist. *Semin Musculoskelet Radiol.* 2012;16(1):27-41. doi:10.1055/s-0032-1304299.
5. Haims AH, Schweitzer ME, Morrison WB, Deely D, Lange R, Osterman AL, et al. Limitations of MR imaging in the diagnosis of peripheral tears of the triangular fibrocartilage of the wrist. *AJR Am J Roentgenol.* 2002;178(2):419-422. doi: 10.2214/ajr.178.2.1780419.
6. Abe Y, Tominaga Y, Yoshida K. Various patterns of traumatic triangular fibrocartilage complex tear. *Hand Surg.* 2012;17(2):191-198. doi: 10.1142/S0218810412500189.

7. Atzei A, Luchetti R, Garagnani L. Classification of ulnar triangular fibrocartilage complex tears. A treatment algorithm for Palmer type IB tears. *J Hand Surg Eur.* 2017;42(4):405-414. doi: 10.1177/1753193416687479.
8. Atzei A, Luchetti R. Foveal TFCC tear classification and treatment. *Hand Clin.* 2011;27(3):263-272. doi: 10.1016/j.hcl.2011.05.014.
9. Moser T, Khoury V, Harris PG, Bureau NJ, Cardinal E, Dosch JC. MDCT arthrography or MR arthrography for imaging the wrist joint? *Semin Musculoskelet Radiol.* 2009;13(1):39-54. doi: 10.1055/s-0029-1202244.
10. Schmid MR, Schertler T, Pfirrmann CW, Saupe N, Manestar M, Wildermuth S, et al. Interosseous ligament tears of the wrist: comparison of multi-detector row CT arthrography and MR imaging. *Radiology.* 2005; 237(3):1008-1013. doi: 10.1148/radiol.2373041450.
11. Moser T, Dosch JC, Moussaoui A, Dietemann JL. Wrist ligament tears: evaluation of MRI and combined MDCT and MR arthrography. *AJR Am J Roentgenol.* 2007;188(5):1278-1286. doi: 10.2214/AJR.06.0288.
12. Theumann N, Favarger N, Schnyder P, Meuli R. Wrist ligament injuries: value of post-arthrography computed tomography. *Skeletal Radiol.* 2001;30(2):88-93. doi: 10.1007/s002560000302.
13. Moritomo H, Arimitsu S, Kubo N, Masatomi T, Yukioka M. Computed tomography arthrography using a radial plane view for the detection of triangular fibrocartilage complex foveal tears. *J Hand Surg Am.* 2015; 40(2):245-251. doi: 10.1016/j.jhsa.2014.10.051.
14. Bille B, Harley B, Cohen H. A comparison of CT arthrography of the wrist to findings during wrist arthroscopy. *J Hand Surg Am.* 2007;32(6): 834-841. doi: 10.1016/j.jhsa.2007.04.005.
15. Lee RKL, Griffith JF, Ng AW, Law EK, Tse WL, Wong CW, et al. Intrinsic carpal ligaments on MR and multidetector CT arthrography: comparison of axial and axial oblique planes. *Eur Radiol.* 2017;27(3):1277-1285. doi: 10.1007/s00330-016-44-x.
16. Binkert CA, Zanetti M, Hodler J. Patient's assessment of discomfort during MR arthrography of the shoulder. *Radiology.* 2001;221(3):775-778. doi:10.1148/radiol.2213010277.
17. Moser T, Sauer B, Clavert P, Kahn JL, Gang A, Roy C. High Resolution 64-MDCT of the Wrist: Should We Use the Peripheral Detector ROWK? Presented at: Annual Meeting of RSNA; November 26, 2007; Chicago. IL.
18. Palmer AK, Werner FW. The triangular fibrocartilage complex of the wrist-anatomy and function. *J Hand Surg Am.* 1981;6(2):153-162. doi: 10.1016/s0363-5023(81)80170-0.
19. Ishii S, Palmer AK, Werner FW, Short WH, Fortino MD. An anatomic study of the ligamentous structure of the triangular fibrocartilage complex. *J Hand Surg Am.* 1998;23(6):977-985. doi: 10.1016/S0363-5023(98)80003-8.
20. Nakamura T, Makita A. The proximal ligamentous component of the triangular fibrocartilage complex. *J Hand Surg Br.* 2000;25(5):479-486. doi: 10.1054/jhsb.1999.0329.
21. Haugstvedt JR, Langer MF, Berger RA. Distal radioulnar joint: functional anatomy, including pathomechanics. *J Hand Surg Eur.* 2017;42(4):338-345. doi:10.1177/1753193417693170.
22. Kleinman WB. Stability of the distal radioulnar joint: biomechanics, pathophysiology, physical diagnosis, and restoration of function what we have learned in 25 years. *J Hand Surg Am.* 2007;32(7):1086-1106. doi: 10.1016/j.jhsa.2007.06.014.
23. Moritomo H, Kataoka T. Palmar reconstruction of the triangular fibrocartilage complex for static instability of the distal radioulnar joint. *Tech Hand Up Extrem Surg.* 2014;18(3):110-115. doi: 10.1097/BTH.0000000000000047.
24. Berger RA. The ligaments of the wrist. A current overview of anatomy with considerations of their potential functions. *Hand Clin.* 1997;13(1):63-82.
25. Moritomo H, Murase T, Arimitsu S, Oka K, Yoshikawa H, Sugamoto K. Change in the length of the ulnocarpal ligaments during radiocarpal motion: possible impact on triangular fibrocartilage complex foveal tears. *J Hand Surg Am.* 2008;33(8):1278-1286. doi:10.1016/j.jhsa.2008.04.033.
26. Sennwald GR, Lauterburg M, Zdravkovic V. A new technique of reattachment after traumatic avulsion of the TFCC at its ulnar insertion. *J Hand Surg Br.* 1995;20(2):178-184. doi: 10.1016/s0266-7681(05)80046-4.
27. Moritomo H, Masatomi T, Murase T, Miyake J, Okada K, Yoshikawa H. Open repair of foveal avulsion of the triangular fibrocartilage complex and comparison by types of injury mechanism. *J Hand Surg Am.* 2010;35(12): 1955-1963. doi: 10.1016/j.jhsa.2010.07.031.
28. Chou KH, Sarris IK, Sotereanos DG. Suture anchor repair of ulnar-sided triangular fibrocartilage complex tears. *J Hand Surg Br.* 2003;28(6):546-550. doi: 10.1016/s0266-7681(03)00173-6.
29. Atzei A, Luchetti R, Braidotti F. Arthroscopic foveal repair of the triangular fibrocartilage complex. *J Wrist Surg.* 2015;4(1):22-30. doi: 10.1055/s-0035-1544226.
30. Moritomo H. Advantages of open repair of a foveal tear of the triangular fibrocartilage complex via a palmar surgical approach. *Tech Hand Up Extrem Surg.* 2009;13(4):176-181. doi: 10.1097/BTH.0b013e3181bd8319.
31. Prendergast N, Rauschnig W. Normal anatomy of the hand and wrist. *Magn Reson Imaging Clin N Am.* 1995;3(2):197-212.
32. Atzei A, Luchetti R. In book: *Principles and Practice of Wrist Surgery*, Chapter: Repair of the foveal insertion of the TFCC through the DF portal, Editors: David J. Slutsky MD FRCS, November 2009 pp.559-568.

Validation of the Ultrasound Neck Node Reporting and Data System (UNN-RADS) for predicting lymph node metastases in thyroid cancer

Oquitzin Flores-Palomares¹ , Hilda E. Macias-Cervantes², Oswaldo Maya-Martinez¹,
Martha A. Hernandez-Gonzalez³, and Luz F. Velazquez-Fernandez¹

¹Diagnostic and Therapeutic Imaging Department; ²Internal Medicine Department; ³Research Department. Hospital de Alta Especialidad No. 1 Bajío, Centro Médico Nacional, Instituto Mexicano del Seguro Social, León, Guanajuato, Mexico

ABSTRACT

Introduction: An ultrasound (US) scoring system was developed by combining seven ultrasonographic descriptors for predicting metastatic lymph nodes (LNs). The aims of this study were (1) to validate the Ultrasound Neck Node Reporting and Data System (UNN-RADS) for suspicious ultrasonographic features of LN metastasis in patients undergoing thyroid cancer follow-up and (2) to evaluate the interobserver agreement. **Materials and Methods:** Patients undergoing thyroid cancer follow-up were evaluated with US and US-guided fine-needle aspiration biopsy (FNAB) of the LNs. The weighted UNN-RADS score of seven ultrasonographic descriptors, namely, shape, margin, echogenicity, echogenic hilum, cystic degeneration, calcification, and intranodal vascular pattern for suspicious malignant LN was evaluated. UNN-RADS categories were assigned according to the total score. The optimal cut-off value and diagnostic performance of the weighted score for predicting malignant LN were determined using a receiver operating characteristic (ROC) curve. Cohen's kappa was used to calculate the interobserver agreement. **Results:** We included 99 LNs from 99 patients who underwent thyroid cancer follow-up, of which 46 (46.5%) had metastatic LNs and 53 (53.5%) LNs were benign. Metastatic LNs were UNN-RADS categories 3 (22/46), 4 (15/46), and 5 (9/46), while LNs in UNN-RADS categories 1 and 2 were benign. A cut-off of 6 points, corresponding to UNN-RADS category 3, had a sensitivity of 100% for predicting malignant LNs. The ROC curve showed an AUC of 0.893 (95% CI, 81.5–94.6). The interobserver agreement between the two radiologists was good ($\kappa = 0.71$, 95% CI 0.573–0.798). **Conclusion:** UNN-RADS is a reliable tool for predicting LN metastases in thyroid cancer patients during follow-up. The multiple features in this scoring system, which weighs US findings suspicious of malignancy, may be more accurate than a single feature.

Keywords: Thyroid. Thyroid cancer. Lymph node. Ultrasound. Lymph node metastasis.

INTRODUCTION

The incidence of thyroid cancer has steadily increased worldwide. Despite a good prognosis, neck lymph node (LN) metastases occur in 20–80% of cases^{1–3}. LN levels VI and VII are more commonly affected and associated with papillary thyroid carcinoma (PTC), medullary thyroid carcinoma (MTC), and anaplastic thyroid carcinoma

(ATC)⁴. Correct differentiation of benign and malignant LN involvement is critical in thyroid cancer follow-up^{5–7}. Ultrasound (US) is the primary imaging modality for evaluating and diagnosing cervical LNs due to its accessibility, speed, safety, low cost, and the fact that it does not require exposure to ionizing radiation^{8–11}. The accuracy of US examination in detecting suspicious LN malignancy has been widely assessed with varying results^{1,4}.

*Corresponding author:

Oquitzin Flores-Palomares
E-mail: oquitzinflores@gmail.com

Received for publication: 23-12-2023

Accepted for publication: 14-02-2024

DOI: 10.24875/JMEXFRI.23000025

Available online: 22-03-2024

J Mex Fed Radiol Imaging. 2024;3(1):17-26

www.JMEXFRI.com

2696-8444 / © 2024 Federación Mexicana de Radiología e Imagen, A.C. Published by Permanyer. This is an open access article under the CC BY-NC-ND (<https://creativecommons.org/licenses/by-nc-nd/4.0/>).

It is important to note that while some US features are promising in identifying LN metastases, a single US feature cannot predict a malignant LN^{1,4,5,12-17}.

A scoring system that weighs various US findings of suspected malignancy may be more accurate in predicting malignant lymphadenopathy than a single feature¹⁸. In 2022, Sarda-Inman et al.¹⁸ developed the Ultrasound Neck Node Reporting and Data System (UNN-RADS), based on a weighted scoring system combining seven ultrasonographic descriptors (shape, margin, echogenicity, echogenicity of the hilum, vascularity and the presence or absence of calcifications, and cystic degeneration) that are suspicious for malignancy and increase the predictability of metastatic LN, with scores ranging from 0 to 3 points, which allows separation into five different risk categories. The clinical application of the UNN-RADS requires validation in an independent cohort with different populations and US operators. The aims of this study were (1) to validate the UNN-RADS for predicting malignant LNs with cytopathologic confirmation in patients undergoing thyroid cancer follow-up and (2) to evaluate the interobserver agreement.

MATERIALS AND METHODS

An ambispective study was conducted between January 2022 and October 2023 in the Department of Diagnostic and Therapeutic Imaging at the Hospital of Alta Especialidad 1 CMN Bajío in Leon, Guanajuato, Mexico. Informed consent was obtained from prospectively enrolled participants and waived for retrospectively enrolled patients. The methods and data reporting were in accordance with the guidelines of the Standards for Reporting of Diagnostic Accuracy Studies (STARD)¹⁹. Our Institutional Review Board approved the study.

Patient selection

Consecutive patients of both sexes over the age of 18 years undergoing follow-up for thyroid cancer and with a US-guided fine-needle aspiration biopsy (FNAB) of the LN and at least one of the seven ultrasonographic features of suspicious metastases defined in the UNN-RADS¹⁸ were included. Patients were excluded if they had a previous bilateral cervical LN dissection as thyroid cancer treatment or an FNAB with an indeterminate result. LNs were confirmed metastatic or benign by Bethesda system cytopathologic examination at the local laboratory. Sex and age were also recorded.

US protocol and US-guided FNAB

US thyroid examinations were performed with an HS50 unit (Samsung, Seoul, Korea) or a MyLab™ Eight eXP unit (Esaote, Barcelona, Spain) with a 5–14-MHz linear probe. All US examinations and US-guided FNABs were performed by residents under the supervision of staff radiologists with at least 10 years of clinical experience in evaluating thyroid US images. The thyroid US examination was orderly and systematically performed with a review of the seven LN levels¹⁸. When multiple adjacent suspicious LNs were found, an easily accessible LN was chosen for FNAB.

Imaging analysis

LNs were assessed during US-guided FNAB, and in some cases, retrospectively, using images stored in the Picture Archiving and Communication System (PACS). LNs were assessed by two radiologists with 10 and 11 years of experience in oncologic imaging and interventional radiology, respectively. In the retrospective assessment of the LNs, the evaluators were blinded to the cytopathology FNAB results.

LNs were scored using seven US features suspicious for malignancy, as defined by Sarda et al.¹⁸:

Shape (oval, round, or lobulated): round was determined by the ratio of shortest-to-longest axis in the longitudinal plane of the LN, and lobulated was defined as three or more undulations.

Margin (circumscribed or noncircumscribed): determined by the sharpness of the LN edge.

Echogenicity (hypoechoogenicity or hyperechogenicity): determined by comparison with adjacent muscles.

Echogenic hilum (present $\geq 25.0\%$, present $< 25.0\%$ or absent): the percentage was determined by the maximum diameter of the short axis of the LN in relation to the hilum thickness.

Presence of cystic degeneration: irregular prominent anechoic areas.

Calcification (present or absent): punctate hyperechoic foci with or without a posterior acoustic shadow.

Intranodal vascular pattern (hilar or nonhilar): determined by the distribution of vascular flow signals within the LN. A nonhilar intranodal vascular pattern may have peripheral vascularity, defined as flow signals along the periphery or in the capsular portion.

All US-guided FNABs were performed under the physician's direction and when the LNs had at least one of the seven suspicious features of malignancy. LNs were scored for each ultrasonographic feature with a 1-, 2-, or

Table 1. UNN-RADS structured reporting format modified from Sarda-Inman et al.¹⁸

US feature	Descriptor	Points	Patient score	
Shape	Oval	0		
	Round or lobulated	2		
Margin	Circumscribed	0		
	Non-circumscribed	1		
Echogenicity	Hypoechoogenicity	0		
	Hyperechoogenicity	2		
Echogenic hilum	≥ 25.0%	0		
	< 25.0% or Absent	3		
Cystic degeneration	Absent	0		
	Present	3		
Calcification	Absent	0		
	Present	1		
Intranodal vascular pattern	Hilar	0		
	Nonhilar	2		
Total				
UNN-RADS category				
UNN-RADS 1 0-3 points Benign, No FNAB	UNN-RADS 2 4-5 points Probably benign, No FNAB	UNN-RADS 3 6-8 points Mildly suspicious for malignancy, FNAB ^a or follow-up	UNN-RADS 4 9-11 points Moderately suspicious for malignancy, FNAB ^a	UNN-RADS 5 ≥12 points Highly suspicious for malignancy, FNAB ^a

UNN-RADS: Ultrasound Neck Node Reporting and Data System; US: ultrasound; FNAB: fine-needle aspiration biopsy.

^aIf the referring physician's suspicion or the US features suggest lymphoma, a core biopsy should be performed.

3-point scale (Table 1). The sum of the scores determined the UNN-RADS category according to the total score of ultrasonographic descriptors suspicious for LN malignancy: category 1 – benign with a score of 3 or less; category 2 – probably benign with 4-5 points; category 3 – mildly suspicious for malignancy with 6-8 points; category 4 – moderately suspicious for malignancy with 9-11 points; and category 5 – highly suspicious for malignancy with 12 or more points.

Statistical analysis

The sample size was calculated considering the overall sensitivity of US for detecting malignant cervical LNs, which was 96.8%, a specificity of 80%¹⁸, and a prevalence of 10% for thyroid cancer, with a 95% confidence interval and a loss of 20.0%. The calculated sample size was 12 patients. The Kolmogorov–Smirnov test was used to determine the normality of the data. Continuous

variables were expressed as mean ± standard deviation (SD), and Student's t-test was used for comparison. The association between benign and metastatic LN US features was assessed using the chi-square or Fisher's exact tests for categorical variables. LNs were dichotomized into two groups to assess the diagnostic performance of UNN-RADS: UNN-RADS categories 1 or 2 were defined as negative, and UNN-RADS categories 3–5 were positive. A receiver operating characteristic (ROC) curve determined the optimal cut-off value of the weighted score of the US features for the prediction of malignant LNs. Diagnostic performance was evaluated by sensitivity, specificity, positive predictive value (PPV), negative predictive value (NPV), positive likelihood ratio (+LR), and accuracy. Cohen's kappa was used to calculate the agreement between the two radiologists. All tests were two-sided, and a *p*-value < 0.05 was considered significant. All statistical analyses were performed using the R Statistical software (version 4.3.1; R

Table 2. Comparison of seven ultrasonographic descriptors for malignant and benign LNs with cytopathologic confirmation from thyroid cancer patient follow-up

Characteristic	Total n = 99	Metastatic LNs n = 46 (46.5%)	Benign LNs n = 53 (53.5%)	p-Value
Age, years, mean \pm SD	48.0 \pm 14.6	47.3 \pm 15.8	49.0 \pm 13.6	0.564
Female, n (%)	70 (70.7)	32 (70.0)	38 (72.0)	0.991
Male, n (%)	29 (29.3)	14 (30.0)	15 (28.0)	
Shape				< 0.001
Oval, n (%)	37 (37.4)	4 (8.7)	33 (62.2)	
Round or lobulated, n (%)	62 (62.6)	42 (91.3)	20 (37.8)	
Margin				0.01
Circumscribed, n (%)	92 (92.9)	39 (84.8)	53 (100)	
Non-circumscribed, n (%)	7 (7.1)	7 (15.2)	0	
Echogenicity				< 0.001
Hypoechoogenicity, n (%)	32 (32.3)	25 (54.3)	7 (13.2)	
Hyperechogenicity, n (%)	67 (67.7)	21 (45.7)	46 (86.8)	
Echogenic hilum				0.005
\geq 25.0%, n (%)	10 (10.1)	0	10 (18.9)	
< 25.0% or absent, n (%)	89 (89.9)	46 (100)	43 (81.1)	
Cystic degeneration				< 0.001
Absent, n (%)	74 (74.8)	27 (58.7)	47 (88.7)	
Present, n (%)	25 (25.2)	19 (41.3)	6 (11.3)	
Calcification				0.002
Absent, n (%)	62 (62.6)	21 (45.7)	41 (77.4)	
Present, n (%)	37 (37.4)	25 (54.3)	12 (22.6)	
Intranodal vascular pattern				< 0.001
Hilar, n (%)	35 (35.4)	2 (4.3)	33 (62.2)	
Nonhilar, n (%)	64 (64.6)	44 (95.7)	20 (37.8)	

US: ultrasound; LNs: lymph nodes.

Foundation for Statistical Computing, Vienna, Austria) and MedCalc version 22.014 (Statistical Software version, Ostend, Belgium).

RESULTS

A total of 107 LNs were evaluated; eight were excluded due to an indeterminate FNAB and belonged to UNN-RADS categories 1 (5/8) and 2 (3/8). Ninety-nine LNs of 99 patients who underwent thyroid cancer follow-up were included (Figure 1), of which 53 (53.5%) were negative and 46 (46.5%) were positive for LN metastases. A benign or malignant LN diagnosis was confirmed by cytopathologic examination: 38 cases were diagnosed

as PTC, four as ATC, three as MTC, and one as FTC. A comparison of the frequency of the seven ultrasonographic descriptors in malignant and benign LN is shown in Table 2. The mean age was 48 ± 14.6 years; 70.7% (70/99) were females, and 29.3% (29/99) were males. At least one of the seven descriptors was found in each of the LNs. The seven ultrasonographic features were significantly associated with metastatic LNs.

Score-weighted US features and UNN-RADS categories

The likelihood of malignant or benign LN was based on the total score. Table 3 shows a comparison of

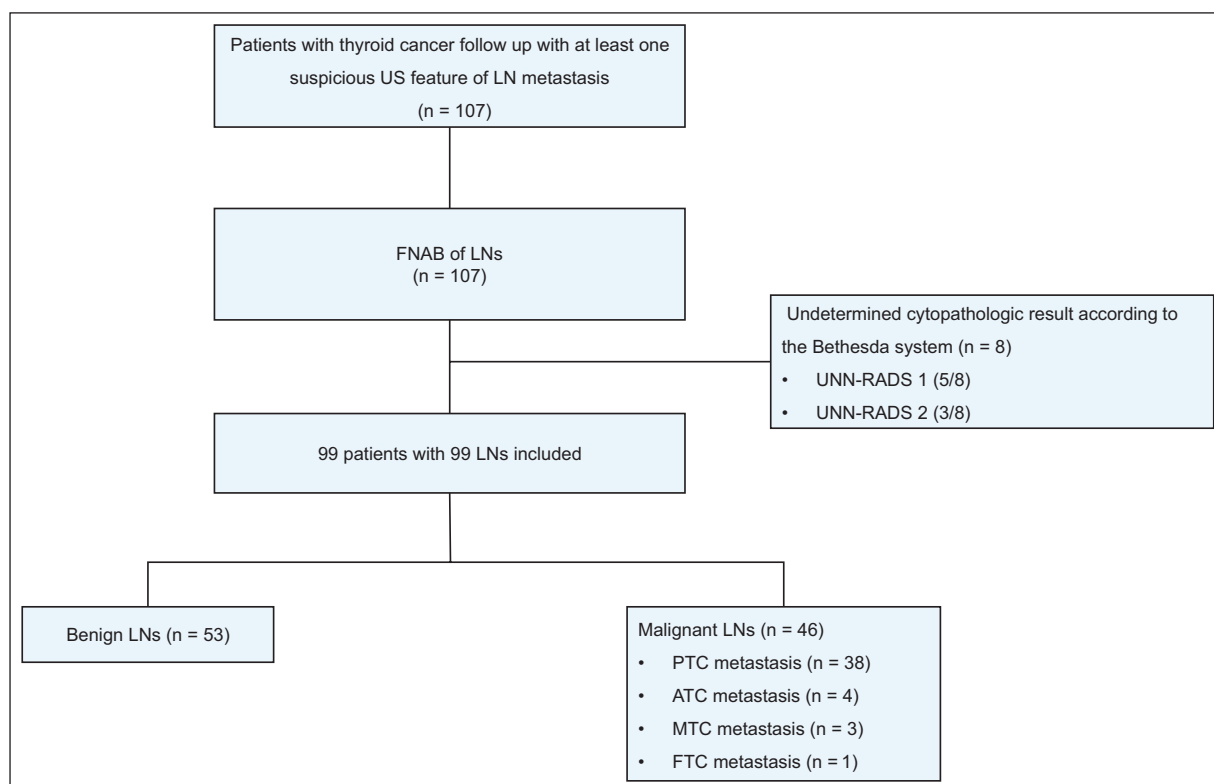


Figure 1. Flowchart of the study population. Ninety-nine LNs from 99 patients were followed for thyroid cancer. The diagnosis of benign or malignant LN was confirmed by cytopathologic examination. There were 53 (53.5%) negatives and 46 (46.5%) positives for LN metastases.

ATC: anaplastic thyroid carcinoma; FNAB: fine-needle aspiration biopsy; FTC: follicular thyroid carcinoma; LNs: lymph nodes; MTC: medullary thyroid carcinoma; PTC: papillary thyroid carcinoma; UNN-RADS: Ultrasound Neck Node Reporting and Data System; US: ultrasound.

scoring and UNN-RADS categories between metastatic and benign LN with cytopathologic confirmation in the follow-up of thyroid cancer patients. Twenty-one (100%) of 21 and 14 (100%) of 14 benign LNs were categories 1 and 2, respectively. The US features of benign LNs with cytopathologic confirmation with a weighted score corresponding to UNN-RADS categories 1 and 2 are shown in Figures 2 and 3.

All metastatic LNs belonged to UNN-RADS categories 3 (22/46), 4 (15/46), and 5 (9/46). There was a higher proportion of metastatic LNs with increasing category in 22 (59.5%) of 37 LNs classified as UNN-RADS category 3, 15 (93.8%) of 16 as category 4, and 9 (81.8%) of 11 as category 5. The US features of benign LNs with cytopathologic confirmation and a weighted score corresponding to UNN-RADS categories 1 and 2 are shown in Figures 4 and 5. No malignant LNs were diagnosed in categories 1 (benign) and 2 (probably benign), while the increased likelihood of malignancy in categories 3–5 was related to an increase in the UNN-RADS category score.

Diagnostic performance of UNN-RADS

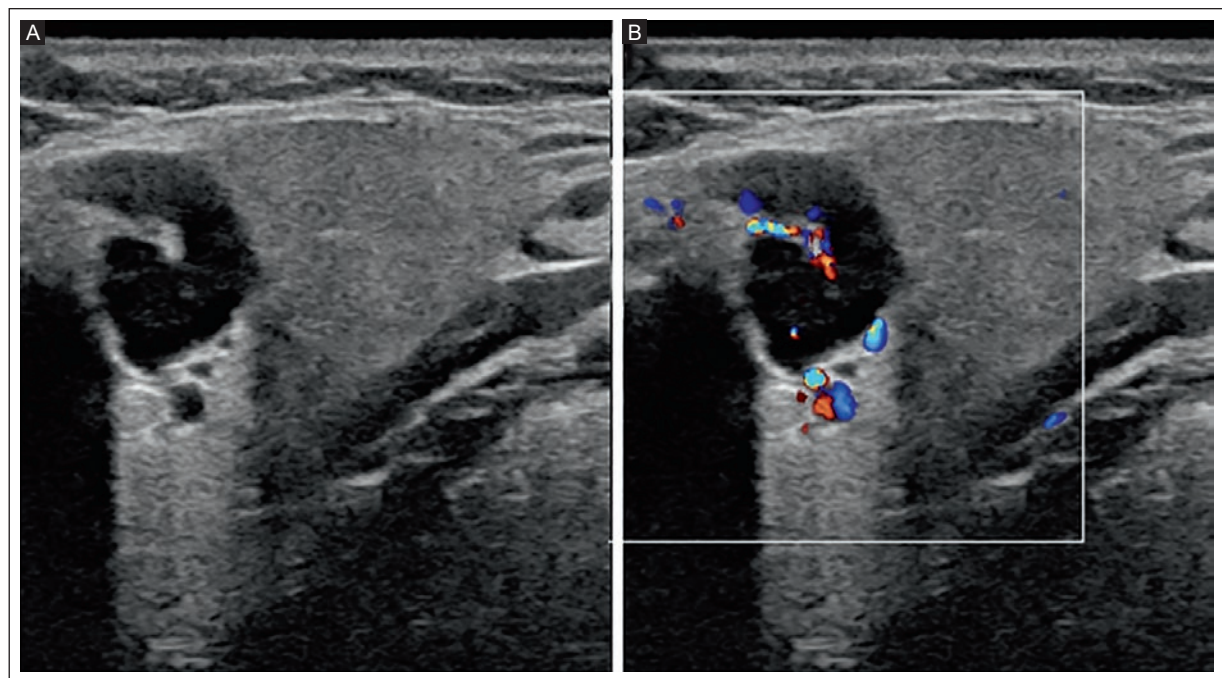
The ROC curve determined that the optimal cut-off value was equal to or greater than 6 points of the weighted score of US features for predicting malignant LN confirmed by cytopathology in thyroid cancer follow-up patients. The AUC ROC was high (0.893, 95% CI 81.5-94.6) (Figure 6). This value corresponded to UNN-RADS category 3.

The diagnostic performance of UNN-RADS for predicting metastatic LN in patients undergoing thyroid cancer follow-up using a weighted score ≥ 6 points showed a sensitivity of 100% (95% CI, 92.3-100), an NPV of 100% (95% CI, 90.0-100), and an accuracy of 81.6% (95% CI, 72.5-88.7) (Table 4). However, we found a low specificity (66%, 95% CI of 51.7-78.5) and a PPV of 71.4% (95% CI of 63.2-78.4). There were true positive results in 46 (100%) of 46 malignant LNs categorized as 3, 4, or 5, and true negative results in 35 (100%) of 35 benign LNs categorized as UNN-RADS 1 and 2. In contrast, false positives were found in 18

Table 3. Comparison of metastatic and benign LNs with cytopathologic confirmation by US features according to weighted UNN-RADS scoring and categories in the follow-up of patients with thyroid cancer

Score	≤ 3	4-5	6-8	9-11	≥ 12
Category	1	2	3	4	5
	Benign	Probably benign	Mildly suspicious for malignancy	Moderately suspicious for malignancy	Highly suspicious for malignancy
Benign LNs, n (%)	21 (100)	14 (100)	15 (40.5)	1 (6.2)	2 (18.2)
Metastatic LNs, n (%)	0	0	22 (59.5)	15 (93.8)	9 (81.8)
Total, n	21	14	37	16	11

UNN-RADS: Ultrasound Neck Node Reporting and Data System; LNs: lymph nodes; US: ultrasound.

**Figure 2.** A 28-year-old woman undergoing PTC follow-up. **A:** grayscale US, longitudinal view shows an oval LN, with an echogenic hilum < 25% (3 points) and a circumscribed margin. **B:** doppler color shows hilar vascularity. The LN was classified as UNN-RADS category 1 (total 3 points). The FNAB result was benign.

FNAB: fine-needle aspiration biopsy; LNs: lymph nodes; PTC: papillary thyroid carcinoma; UNN-RADS: Ultrasound Neck Node Reporting and Data System; US: ultrasound.

(34.0%) of 53 cases with benign LNs categorized as UNN-RADS 3, 4, or 5. There were no false negatives.

Interobserver agreement

The interobserver agreement between the radiologists classifying the seven US features suspicious for malignant LNs was good ($\kappa = 0.71$, 95.0% CI 0.573-0.798).

DISCUSSION

This study is the first to evaluate the diagnostic performance of UNN-RADS for predicting malignant LNs. We found optimal sensitivity and a negative positive value for detecting metastatic LNs in the follow-up of a cohort of thyroid cancer patients and no false negative results, making UNN-RADS an ideal diagnostic tool based on US features for predicting malignant LNs. UNN-RADS accurately defined the ultrasonographic features and reported

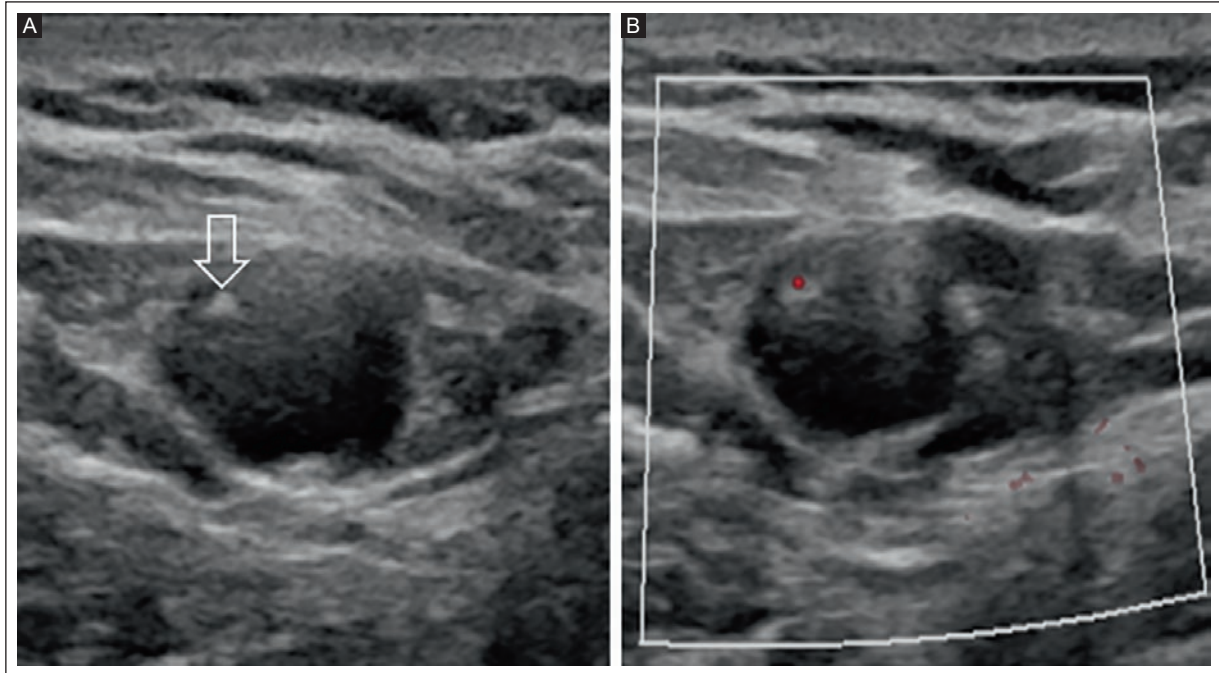


Figure 3. A 50-year-old woman undergoing PTC follow-up. **A:** grayscale US, longitudinal view shows a round-shaped LN (2 points) with an echogenic hilum < 25% (3 points) (arrow) and a circumscribed margin. **B:** doppler color shows hilar vascularity. The LN was classified as UNN-RADS category 2 (total 5 points). The FNAB result was benign.

FNAB: fine-needle aspiration biopsy; LN: lymph node; PTC: papillary thyroid cancer; UNN-RADS: Ultrasound Neck Node Reporting and Data System; US: ultrasound.

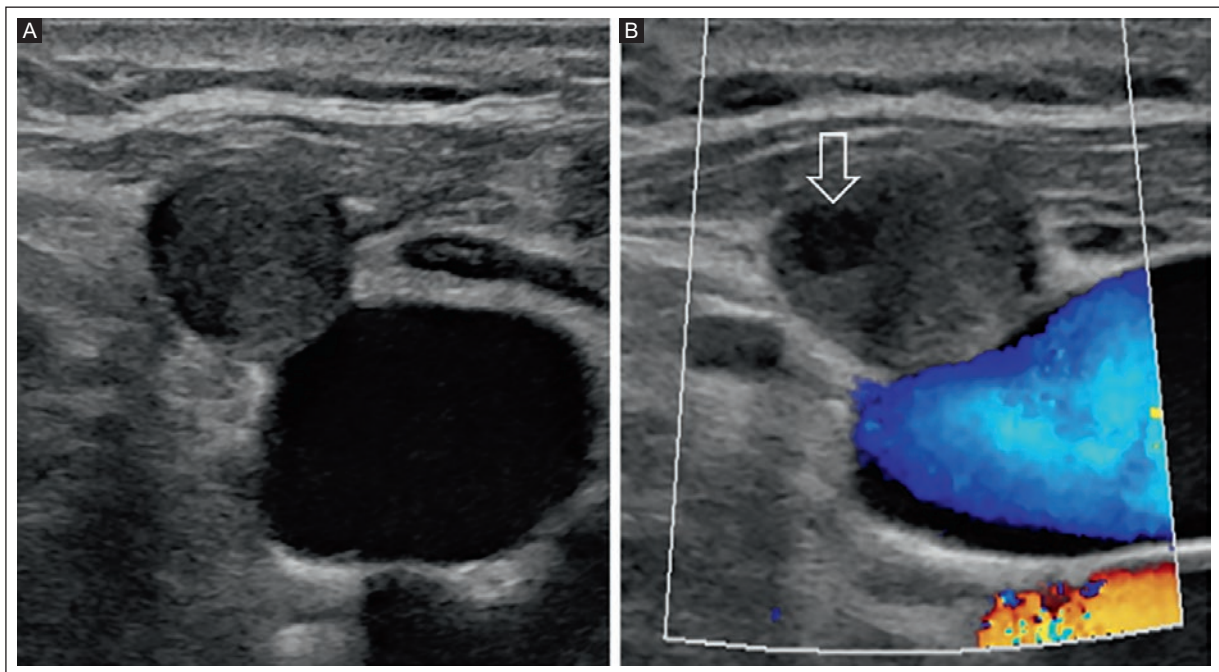


Figure 4. A 49-year-old woman undergoing an MTC follow-up. **A:** grayscale US, longitudinal view shows a round-shaped LN (2 points), absent hilum (3 points), and hyperechogenic (2 points) with a circumscribed margin. **B:** doppler US shows no vascularity, and cystic degeneration (3 points) with posterior acoustic enhancement (arrow). The LN was classified as UNN-RADS category 4 (total 10 points). The FNAB result was positive for MTC metastasis.

FNAB: fine-needle aspiration biopsy; LNs: lymph nodes; MTC: medullary thyroid cancer; UNN-RADS: Ultrasound Neck Node Reporting and Data System; US: ultrasound.

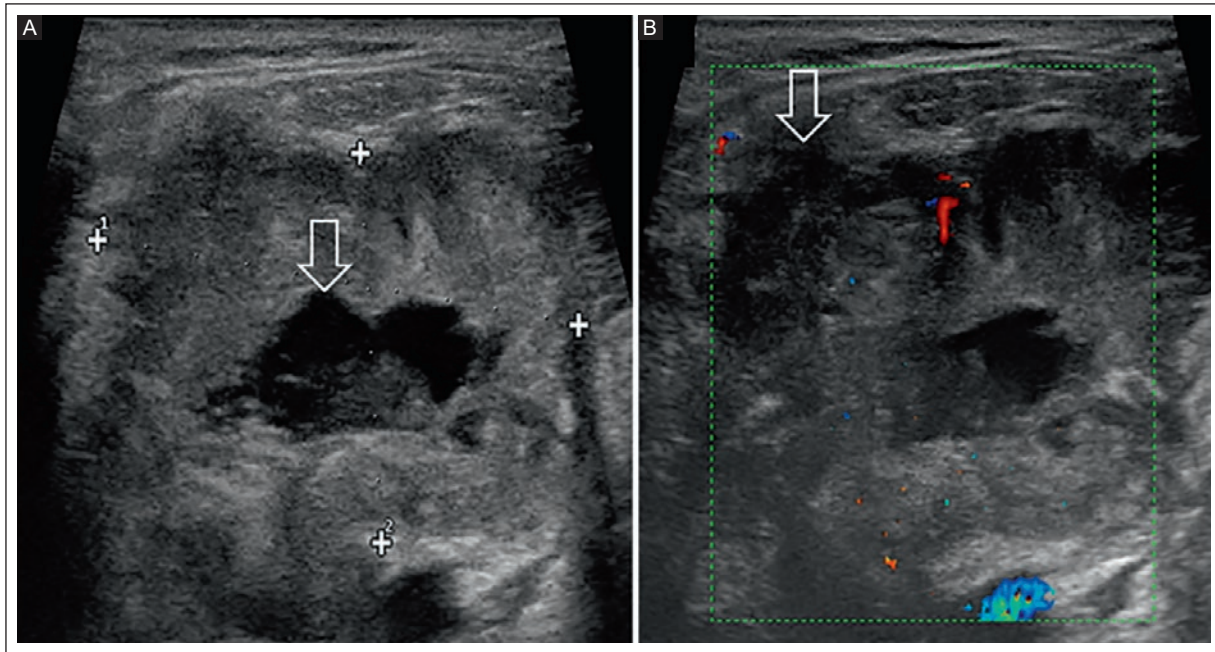


Figure 5. A 53-year-old man undergoing PTC follow-up. **A:** grayscale US, longitudinal view shows a round-shaped LN (2 points), absent hilum (3 points), cystic degeneration (3 points) (arrow), and hyperechogenic (2 points). **B:** doppler US shows nonhilar vascularity (2 points) with a non-circumscribed margin (1 point) (arrow). The LN was classified as UNN-RADS category 5 (total 13 points). The FNAB result was positive for PTC metastasis.

FNAB: fine-needle aspiration biopsy; LN: lymph node; PTC: papillary thyroid cancer; UNN-RADS: Ultrasound Neck Node Reporting and Data System; US: ultrasound.

the findings and recommendations for biopsy or follow-up in neck lymphadenopathy.

UNN-RADS combines a weighted score of seven US features, such as a round or lobulated shape, a non-circumscribed margin, hyperechogenicity, an echogenic hilum < 25% or absent, cystic degeneration, the presence of calcifications, and a nonhilar vascular pattern, that increase the predictability of malignant LNs¹⁸. In our study, the likelihood of malignancy was found in categories 3-5, and a higher proportion of metastatic LNs was associated with a higher UNN-RADS score. This observation is supported by the ROC curve, which showed that a cut-off score of 6 or more points had a sensitivity and an NPV of 100% with a high AUC (0.893), indicating excellent diagnostic performance in metastatic LN. We validated the usefulness of the combined weighted score of US features suspicious for malignancy defined by UNN-RADS in the follow-up of thyroid cancer patients.

Risk stratification by UNN-RADS categories for predicting malignant LN was originally reported by Sarda et al.¹⁸ All cases with LN metastases from primary head and neck cancers were classified as UNN-RADS categories 3, 4, or 5¹⁸. Metastatic LNs in our study belonged to

UNN-RADS categories 3, 4, or 5. Moreover, in categories 4 and 5, the number of benign cases decreased, and the number of malignant cases increased. On the contrary, 15 (40.5%) benign LNs in category 3 underwent FNAB according to the UNN-RADS recommendation because of mildly suspicious malignancy. Despite this high proportion of benign LN cases, an FNAB should be performed considering the risk-benefit of the procedure.

It is a real challenge to differentiate benign and metastatic LNs on US as a chronic inflammatory or infectious process may show calcifications, cortical or peripheral vascularity, a loss of morphology, cortex hyperechogenicity, cystic changes, and, in some cases, a non-circumscribed margin due to perinodal inflammation¹⁶. All our cases classified as UNN-RADS categories 1 and 2 were benign LNs. On the contrary, only a small proportion of cases in UNN-RADS categories 4 (1/16) or 5 (2/11), which were found to have a chronic infectious etiology, showed benign results. This finding is similar to Sarda et al.¹⁸, where all LNs in UNN-RADS categories 1 and 2 were benign. Their cases included mainly lymphoid hyperplasia, acute or chronic inflammatory processes, and infections. We found a low specificity (66.0%) in our study, which was mainly

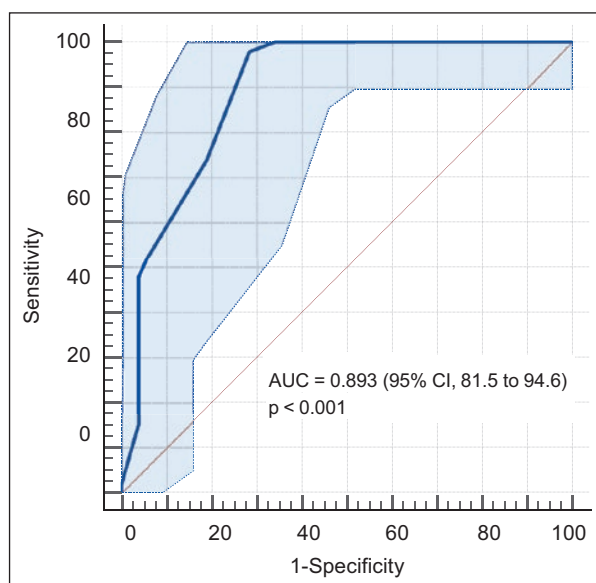


Figure 6. UNN-RADS diagnostic performance. The ROC curve defines that the optimal cut-off was equal to or greater than 6 points of the weighted score of US features for predicting malignant LN confirmed by cytopathology in patients undergoing thyroid cancer follow-up.

AUC: area under the curve; LNs: lymph nodes; ROC: receiver operating characteristic; UNN-RADS: Ultrasound Neck Node Reporting and Data System; US: ultrasound.

Table 4. Diagnostic performance of UNN-RADS for predicting metastatic LNs in thyroid cancer patient follow-up

Parameter	Value	95% CI
Sensitivity	100%	92.3-100
Specificity	66.0%	51.7-78.5
Positive predictive value	71.4%	63.2-78.4
Negative predictive value	100%	90.0-100
Positive likelihood ratios	2.9	2.0-4.3
Accuracy	81.6%	72.5-88.7

UNN-RADS: Ultrasound Neck Node Reporting and Data System; LNs: lymph nodes.

related to benign UNN-RADS category 3 LNs ($n = 15$, 40.5%), suggesting a moderate probability of predicting benign LNs. This finding contrasts with the high probability of correctly identifying benign LNs when cases are classified as UNN-RADS categories 1 and 2. Therefore, UNN-RADS categories 1 and 2 can reliably predict benign LNs.

Moderate interobserver agreement in assessing individual US features suspicious for malignant LN has

been previously reported^{1,20}. The UNN-RADS is a combined scoring system that weighs the US findings of seven features suspicious of malignancy. Therefore, interobserver agreement must be determined in an independent cohort study before its clinical use can be recommended¹⁸. Our study showed good interobserver agreement ($\kappa = 0.71$) between two radiologists with 10 and 11 years of experience. The UNN-RADS is a reproducible tool, even among less experienced radiologists compared with a head and neck radiologist with 30 years of experience from the paper by Sarda et al.¹⁸ We used a structured template of the seven descriptors of suspected malignancy to report the US features¹⁸. This template allowed us to standardize and systematize the identification and reporting of US findings.

The strengths of this study include the fact that all benign and malignant LNs were confirmed by FNAB, which is the reference standard, and that the sample size was sufficient to meet the study objectives. The limitations of the study are that it is a single center with a specific population of patients with thyroid cancer, and we do not perform complementary assessments with other imaging modalities.

CONCLUSION

This study showed that UNN-RADS has high diagnostic performance for predicting metastatic LNs with a good interobserver agreement in the follow-up of thyroid cancer patients. We considered that a scoring system based on the weighted score of seven malignancy-suspicious US findings is more accurate than a single feature in predicting malignant LNs. We believe that the inclusion of UNN-RADS in the follow-up of patients with thyroid cancer may help reduce the number of unnecessary biopsies. Further prospective and multicenter studies in different populations are needed before UNN-RADS can be widely used.

Acknowledgments

The authors thank Doctor Luz Faviola Velazquez and Doctor Omar Sanchez Figueroa for their important role as mentors in the Radiology Residency Program and for always encouraging us, and the Mexican Social Security Institute for being an important part of the medical training of future radiologists in Mexico. The authors thank Professor Ana M. Contreras-Navarro for her guidance in preparing and writing this scientific paper.

Funding

This research received no external funding.

Conflicts of interest

The authors declare that they have no conflicts of interest.

Ethical disclosures

Protection of individuals. This study complied with the Declaration of Helsinki (1964) and its amendments.

Confidentiality of data. The authors declare they followed their center's protocol for sharing patient data.

Right to privacy and informed consent. Informed consent was obtained from prospectively enrolled participants and waived for retrospectively enrolled patients.

Use of artificial intelligence. The authors did not use generative artificial intelligence to prepare this manuscript and/or create tables, figures, or figure legends.

REFERENCES

1. Chung SR, Baek JH, Rho YH, Choi YJ, Sung TY, Song DE, et al. Sonographic Diagnosis of Cervical Lymph Node Metastasis in Patients with Thyroid Cancer and Comparison of European and Korean Guidelines for Stratifying the Risk of Malignant Lymph Node. *Korean J Radiol.* 2022; 23(11):1102–1111. doi: 10.3348/kjr.2022.0358.
2. Lee JY, Yoo RE, Rhim JH, Lee KH, Choi KS, Hwang I, et al. Validation of Ultrasound Risk Stratification Systems for Cervical Lymph Node Metastasis in Patients with Thyroid Cancer. *Cancers (Basel).* 2022; 14(9):2106. doi: 10.3390/cancers14092106.
3. Ha EJ, Chung SR, Na DG, Ahn HS, Chung J, Lee JY, et al. 2021 Korean Thyroid Imaging Reporting and Data System and Imaging-Based Management of Thyroid Nodules: Korean Society of Thyroid Radiology Consensus Statement and Recommendations. *Korean J Radiol.* 2021; 22(12):2094–2123. doi: 10.3348/kjr.2021.0713.
4. Chasen NN, Wang JR, Gan Q, Ahmed S. Imaging of Cervical Lymph Nodes in Thyroid Cancer: Ultrasound and Computed Tomography. *Neuroimaging Clin N Am.* 2021; 31(3):313–326. doi: 10.1016/j.nic.2021.04.002.
5. Ahuja AT, Ying M. Sonographic evaluation of cervical lymph nodes. *AJR Am J Roentgenol.* 2005; 184(5):1691–1699. doi: 10.2214/ajr.184.5.01841691.
6. Mao Y, Hedgire S, Harisinghani M. Radiologic Assessment of Lymph Nodes in Oncologic Patients. *Curr Radiol Rep.* 2014; 36(2):1–13. doi:10.1007/s40134-013-0036-6.
7. Moharram MA, Abd-ElMaboud NM, Ahmed HA. Evaluation of the role of sono-elastography in diagnosis of enlarged cervical lymph nodes. *Egypt J Radiol Nucl Med.* 2017; 2(48):381–391. doi.org/10.1016/j.ejrmm.2017.01.009.
8. Filetti S, Durante C, Hartl D, Leboulleux S, Locati LD, Newbold K, et al. Thyroid cancer: ESMO Clinical Practice Guidelines for diagnosis, treatment and follow-up. *Ann Oncol.* 2019; 30(12):1856–1883. doi: 10.1093/annonc/mdz400.
9. Heřman J, Sedláčková Z, Fürst T, Vachutka J, Salzman R, Vomáčka J, et al. The role of ultrasound and shear-wave elastography in evaluation of cervical lymph nodes. *Biomed Res Int.* 2019; 2019:4318251. doi: 10.1155/2019/4318251.
10. Desmots F, Fakhry N, Mancini J, Reyre A, Vidal V, Jacquier A, et al. Shear Wave Elastography in Head and Neck Lymph Node Assessment: Image Quality and Diagnostic Impact Compared with B-Mode and Doppler Ultrasonography. *Ultrasound Med Biol.* 2016; 42(2):387–398. doi: 10.1016/j.ultrasmedbio.2015.10.019.
11. Learned KO, Lev-Toaff AS, Brake BJ, Wu RI, Langer JE, Loevner LA. US-guided biopsy of neck lesions: The head and neck neuroradiologist's perspective. *Radiographics.* 2016; 36(1):226–243. doi: 10.1148/rg.2016150087.
12. Meyer JE, Steffen A, Bienemann M, Hedderich J, Schulz U, Laudien M, et al. Evaluation and development of a predictive model for ultrasound-guided investigation of neck metastases. *Eur Arch Otorhinolaryngol.* 2012; 269(1):315–320. doi: 10.1007/s00405-011-1611-1.
13. Rohan K, Ramesh A, Sureshkumar S, Vijayakumar C, Abdulbasith K, Krishnaraj B. Evaluation of B-Mode and Color Doppler Ultrasound in the Diagnosis of Malignant Cervical Lymphadenopathy. *Cureus.* 2020;12(8):e9819. doi: 10.7759/cureus.9819.
14. Jayapal N, Ram S, Murthy V, Basheer S, Shamsuddin S, Khan A. Differentiation between benign and metastatic cervical lymph nodes using ultrasound. *J Pharm Bioallied Sci.* 2019; 11(2):338–346. doi: 10.4103/JPBS.JPBS_26_19.
15. Elsholtz FHJ, Asbach P, Haas M, Becker M, Beets-Tan RG, Thoeny HC, et al. Introducing the Node Reporting and Data System 1.0 (Node-RADS): a concept for standardized assessment of lymph nodes in cancer. *Eur Radiol.* 2021; 31(8):6116–6124. doi: 10.1007/s00330-020-07572-4.
16. Ahuja AT, Ying M, Ho SY, Antonio G, Lee YP, King AD, et al. Ultrasound of malignant cervical lymph nodes. *Cancer Imaging.* 2008; 8(1):48–56. doi: 10.1102/1470-7330.2008.0006.
17. Cheng PC, Chang CM, Liao LJ, Cheng PW, Lo WC. The outcomes and decision-making process for neck lymph nodes with indeterminate fine-needle aspiration cytology. *PLoS One.* 2021; 16(2):246437. doi: 10.1371/journal.pone.0246437.
18. Sarda-Inman ED, Valdez-Rojas AM. Ultrasound Neck Node Reporting and Data System (UNN-RADS) for lymphadenopathy: A structured report. *J Mex Fed Radiol Imaging.* 2022; 1(3):151–163. doi: 10.24875/JMEXFRI.M22000020.
19. Cohen JF, Korevaar DA, Altman DG, Bruns DE, Gatsonis CA, Hooft L, et al. STARD 2015 guidelines for reporting diagnostic accuracy studies: explanation and elaboration. *BMJ Open.* 2016; 6(11):12799. doi: 10.1136/bmjopen-2016-012799.
20. Ryu KH, Lee KH, Ryu J, Baek HJ, Kim SJ, Jung HK et al. Cervical lymph node imaging reporting and data system for ultrasound of cervical lymphadenopathy: a pilot study. *AJR Am J Roentgenol.* 2016;206(6):1286–1291. doi:10.2214/AJR.15.15381.

Paramagnetic rim lesions on 1.5T and 3.0T MRI in Mexican patients with multiple sclerosis

Rebeca de J. Ramos-Sanchez¹ , Roger A. Carrillo-Mezo¹, Yazmin Martinez-Lopez², Jose Flores-Rivera², and Hector Ramirez-Flores¹

¹Department of Neuroimaging; ²Department of Neuroimmunology. Instituto Nacional de Neurología y Neurocirugía “Manuel Velasco Suarez”, Mexico City, Mexico

ABSTRACT

Introduction: Paramagnetic rim lesions (PRLs) in multiple sclerosis (MS) patients have been described with different magnetic field strengths in magnetic resonance imaging (MRI). This study aimed to identify the characteristics of PRLs in magnitude and filtered phase susceptibility weighted imaging (SWI/SWAN) in 1.5T and 3.0T MRI in Mexican patients with MS and to determine interobserver agreement. **Materials and methods:** This retrospective cross-sectional study assessed adults with MS who underwent 1.5T or 3.0T MRI with SWI/SWAN. The variables, sex, age, MS duration, annualized relapse rate, the severity of current disability determined by the Expanded Disability Status Scale (EDSS), the MS clinical phenotype, and the presence, number, location, and volume of PRLs were assessed. Cohen's kappa was used to calculate interobserver agreement. **Results:** A total of 76 patients with MS were included. At least one PRL was found in 60 (78.9%). A total of 375 PRLs were detected: 233 in 42 (76.4%) of 55 patients with 1.5T MRI with a mean of 5.54 per patient and 142 PRLs in 18 (85.7%) of 21 patients with 3.0T MRI with a mean of 7.9 per patient. The most common location was periventricular ($n = 49$, 81.7%). A significant association was found between PRLs and younger patients ($p = 0.017$), a shorter disease evolution ($p = 0.010$), an annualized relapse rate ($p = 0.030$), and a higher volume of white matter lesions ($p = 0.035$). Interobserver agreement was good ($\kappa = 0.709$, 95% CI, 0.702–0.716). **Conclusion:** This study is the first in Mexico that characterizes PRLs with 1.5T and 3.0T MRI magnetic fields in patients with MS with good interobserver agreement.

Keywords: Multiple sclerosis. Chronic active lesion. Paramagnetic rim lesion. Magnetic resonance imaging. Susceptibility weighted imaging.

INTRODUCTION

Conventional magnetic resonance imaging (MRI) is standard in clinical practice and drug trials in multiple sclerosis (MS) for diagnosis, prognosis, monitoring disease activity, and assessing therapy. Paramagnetic rim lesions (PRLs) in magnitude and filtered phase susceptibility weighted imaging (SWI/SWAN) are prognostic

biomarkers in MS patients¹⁻⁴. PRLs reflect chronic perilesional inflammation and persisting demyelinating activity of residual iron-loaded microglia^{2,5,6}; therefore, they are a sign of chronic active inflammation⁷. However, their clinical significance in MS is unclear.

MRI and post-mortem studies show that PRLs edge-related iron accumulation is captured by a rim-shaped signal around chronic white matter lesions

*Corresponding author:

Rebeca de J. Ramos-Sanchez

E-mail: rramossanchez25@gmail.com

Received for publication: 17-01-2024

Accepted for publication: 30-01-2024

DOI: 10.24875/JMeXFRi.24000005

Available online: 22-03-2024

J Mex Fed Radiol Imaging. 2024;3(1):27-35

www.JMeXFRi.com

2696-8444 / © 2024 Federación Mexicana de Radiología e Imagen, A.C. Published by Permanyer. This is an open access article under the CC BY-NC-ND (<https://creativecommons.org/licenses/by-nc-nd/4.0/>).

Table 1. Characteristics of MS patients categorized by PRLs in 1.5T and 3.0T MRI

Characteristics	Total (n = 76)	MS patients with PRLs (n = 60)	MS patients without PRLs (n = 16)	p-values
Age, years	38.3 ± 11.2	36.7 ± 11.0	44.4 ± 9.8	0.017
Female, n (%)	44 (57.9)	34 (56.7)	10 (62.5)	0.675
Male, n (%)	32 (42.1)	26 (43.3)	6 (37.5)	0.675
MRI field strength				
1.5T, n (%)	55 (72.4)	42 (70.0)	13 (81.2)	
3.0T, n (%)	21 (27.6)	18 (30.0)	3 (18.8)	
Decreased normalized brain volume				
White matter, n (%)	52 (68.4)	43 (71.7)	9 (56.2)	0.242
Gray matter, n (%)	31 (40.7)	27 (45.0)	4 (25.0)	0.151
WML volume, cm ³	23.49 ± 21.2	25.85 ± 21.9	14.19 ± 15.7	0.035

MRI: magnetic resonance imaging; MS: multiple sclerosis; PRLs: paramagnetic rim lesions; WML: white matter lesions. The values refer to the mean ± SD unless otherwise stated.

Table 2. Characteristics of PRLs in 1.5T and 3.0T MRI in MS patients

Characteristics	Parameters
Prevalence of patients with ≥ 1 PRL, n (%)	60 (78.9)
Patients with non-PRL, n (%)	16 (21.1)
Total, n (%)	76 (100)
Patients with PRLs by MRI field strength	
1.5T, n (%)	42 (70.0)
3.0T, n (%)	18 (30.0)
Total, n (%)	60 (100)
PRLs number related to MRI field strength	
1.5T, n (%)	233 (62.2)
3.0T, n (%)	142 (37.8)
Total, n (%)	375 (100)
Number of PRLs per patient	
All patients, mean ± SD	6.25 ± 5.9
Patients examined with 1.5T, mean ± SD	5.54 ± 5.23
Patients examined with 3.0T, mean ± SD	7.88 ± 7.1
PRLs volume, cm ³	1.62 ± 1.9

MRI: magnetic resonance imaging; MS: multiple sclerosis; PRLs: paramagnetic rim lesions.

(WML) with SWI/SWAN MRI^{5,7-9}. These chronic active lesions are common and associated with more aggressive MS disease, exert ongoing tissue

damage. They even occur in individuals treated with effective disease-modifying therapies^{7,8}. MRI studies have shown that PRLs, previously detected only at autopsy, are identified *in vivo* as non-gadolinium-enhanced chronic lesions with a paramagnetic rim on 7.0T, 4.7T, 3.0T, or 1.5T susceptibility-based MRI^{7,10}. PRLs have been proposed as imaging markers of smoldering MS. The prevalence of PRLs varies due to differences in scanner resolution. Few studies have evaluated the use of 1.5T and 3.0T MRI in detecting PRLs in MS¹¹. This study aimed to identify the characteristics of PRLs on 1.5T and 3.0T MRI with susceptibility-weighted sequences in Mexican patients with MS and to determine interobserver agreement.

MATERIALS AND METHODS

This retrospective cross-sectional study was conducted from January to July 2023 in the Department of Neuroimaging of the National Institute of Neurology and Neurosurgery “Manuel Velasco Suarez” in Mexico City, Mexico. We included patients diagnosed with MS from the Demyelinating Diseases Clinic according to the 2017 revised McDonald criteria¹² and referred for routine follow-up with MRI. Patients with an incomplete MRI were excluded. Informed consent was not required to analyze and publish data obtained as part of routine medical care. The institutional research and ethics committee approved the protocol.

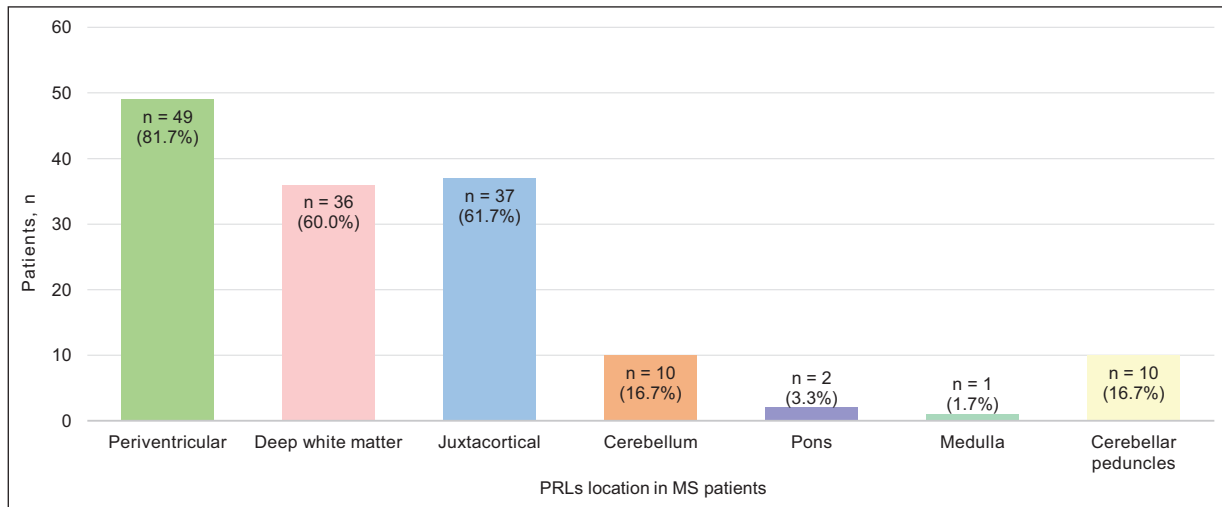


Figure 1. MRI location of PRLs in 60 patients with MS. A few patients had more than one site.

PRLs: paramagnetic rim lesions; MRI: magnetic resonance imaging; MS: multiple sclerosis.

Table 3. Clinical characteristics categorized by the presence or absence of PRLs in MS patients

Characteristics	Total (n = 76)	MS patients with PRLs (n = 60)	MS patients without PRLs (n = 16)	p-values
MS duration, years	9.28 ± 8.18	8.05 ± 7.71	13.56 ± 8.89	0.010
MS annualized relapse rate	0.24 ± 0.26	0.27 ± 0.27	0.13 ± 0.26	0.030
EDSS score	4.5 ± 2.39	4.4 ± 2.36	4.53 ± 2.59	0.934
Clinical phenotype				0.198
RRMS, n (%)	61 (80.3)	50 (83.4)	11 (68.7)	
SPMS, n (%)	13 (17.1)	8 (13.3)	5 (31.3)	
PPMS, n (%)	2 (2.6)	2 (3.3)	0	

MRI: magnetic resonance imaging; MS: multiple sclerosis; PRLs: paramagnetic rim lesions; EDSS: Expanded Disability Status Scale; RRMS: relapsing-remitting multiple sclerosis; SPMS: secondary progressive multiple sclerosis; PPMS: primary progressive multiple sclerosis. The values refer to the mean ± SD unless otherwise stated.

Study development and variables

Demographic data and the MS clinical history were obtained from patient records. The variables used were sex, age, MS duration, annualized relapse rate, the severity of current disability determined by the Expanded Disability Status Scale (EDSS), and MS clinical phenotype: relapsing-remitting (RRMS), secondary-progressive (SPMS), or primary progressive (PPMS).

According to Vanheule et al.¹, PRL is a hypointense lesion with ring morphology and a circumference greater than 75%. The authors changed this definition, assuming that the lesion must be visible in at least two

Table 4. Interobserver agreement according to the number of PRLs in 1.5T and 3.0T MRI in MS patients

Description	κ	95% CI
≥ 1 PRL	0.709	0.702-0.716
1-3 PRLs	0.464	0.456-0.471
≥ 4 PRLs	0.730	0.723-0.737

MRI: magnetic resonance imaging; MS: multiple sclerosis; PRLs: paramagnetic rim lesions.

continuous SWI/SWAN MRI images, corresponding to a hyperintense lesion on FLAIR. In the original definition, three or more contiguous slices were required¹.

Lesions with a nodular pattern in a single slice on SWI/SWAN or enhancement in the contrasted T1-W post-gadolinium sequences were excluded.

Patients were grouped according to the presence or absence of PRLs. The number, volume, and location of PRLs, the decrease in age-normalized WM and gray matter (GM) volume, the total volume of WML, and post-contrast enhancement lesions were recorded. The PRL locations were described as periventricular, deep WM, juxtacortical WM, midbrain, pons, medulla, cerebellum, and cerebellar peduncles.

Image acquisition and analysis protocol

MRI was performed with a SIGNA™ Explorer 1.5T (GE HealthCare, Chicago, IL, USA) or a MAGNETOM Skyra 3.0T (Siemens Medical Solutions, Erlangen, Germany). Structural MRI with SWI/SWAN in 1.5T or 3.0T magnetic fields was performed in all patients.

1.5T MRI parameters: 3D SWAN, TR: 78.4 ms, TE: 50 ms, slice thickness: 1.5 mm, reconstructed voxel size: $0.9 \times 0.9 \times 1.5$ mm, acquisition time: 7 minutes 13 seconds; T1 3D, TR: 6.8 ms, TE: 2.6 ms, slice thickness: 1 mm, reconstructed voxel size: $1.1 \times 1.1 \times 1.0$ mm, acquisition time: 4 minutes 16 seconds; and 3D FLAIR, TR: 6000 ms, TE: 120 ms, TI: 1874 ms, slice thickness: 0.60 mm, reconstructed voxel size: $1.2 \times 1.2 \times 1.2$ mm, acquisition time: 5 minutes 45 seconds.

3.0T MRI parameters: 3D SWAN, TR: 36 ms, TE: 20 ms, slice thickness: 1.5 mm, reconstructed voxel size: $0.9 \times 0.9 \times 1.5$ mm, acquisition time: 7 minutes 9 seconds; T1 3D, TR: 500 ms, TE: 11 ms, slice thickness: 1 mm, reconstructed voxel size: $0.8 \times 0.8 \times 1.0$ mm, acquisition time: 6 minutes 29 seconds; and 3D FLAIR, TR: 5000 ms, TE: 386 ms, TI: 1800 ms, slice thickness: 1.00 mm, reconstructed voxel size: $0.5 \times 0.5 \times 1.0$ mm, acquisition time: 7 minutes 7 seconds.

Brain volume was determined by converting 3D T1 and 3D FLAIR images from DICOM to NIFTI format. Automatic segmentation was performed using the free online software volBrain and lesionBrain (<https://vol-brain.net/>). The PRL volume was defined by manual segmentation in the PACS system (Carestream Health, Toronto, Canada). Images were analyzed by a neuroradiologist (RCM) with 21 years of experience and a second-year neuroradiology resident (RRS) at workstations with medical-grade displays. Interobserver agreement between the two readers regarding the presence of PRLs was assessed. Agreement on the number of PRLs (1-3 versus ≥ 4) was also compared. Readers were blinded to the patient's clinical data.

In cases where the readers disagreed, the score was determined by consensus.

Statistical analysis

Quantitative variables are described as means, standard deviations, and ranges. The t-test or the Mann-Whitney U test was used to compare means. Dichotomous qualitative variables were compared with the chi-square or Fisher's exact test. Cohen's kappa coefficient for the two raters' lesion classifications was calculated using unweighted categories (PRLs vs. non-PRLs). P-values less than 0.05 were statistically significant. Statistical analyses were performed using IBM SPSS v26.0 (IBM Corp. Armonk, NY, USA).

RESULTS

Ninety-three MS patients were studied. Eight were excluded due to incomplete MRI sequences, seven had enhancement in the T1-W contrasted sequences post gadolinium, and two had no contrasted sequence. Table 1 shows the characteristics of MS patients categorized by the presence or absence of PRLs in the magnetic fields of 1.5T and 3.0T MRI. Seventy-six patients were included: 44 (57.9%) women and 32 (42.1%) men. The mean age was significantly lower in patients with PRLs (36.7 ± 11.0 years) than in patients without PRLs (44.4 ± 9.8 years) ($p = 0.017$). Regarding field strength, 55 (72.4%) of the 76 patients underwent 1.5T MRI, and 21 (27.6%) underwent 3.0T MRI. When brain volumetry was analyzed, 52 (68.4%) of the 76 patients had decreased WM volume, and 31 (40.7%) had decreased GM volume. PRLs were more common in patients with decreased WM volume ($n = 43$, 71.7%) than in patients with decreased GM volume ($n = 27$, 45.0%). The volume of WML was significantly higher in patients with PRLs (25.85 ± 21.9 cm³) than in those without PRLs (14.19 ± 15.7) ($p = 0.035$).

Table 2 describes the characteristics of PRLs in magnetic fields of 1.5T and 3.0T MRI. At least one PRL was found in 60 of 76 patients, with a prevalence of 78.9%. We found 375 PRLs, 233 in 42 of 55 patients evaluated with 1.5T MRI and 142 in 18 of 21 patients evaluated with 3.0T MRI. The number of PRLs detected per patient was 7.9 at 3.0T, with 142 PRLs in 18 (85.7%) of 21 patients evaluated, compared with 5.54 per patient at 1.5T with 233 in 42 (76.4%) of 55 patients. Figure 1 shows the location of PRLs: periventricular WM ($n = 49$, 81.7%), juxtacortical WM ($n = 37$, 61.7%), deep WM ($n = 36$, 60.0%), cerebellum ($n = 10$, 16.7%), cerebellar

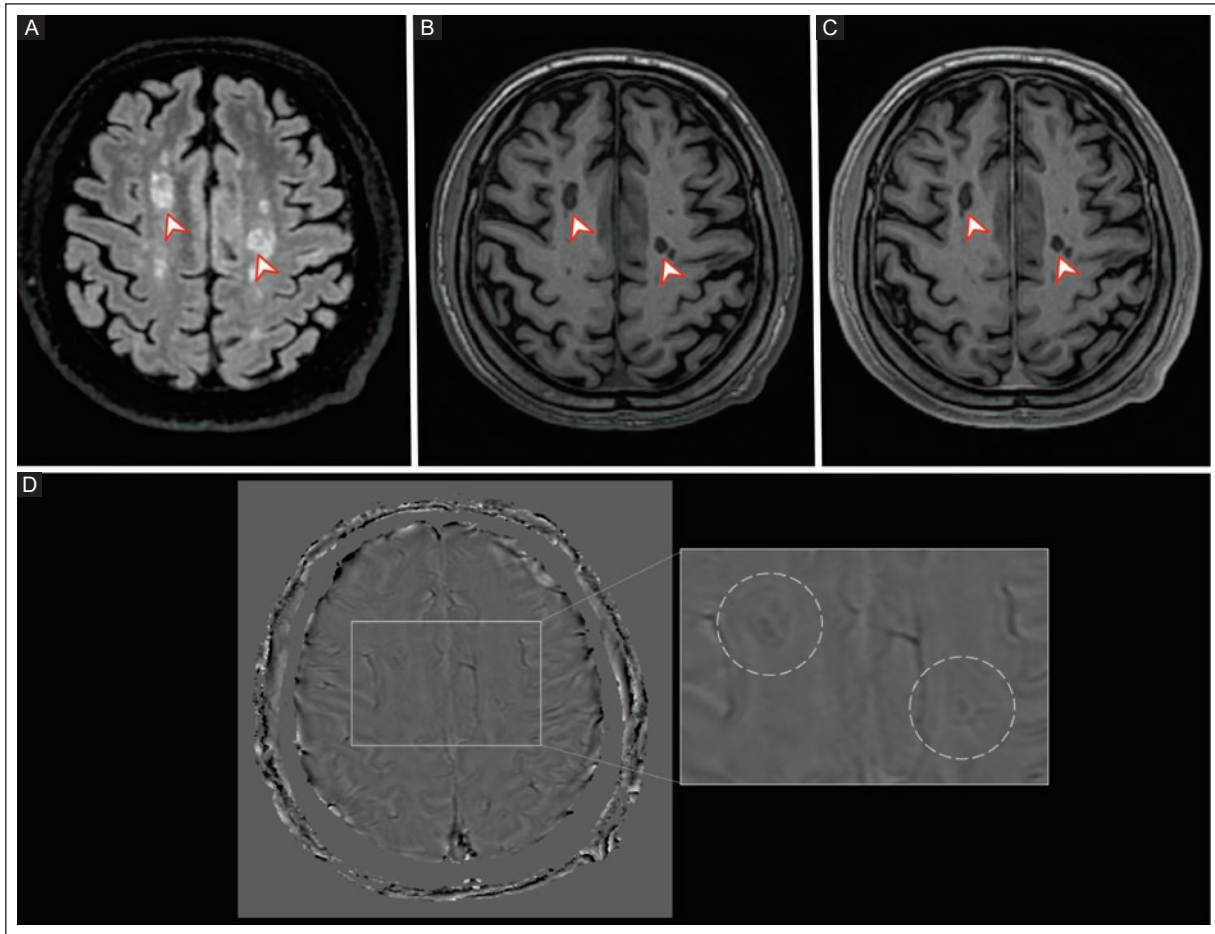


Figure 2. Structural 1.5T MRI of a 57-year-old man with PPMS with 5 years of disease evolution. **A:** axial FLAIR view showing multiple oval and round demyelinating lesions in the juxtacortical and deep WM with two larger lesions in the deep WM of both frontal lobes (arrowheads). **B:** axial T1-weighted view shows marked hypointensity of the two largest lesions (arrowheads), indicating a chronic lesion stage with WM destruction. **C:** axial T1-weighted post-gadolinium with no evidence of WM enhancement (arrowheads). **D:** axial filtered-phase SWAN shows PRL with a completely hypointense rim in the two largest lesions (dotted circles in the inset). A central venous sign is observed in both lesions.

MRI: magnetic resonance imaging; PPMS: primary progressive multiple sclerosis; FLAIR: fluid-attenuated inversion recovery; WM: white matter; SWAN: susceptibility-weighted angiography; PRL: paramagnetic rim lesion.

peduncles ($n = 10$ patients, 16.7%), pons ($n = 2$, 3.3%), and medulla ($n = 1$, 1.7%). No PRLs were identified in the midbrain. A few patients had PRLs in more than one location.

The duration of MS was significantly shorter in patients with PRLs compared with those without PRLs (8.05 ± 7.71 and 13.56 ± 8.89 years, respectively) ($p = 0.010$) (Table 3). In contrast, the annualized MS relapse rate was significantly higher in patients with PRLs (0.27 ± 0.27) than in patients without PRLs (0.13 ± 0.26) ($p = 0.30$). On the contrary, EDSS was comparable between the two groups. The clinical phenotype RRMS was the most common, with no significant difference between the clinical phenotypes and the presence or absence of PRLs.

The agreement between the two observers in identifying PRLs was good ($\kappa = 0.709$, 95% CI, 0.702–0.716) (Table 4). On the contrary, agreement was slightly better for PRLs ≥ 4 ($\kappa = 0.730$, 95% CI, 0.723–0.737) compared with one to three lesions ($\kappa = 0.464$, 95% CI, 0.456–0.471). A higher number of PRLs improved interobserver agreement.

Figure 2 shows the structural MRI of a 57-year-old man with PPMS after 5 years of disease progression. Axial filtered-phase SWAN shows PRL with a complete hypointense rim in the two most prominent lesions. A central vein sign is observed in both lesions. In contrast, Figure 3 shows the structural MRI of a 37-year-old woman with RRMS after 13 years of disease evolution

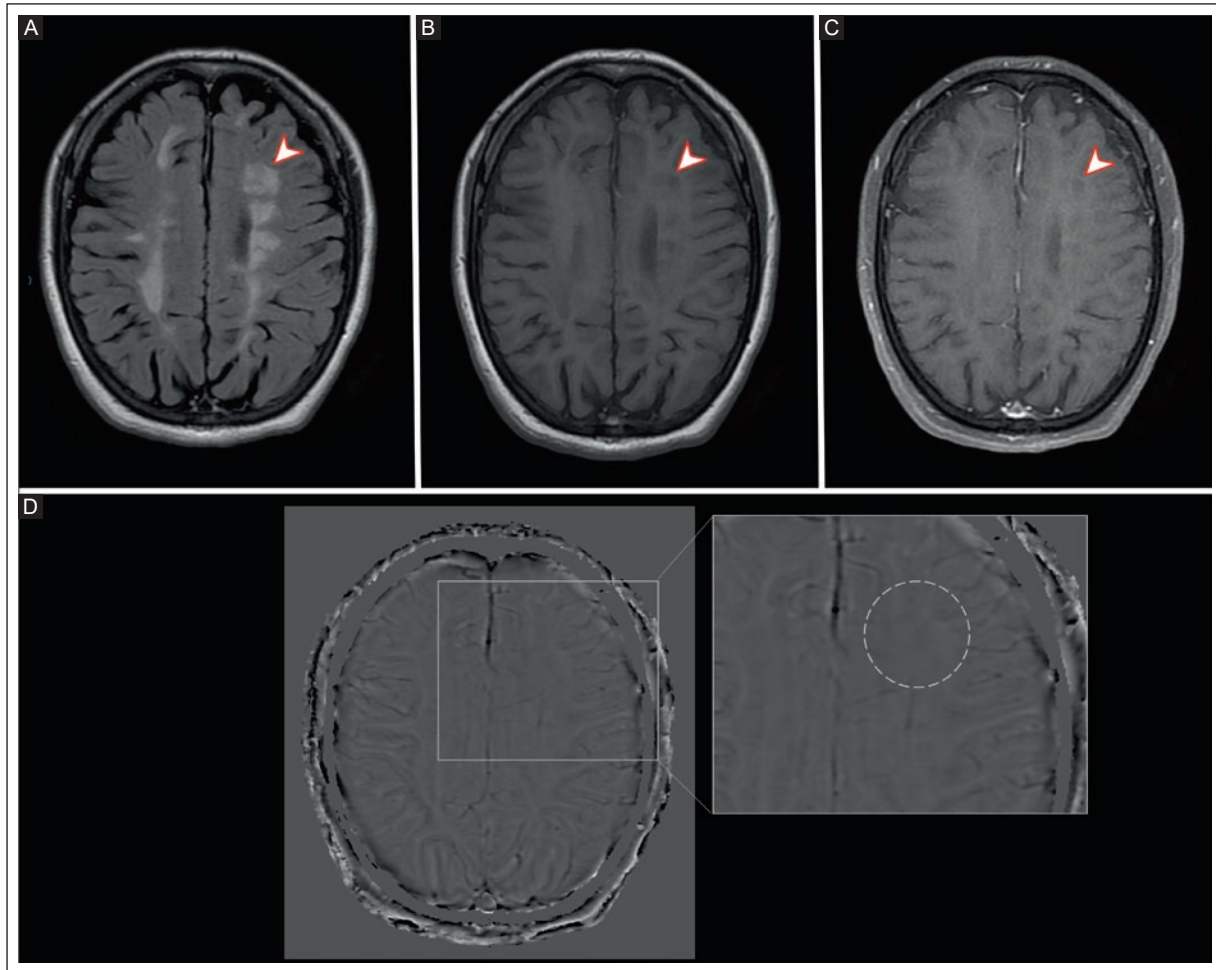


Figure 3. Structural 1.5T MRI of a 37-year-old woman with RRMS with 13 years of disease evolution. **A:** axial FLAIR view showing multiple periventricular and juxtacortical demyelinating lesions, one with a periventricular location in the left frontal region (arrowhead). **B:** axial T1-weighted view showing hypointensity of the left frontal periventricular lesion (arrowhead), indicating a chronic stage of the lesion with WM destruction. **C:** axial T1-weighted post-gadolinium. There was no evidence of WM lesion enhancement (arrowhead). **D:** in the axial filtered-phase SWAN, the PRL is absent in the left frontal lesion (dotted circles in the inset).

MRI: magnetic resonance imaging; RRMS: relapsing-remitting multiple sclerosis; FLAIR: fluid-attenuated inversion recovery; WM: white matter; SWAN: susceptibility-weighted angiography; PRL: paramagnetic rim lesion.

without a PRL in the left frontal lesion. Figure 4 shows four clinical cases with different PRL locations detected with 1.5T or 3.0T MRI.

DISCUSSION

This study is the first in Mexico that characterizes PRLs in 1.5T and 3.0T MRI. A high prevalence (78.9%) was found with at least one PRL in four out of five patients with MS, regardless of sex and clinical phenotype. Magnitude and filtered phase susceptibility weighted imaging (SWI/SWAN) should be included in the conventional MRI protocol to identify PRLs in MS patients.

The prevalence of PRLs in MS patients has been reported with a wide range. In a systematic mapping review that included 38 studies published between February 2001 and January 2020, the prevalence of PRLs ranged from 10% to 72%⁷. The MRI techniques used to detect PRLs in these studies were different, namely, quantitative susceptibility mapping (QSM), SWI, R2*, and FLAIR with mixed use of different magnetic field MRI scanners⁷. Absinta et al.⁸ reported a prevalence of PRLs of 56% (n = 117) in a cohort of 209 patients, regardless of treatment or clinical phenotype. On the contrary, Maggi et al.² reported a prevalence of 52.3% (n = 172) in a retrospective study of 329 patients with MS. In contrast, a lower prevalence was reported

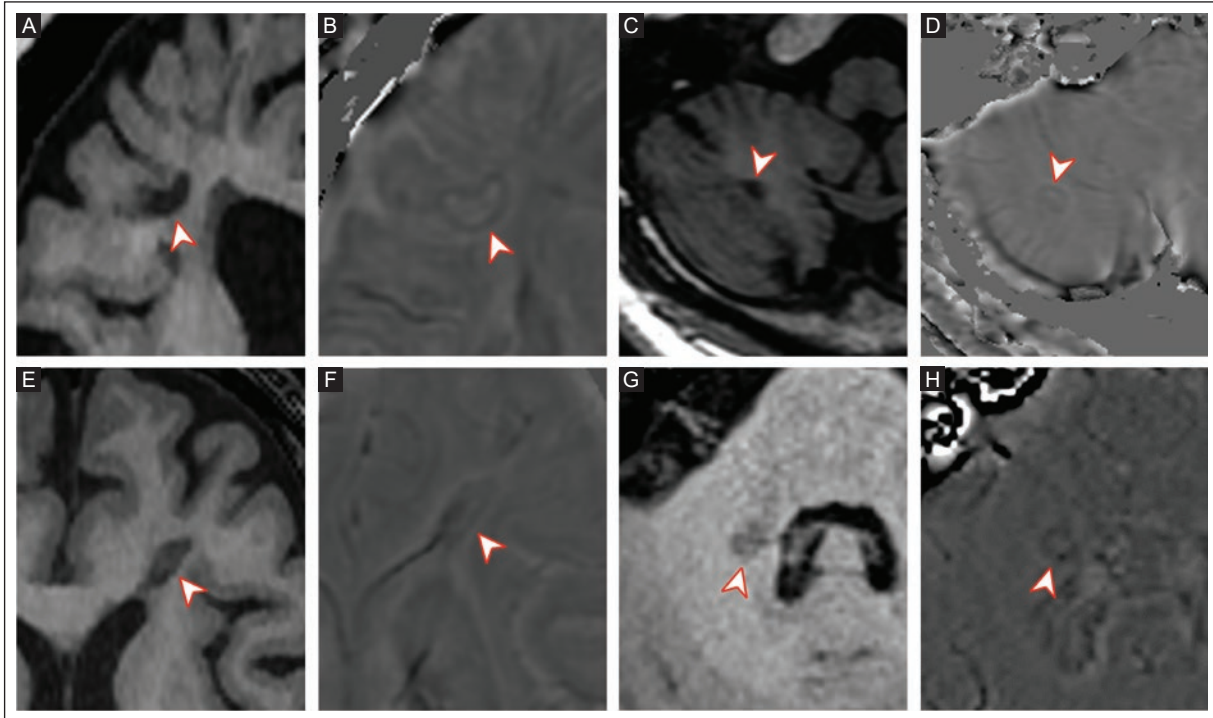


Figure 4. Structural MRI of four patients with MS, each with a different localization of PRLs. **A:** a 37-year-old woman with RRMS with 2 years of disease evolution. T1-weighted image with markedly hypointense juxtacortical WML (arrowhead). **B:** axial filtered-phase SWAN, showing the PRL at the same location with a complete hypointense rim (arrowhead). **C:** a 24-year-old male with RRMS and 3 years of disease evolution. T1-weighted image with markedly hypointense WML in the cerebellum (arrowhead). **D:** axial filtered-phase SWAN, showing PRL at the same location with a complete hypointense rim (arrowhead). **E:** a 40-year-old male with RRMS with 8 years of disease evolution. T1-weighted image with markedly hypointense periventricular WML or “black hole” (arrowhead). **F:** axial filtered-phase SWAN showing PRL at the same location with a complete hypointense rim (arrowhead). The sign of the central vein is also observed. **G:** a 29-year-old male with PPMS with 2 years of disease evolution. T1-weighted image with markedly hypointense WML in the right middle cerebellar peduncle (arrowhead). **H:** axial filtered-phase SWI, showing the PRL at the same location with a complete hypointense rim (arrowhead).

MRI: magnetic resonance imaging; MS: multiple sclerosis; RRMS: relapsing-remitting multiple sclerosis; PPMS: primary progressive multiple sclerosis; WML: white matter lesions; SWAN: susceptibility-weighted angiography; SWI: susceptibility weighted imaging; PRL: paramagnetic rim lesion.

by Vanheule et al.¹ in a retrospective cross-sectional study of 84 patients with MS. PRLs were found in 27 (32.1%) cases. A total of 125 PRLs were detected, with a mean of 4.6 ± 3.82 per patient and a maximum of 14. Our study found at least one PRL in 60 of 76 patients, with a prevalence of 78.9%. The mean number of PRLs per patient was high (6.25 ± 5.9). The higher prevalence in our study may be because the population was from a national center with a high degree of specialization, where MS patients with higher clinical severity are referred; therefore, it may not reflect the true prevalence of a newly diagnosed population.

Many MRI scanners used in clinical practice operate at 1.5T, but few studies have examined their performance characterizing PRLs in MS patients. In one systematic mapping review, 15 studies (39.5%) used only 7.0T, while 13 studies (34.2%) used 3.0T, and four

studies (10.5%) used 3.0T and 7.0T. Two studies used 1.5T (5.3%), and one used 4.7T (2.6%)⁷. Hemond et al.¹¹ showed comparable performances between 1.5T and 3.0T MRI field strengths. They did not observe a more significant number of PRLs at 3.0T than at 1.5T. In contrast, in our study, a higher number and percentage of PRLs per patient were detected at 3.0T (7.9 per patient) in 18 (85.7%) of 21 patients, compared with 1.5T (5.54 per patient) in 42 (76.4%) of 55 patients. This finding means a higher number and percentage of PRLs were detected at 3.0T. On the other hand, the agreement between a neuroradiologist with 21 years of experience and a second-year resident in neuroradiology in detecting PRLs was good ($\kappa = 0.709$) and was slightly higher for PRLs ≥ 4 ($\kappa = 0.730$) than for one to three lesions ($\kappa = 0.464$). A higher number of PRLs improved interobserver agreement. Comparable results

were reported with good interrater agreement ($\kappa = 0.65$ at 1.5T and 0.70 at 3.0T) between a neurologist with 5 years of experience in MS neuroimaging and a neuroradiologist with 15 years of experience¹¹. A retrospective evaluation with 3.0T MRI from a multicenter study of five hospitals showed good interobserver agreement ($\kappa = 0.79$) between two evaluators². In a retrospective cross-sectional study of 84 patients with 3.0T MRI by Vanheule et al.¹, the interobserver agreement between a neuroradiologist with 34 years of experience and a general radiologist in training with 3 years of experience was almost perfect regarding the presence of PRLs ($\kappa = 0.98$) and excellent regarding the number of PRLs ($\kappa = 0.90$). It should be kept in mind that this study is the first in Mexico to describe PRLs, indicating a lack of experience in identifying this finding, which is not usually intentionally sought when evaluating a routine MRI in MS patients¹¹. The most common reasons for discordant interrater PRL classifications include vascular complexity and poor signal or contrast. However, the interobserver agreement appears comparable at 1.5T and 3.0T MRI field strengths¹¹.

PRLs are frequently observed around the ventricles in MS patients. In a systematic mapping review,⁷ the location of PRLs was shown in only 5 of 38 studies. In three studies, the periventricular location was more common, while in juxtacortical and deep GM, PRLs were reported with comparable frequency. In our study, periventricular WM was the most common location ($n = 40$, 81.7%). In addition, PRLs were found in infratentorial sites such as the cerebellar peduncle ($n = 10$, 16.7%), the cerebellum ($n = 10$, 16.7%), and the pons ($n = 2$, 3.3%). It is comparable with other studies. This finding could be due to the higher number of periventricular demyelinating lesions in MS.

The relationship of PRLs to age, sex, phenotype, and clinical course in MS patients has discordant results. In a systematic mapping review,⁷ only 7 of 38 studies reported an association with sex and age, indicating that PRLs were more common in young men. In contrast, other authors^{1,2,8} found no significant association between PRLs and age or disease duration. In our study, PRLs were found in younger patients compared with patients without PRLs (36.7 ± 11.0 and 44.4 ± 9.8 years, respectively) ($p = 0.017$) and in those with a shorter disease evolution (8.05 ± 7.71 years vs. 13.56 ± 8.89 years) ($p = 0.010$). Similar to previous reports, PRLs in our study were significantly more common in younger patients and with shorter disease evolution^{5,7}. No significant differences were found regarding sex. It has been reported that PRLs decrease by 3% per year

with increasing age and disease duration⁷. Published data on PRLs in the early stages of MS or at the time of clinical presentation are limited⁷, so it is not possible to confirm that the increased prevalence of PRLs in patients with shorter disease duration reflects more generalized inflammatory activity.

This study has limitations. These include the cross-sectional, retrospective, single-center study design and the small sample size. In addition, no external reference standard for the presence of PRLs was available, so false positives and negatives could not be identified. Vascular complexity and artifacts in magnetic susceptibility sequences are associated with false negative results in patients with fewer PRLs (≤ 3). In addition, manual PRL segmentation was performed, which is difficult and time-consuming and may result in inter- and intra-observer variation. It is estimated that interpretation of the susceptibility features of each MS lesion would take several minutes of a radiologist's time for examinations with multiple lesions¹¹. Furthermore, we did not assess a possible association between disease-modifying treatments and the presence of PRLs.

CONCLUSION

This study presents the characteristics of PRLs in Mexican MS patients evaluated with field strengths of 1.5T and 3.0T MRI. We propose promoting magnetic susceptibility-based sequences in the routine protocol for MS for the purpose of identifying PRLs at the start of the disease and as a routine yearly evaluation. Evidence for the prognostic and diagnostic utility of PRLs is still emerging and lacks comprehensive replication, especially on different MRI platforms and field strengths¹¹. Studies with different MRI scanners and prospective cohorts of MS patients are needed.

Acknowledgments

The authors thank Professor Ana M. Contreras-Navarro for her guidance in preparing and writing this scientific paper.

Funding

This research received no external funding.

Conflicts of interest

The authors declare no conflicts of interest.

Ethical disclosures

Protection of individuals. This study complies with the Declaration of Helsinki (1964) and its subsequent amendments.

Confidentiality of data. The authors declare that they followed their center's protocol for sharing patient data.

Right to privacy and informed consent. Informed consent was not required for this observational study of information collected during routine clinical care.

Use of artificial intelligence. The authors state that they did not use generative artificial intelligence to prepare this manuscript and/or create tables, figures, or figure legends.

REFERENCES

1. Vanheule E, Cambron M, Casselman JW, Dobai A. Rim lesions in MS at 3T: clinical correlation and possible radiological alternatives for daily practice at lower field strength. *J Neuroradiol.* 2023;S0150-9861(23)00262-00266. doi:10.1016/j.neurad.2023.10.010.
2. Maggi P, Sati P, Nair G, Cortese ICM, Jacobson S, Smith BR, et al. Paramagnetic Rim Lesions are Specific to Multiple Sclerosis: An International Multicenter 3T MRI Study. *Ann Neurol.* 2020;88(5):1034-1042. doi:10.1002/ana.25877.
3. Ng Kee Kwong KC, Mollison D, Meijboom R, York EN, Kampaite A, Thrippleton MJ, et al. The prevalence of paramagnetic rim lesions in multiple sclerosis: A systematic review and meta-analysis. *PLoS One.* 2021;16(9):e0256845. doi:10.1371/journal.pone.0256845.
4. Martire MS, Moiola L, Rocca MA, Filippi M, Absinta M. What is the potential of paramagnetic rim lesions as diagnostic indicators in multiple sclerosis? *Expert Rev Neurother.* 2022; 22(10): 829-837. doi:10.1080/14737175.2022.2143265.
5. Dal-Bianco A, Grabner G, Kronnerwetter C, Weber M, Höftberger R, Berger T, et al. Slow expansion of multiple sclerosis iron rim lesions: pathology and 7 T magnetic resonance imaging. *Acta Neuropathol.* 2017; 133(1):25-42. doi:10.1007/s00401-016-1636-z.
6. Clark KA, Manning AR, Chen L, Liu F, Cao Q, Bar-Or A, et al. Early Magnetic Resonance Imaging Features of New Paramagnetic Rim Lesions in Multiple Sclerosis. *Ann Neurol.* 2023;94(4):736-744. doi:10.1002/ana.26727.
7. AITokhis AI, AlOtaibi AM, Felmban GA, Constantinescu CS, Evangelou N. Iron Rims as an Imaging Biomarker in MS: A Systematic Mapping Review. *Diagnostics.* 2020;10(11):968. doi: 10.3390/diagnostics10110968.
8. Absinta M, Sati P, Masuzzo F, Nair G, Sethi V, Kolb H, et al. Association of Chronic Active Multiple Sclerosis Lesions With Disability In Vivo. *JAMA Neurol.* 2019;76(12):1474-1483. doi: 10.1001/jamaneurol.2019.2399.
9. Haacke EM, Makki M, Ge Y, Maheshwari M, Sehgal V, Hu J, et al. Characterizing iron deposition in multiple sclerosis lesions using susceptibility weighted imaging. *J Magn Reson Imaging.* 2009;29(3):537-44. doi:10.1002/jmri.21676.
10. Hagemeyer J, Heininen-Brown M, Poloni GU, Bergsland N, Magnano CR, Durfee J, et al. Iron deposition in multiple sclerosis lesions measured by susceptibility-weighted imaging filtered phase: a case control study. *J Magn Reson Imaging.* 2012;36(1):73-83. doi: 10.1002/jmri.23603.
11. Hemond CC, Reich DS, Dundamadappa SK. Paramagnetic Rim Lesions in Multiple Sclerosis: Comparison of Visualization at 1.5-T and 3-T MRI. *AJR Am J Roentgenol.* 2022;219(1):120-131. doi: 10.2214/AJR.21.26777.
12. Thompson AJ, Banwell BL, Barkhof F, Carroll WM, Coetzee T, Comi G, et al. Diagnosis of multiple sclerosis: 2017 revisions of the McDonald criteria. *Lancet Neurol.* 2018;17(2):162-173. doi:10.1016/S1474-4422(17)30470-2.

A descending enhancement pattern on CEM is associated with invasive breast cancer: the first Mexican experience

Silvia M. Gonzalez-Lopez^{1,2}, Yhessica Y. Lara-Zavala^{1,2}, Juan J. Biagi-de Leon^{1,2}
Karla G. Garcia-Alvarez³, and David F. Perez-Montemayor^{1,2}*

¹Centro de Imagenología Integral IMAX; ²Instituto de Estudios Superiores de Tamaulipas, Universidad Anahuac; ³Laboratorio de Patología, Hospital Beneficencia Española de Tampico. Tampico, Tamaulipas, Mexico

ABSTRACT

Introduction: There are few studies on the quantitative analysis and enhancement pattern of breast lesions on contrast-enhanced mammography (CEM). We performed a quantitative analysis and defined CEM enhancement patterns of malignant, benign with upgrade potential (BWUP), and benign breast lesions with a histopathologic correlation. **Materials and Methods:** A retrospective cross-sectional study of women with breast lesions showing CEM enhancement patterns was conducted with a confirmed histopathologic diagnosis. The quantitative CEM parameters were the contrast-to-noise ratio (CNR), the percentage signal ratio between the enhanced lesion and background (%RS), and the relative signal difference (RSD). The enhancement patterns analyzed were ascending, steady, and descending. **Results:** A total of 32 women with a mean age of 53.5 ± 11.1 (range 33–75) years with 36 breast lesions assessed by CEM were included. Histopathologic diagnoses were infiltrating breast carcinoma ($n = 13$, 36.1%), breast carcinoma in situ ($n = 2$, 5.5%), BWUP ($n = 4$, 11.1%), and benign breast lesions ($n = 17$, 47.2%). The ascending pattern was found in 16 (44.4%) of the 36 lesions, the descending enhancement pattern in 15 (41.7%), and the steady pattern in 5 (13.9%). The descending enhancement pattern was significantly more frequent in infiltrating breast carcinomas ($n = 9$, 60.0%) ($p = 0.018$), while carcinoma in situ ($n = 2$) showed an ascending pattern ($p = ns$). Benign and BWUP lesions were more likely to show an ascending pattern ($n = 9$ and $n = 3$, respectively) ($p = ns$). **Conclusion:** This is the first study in Mexico to present a quantitative analysis and enhancement patterns to better characterize breast lesions in CEM. The descending enhancement pattern provides useful information for predicting invasive breast cancer.

Keywords: Contrast-enhanced mammography. Recombined images. Quantitative CEM values. Breast cancer. Infiltrating breast carcinoma.

INTRODUCTION

Contrast-enhanced mammography (CEM) increases diagnostic accuracy in detecting breast cancer with higher specificity and similar sensitivity (93-100%) to conventional mammography and magnetic resonance imaging^{1,2}. CEM allows the assessment of the morphology and physiological characteristics of the breast

lesion by contrast enhancement³. Malignant lesions have immature vascular proliferation and increased microvascular permeability that allow the contrast agent to accumulate in and around the malignant tumor⁴.

Some malignant, benign with upgrade potential (BWUP), and benign lesions may have similar imaging features⁵. The first version of the BI-RADS® lexicon for CEM included only subjective qualitative descriptors of

*Corresponding author:

David F. Pérez-Montemayor
E-mail: dfperez@prodigy.net.mx

Received for publication: 12-01-2024

Accepted for publication: 25-01-2024

DOI: 10.24875/JMeXFRi.24000003

Available online: 22-03-2024

J Mex Fed Radiol Imaging. 2024;3(1):36-44

www.JMeXFRi.com

2696-8444 / © 2024 Federación Mexicana de Radiología e Imagen, A.C. Published by Permanyer. This is an open access article under the CC BY-NC-ND (<https://creativecommons.org/licenses/by-nc-nd/4.0/>).

defined internal enhancement patterns, extent of lesion enhancement, asymmetry enhancement, and conspicuity^{6,7}. Interestingly, a quantitative assessment of enhancement in low-energy and recombined images can improve the diagnostic performance of CEM. Few quantitative analyses of CEM have shown an association between increased enhancement and breast malignancy⁸⁻¹⁰. Moreover, contrast kinetics have been evaluated and categorized into three patterns: ascending, steady, and descending⁸. The descending pattern has been associated with an increased likelihood of breast malignancy⁸⁻¹⁰. It is crucial to differentiate breast carcinomas from benign breast lesions to improve the diagnostic performance of CEM¹⁰. Quantitative analysis of CEM enhancement can help differentiate malignant, BUWP, and benign breast lesions. This study focused on the quantitative analysis and CEM enhancement patterns with a histopathologic correlation of malignant, BWUP, and benign breast lesions.

MATERIALS AND METHODS

This retrospective cross-sectional study was conducted from September 2015 to June 2023 at the Centro de Imagenología Integral IMAX in Tampico, Tamaulipas, Mexico. Women with breast lesions on CEM and diagnosis confirmed by histopathology were included. Exclusion criteria were the lack of a histopathology report or incomplete imaging studies. Informed consent was not required for this retrospective data analysis obtained during routine medical care. The Institutional Research Ethics Committee and the Research Committee approved the study.

Study development and variables

CEM was performed in patients with clinically or ultrasonographically suspected breast lesions of malignancy. Patients with a breast lesion with enhancement on CEM and histopathologic confirmation of their diagnosis were identified in the institutional database. The first version of the BI-RADS® lexicon for CEM was used to describe subjective qualitative descriptors that define internal enhancement patterns, extent of lesion enhancement, asymmetric enhancement, and conspicuity⁶.

Quantitative CEM parameters

Contrast-to-noise ratio (CNR) is the difference in signal between lesion enhancement and background¹⁰:

$$CNR = \frac{LS - BS}{SD}$$

where LS is the lesion signal with the maximum pixel value in the region of interest (ROI) of the breast lesion¹⁰; BS is the background signal with the mean pixel value of the signal in the ROI of the background¹⁰; and SD is the standard deviation (pixels).

Percentage signal difference between enhancing lesion and background (%RS):

$$\%RS = \frac{LS - BS \times 100}{BS}$$

Relative signal difference (RSD) of the enhancement pattern:

$$RSD = \frac{CNR_{MLO} - CNR_{CC} \times 100}{CNR_{CC}}$$

CNR_MLO: CNR in the mediolateral oblique (MLO) projection.

CNR_CC: CNR in the caudal cranial (CC) projection.

CEM enhancement patterns

Two acquisition time points, the relative enhancement at early (CC view) and late (MLO view) net enhancement on the CEM, were recorded and classified as follows¹⁰:

Ascending pattern: The intensity of the enhancement showed a continuous increase state with an RSD > 10%¹⁰. Enhancement increased by more than 10% from the early to the late phase⁸.

Steady pattern: The enhancement intensity showed no notable difference between the two projections, with the absolute RSD value within 10%¹⁰. The enhancement changed within 10%⁸.

Descending pattern: The intensity of the enhancement is weaker in the latter position than in the former with an RSD ≤ 10%¹⁰. Enhancement decreased by more than 10%⁸.

Image acquisition and analysis

CONTRAST-ENHANCED MAMMOGRAPHY (CEM)

The CEM technique was performed with SenoBright™ (GE Medical Systems, Buc, France) equipment⁷. A peripheral intravenous line was placed in the antecubital fossa, and 1.5 mL/kg of an iodinated contrast

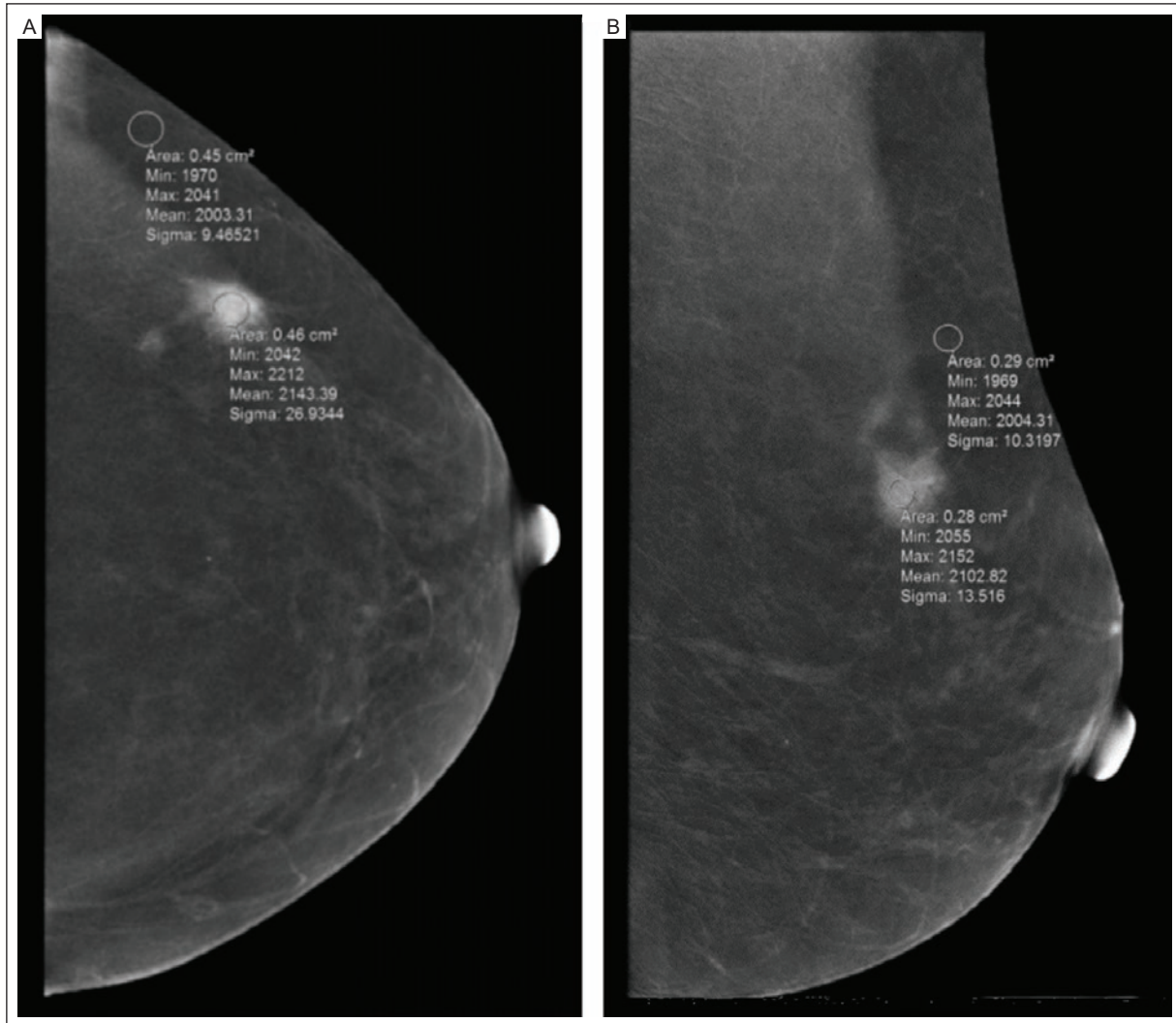


Figure 1. Quantitative measurement of the enhancement of breast lesions on CEM. **A:** RC CC view. **B:** RC MLO view shows an irregular, spiculated lesion with homogeneous internal enhancement and high conspicuity. The ROI was placed on the enhanced breast lesion and background area. The quantitative CNR was 15.7 in the CC view and 9.5 in the MLO view. A descending enhancement pattern was seen with an RSD value of -41.7%.

CC: craniocaudal view; CEM: contrast-enhanced mammography; CNR: contrast-to-noise ratio; MLO: mediolateral oblique; RC: recombined; ROI: region of interest; RSD: relative signal difference.

agent was administered at a rate of 3 mL/s (Omnipaque™ 300, GE Healthcare, Carrigtwohill Co. Cork, Ireland). The patient was positioned for two standard CC and MLO mammography projections of each breast at least 90 s after the injection. The CC and MLO projections of both breasts were performed with a delay of 2 min between each projection of the same breast. It started with the right breast and continued with the left breast. Images were obtained from the Picture Archiving and Communication System (PACS) (Synapse 5™, Fujifilm Medical Systems U.S.A., Inc.).

All CEM examinations were analyzed by the same breast radiologist (DPM) with 31 years of experience on a SecurView workstation (Hologic, Inc. Danbury, CT, USA) with 5 MP medical-grade monitors (BARCO, Kortrijk, Belgium). The region of interest (ROI) of the lesion with enhancement was recorded with the mean value of the calculated enhancement. A second ROI similar to the first was placed in an area without enhancement. Figure 1 illustrates the quantitative measure of the CEM signal values. The ROI was placed over the enhanced area of the lesion and the background area with pixel measurement to

Table 1. Histopathologic diagnosis of 36 breast lesions with enhancement on CEM

Infiltrating breast carcinoma	n (%)
Infiltrating ductal carcinoma	8 (61.5)
Infiltrating lobular carcinoma	2 (15.4)
Infiltrating ductal-lobular carcinoma	3 (23.1)
Total	13 (100)
In situ breast carcinoma	n (%)
Ductal carcinoma in situ	1 (50.0)
Ductal lobular carcinoma in situ	1 (50.0)
Total	2 (100)
BWUP	n (%)
Atypical ductal hyperplasia	3 (75.0)
Lobular carcinoma in situ	1 (25.0)
Total	4 (100)
Benign breast lesion	n (%)
Fibroadenoma	6 (35.3)
Complex fibroadenoma	2 (11.8)
Sclerosing adenosis	3 (17.6)
Fat necrosis	1 (5.9)
Mastitis/abscess	4 (23.5)
Fibrosis	1 (5.9)
Total	17 (100)

BWUP: benign with upgrade potential; CEM: contrast enhanced mammography.

calculate the CNR and evaluate the enhancement intensity. The RSD was calculated to assess the enhancement pattern. The ROIs of the background were as close as possible to the fatty components of the breast background and away from the enhanced lesion or the enhanced breast parenchymal tissue. ROI sizes varied according to the homogeneity of the pixel values between the lesion and noise areas. ROI values were evaluated separately for CC and MLO projections.

Ultrasound

LOGIC™ ultrasound (US) equipment (General Electric, Boston, MA, USA) with a linear multifrequency transducer of 10–16 MHz was used. The US grayscale and color Doppler images were stored in a PACS.

Breast US features were reported according to the BI-RADS¹¹. The US findings of three clinical cases are shown in the figures presented.

Breast biopsy

Breast biopsies were performed with a 14-gauge Bard™ needle (Bard Care, Covington, GA, USA) using the Bard Magnum System™. A pathologist (KGA) blinded to the patient's imaging findings and with 11 years of experience evaluated the biopsies and reported the histopathologic diagnosis.

Statistical analysis

A descriptive analysis of the numerical and categorical variables was performed. The mean, SD, minimum and maximum of CNR, %RS, and RSD were calculated. The association of the enhancement patterns (ascending, descending, or steady) with the histopathologic diagnosis was evaluated with the chi-square test with a significance of $p \leq 0.05$. Statistical analysis was performed with SPSS version 25 (IBM Corp., Armonk, NY, USA).

RESULTS

A total of 32 women with 36 breast masses with CEM enhancement were included. Two lesions were found in four patients. The mean (\pm SD) age was 53.5 ± 11.1 (range 33–75) years. Table 1 shows the histopathologic diagnoses: infiltrating breast carcinoma ($n = 13$, 36.1%), breast carcinoma in situ ($n = 2$, 5.5%), BWUP ($n = 4$, 11.1%), and benign lesions ($n = 17$, 47.2%).

Quantitative analysis of CEM enhancement

The quantitative CNR and %RS values of CEM enhancement of the 36 breast lesions in relation to histopathologic diagnosis are shown in Table 2. The highest mean value of CNR_{CC} and %RS_{CC} corresponded to infiltrating carcinoma (6.5 ± 3.3 and 3.7 ± 1.9 , respectively). In contrast, CNR and %RS in the MLO projection had comparable values between malignant, BWUP, and benign breast lesions.

Enhancement pattern of CEM

The quantitative RSD values of CEM enhancement are shown in Table 3. Infiltrating breast carcinomas had a mean RSD of -22.8 ± 39.7 , corresponding to a

Table 2. Quantitative CNR and %RS values of CEM enhancement in relation to histopathologic diagnosis in 36 breast lesions

Description	n	Mean \pm SD	Minimum	Maximum
CNR_CC				
Infiltrating breast carcinoma	13	6.5 \pm 3.3	2.7	15.4
In situ breast carcinoma	2	2.7 \pm 1.1	1.8	3.5
BWUP	4	3.2 \pm 0.5	2.7	3.8
Benign breast lesions	17	4.9 \pm 1.9	3.2	10.6
Total	36			
%RS_CC				
Infiltrating breast carcinoma	13	3.7 \pm 1.9	1.4	7.5
In situ breast carcinoma	2	1.9 \pm 1.0	1.1	2.6
BWUP	4	2.2 \pm 0.6	1.9	3.1
Benign breast lesions	17	2.9 \pm 2.4	1.4	12.0
Total	36			
CNR_MLO				
Infiltrating breast carcinoma	13	4.5 \pm 2.2	1.1	9.0
In situ breast carcinoma	2	4.2 \pm 1.8	2.9	5.6
BWUP	4	4.4 \pm 1.1	3.2	6.0
Benign breast lesions	17	5.0 \pm 3.2	0.2	12.5
Total	36			
%RS_MLO				
Infiltrating breast carcinoma	13	2.9 \pm 1.4	0.7	5.7
In situ breast carcinoma	2	2.6 \pm 1.3	1.6	3.6
BWUP	4	3.4 \pm 1.8	1.7	5.9
Benign breast lesions	17	2.7 \pm 1.9	0.1	8.2
Total	36			

CEM: contrast enhanced mammography; CNR: contrast to noise ratio; %RS: percentage signal difference between enhancement lesion and background; CC: craniocaudal; MLO: medio-lateral oblique; BWUP: benign with upgrade potential; SD: standard deviation.

descending enhancement pattern. Carcinoma in situ had a mean RSD of 6.1 ± 2.0 , corresponding to a steady pattern, while benign lesions had an RSD of 13.1 ± 72.0 , corresponding to an ascending pattern. BWUP lesions had a mean RSD of 41.7 ± 41.4 , corresponding to an ascending pattern.

The enhancement pattern of breast lesions in CEM and its relationship to histopathologic diagnosis is shown in Table 4. The ascending pattern was found in 16 (44.4%) of 36 breast lesions, the descending enhancement pattern in 15 (41.7%), and the stable pattern in 5 (13.9%). The descending pattern was significantly

more frequent in infiltrating breast carcinomas ($n = 9$, 60.0%) ($p = 0.018$). The ascending pattern was more frequent in in situ carcinoma ($n = 2$, 100%), BWUP lesions ($n = 3$, 75%), and benign lesions ($n = 9$, 56.3%).

Figure 2 shows a 48-year-old woman with a palpable mass in the retroareolar region of the left breast. The CEM shows a focal asymmetry in the retroareolar region with heterogeneous internal enhancement. The quantitative CNR was 8.5 in the CC view and 6.7 in the MLO view. A descending enhancement pattern was detected with an RSD value of -20.9% . The histopathologic diagnosis was an infiltrating ductal lobular carcinoma.

Table 3. Quantitative RSD values of CEM enhancement in relation to histopathologic diagnosis in 36 breast lesions

Diagnosis	(n = 36)	Mean \pm SD	Minimum	Maximum
Infiltrating breast carcinoma	13	-22.8 ± 39.7	-76.5	58.0
In situ breast carcinoma	2	6.1 ± 2.0	58.6	61.5
BWUP	4	41.7 ± 41.4	-17.2	71.5
Benign breast lesions	17	13.1 ± 72.0	-98.4	223.3

CEM: contrast enhanced mammography; RSD: relative signal difference; CC: craniocaudal; MLO: medio-lateral oblique; BWUP: benign with upgrade potential; SD: standard deviation.

Table 4. Enhancement patterns on CEM and their relationship with the histopathologic diagnosis in 36 breast lesions

Diagnosis	Ascending pattern n (%)	Steady pattern n (%)	Descending pattern n (%)	p-value
Infiltrating breast carcinoma	2 (12.5)	2 (40.0)	9 (60.0)	0.018
In situ breast carcinoma	2 (12.5)	0	0	0.619
BWUP	3 (18.7)	0	1 (6.7)	0.633
Benign breast lesions	9 (56.3)	3 (60.0)	5 (33.3)	0.393
Total	16 (100)	5 (100)	15 (100)	0.101

CEM: contrast enhanced mammography; BWUP: benign with upgrade potential.

Figure 3 shows the CEM of an asymptomatic 60-year-old woman with a nonmass lesion in the upper outer quadrant and heterogeneous internal enhancement with moderately conspicuous in the upper quadrant. The quantitative CNR was 7.2 in the CC view and 3.2 in the MLO view. A descending enhancement pattern was detected with an RSD of -55.6% . The histopathologic diagnosis was an infiltrating ductal lobular carcinoma.

Figure 4 shows the CEM of an asymptomatic 46-year-old woman with focal asymmetry in the upper inner quadrant, with a heterogeneous internal enhancement pattern. The mammographic lesion is fully enhanced with high conspicuity. The quantitative CNR was 4.7 in the CC view and 6.2 in the MLO view. An ascending enhancement pattern was detected with an RSD value of 32.0% . The histopathologic diagnosis was fibroadenoma.

DISCUSSION

A significant association between the descending pattern of enhancement in CEM and invasive breast cancer was found in this study. We also observed that the ascending pattern was associated with benign

breast lesions and BWUP. The descending enhancement pattern in CEM is useful for predicting invasive breast cancer.

Few reports show that malignant breast lesions are more likely to have a descending enhancement pattern^{8,10}; thus, assessment of the enhancement pattern on CEM becomes relevant in identifying malignant breast cancer. In a study of 145 breast lesions in 131 patients, Liu et al.¹⁰ reported that 22 (51.2%) of 43 malignant lesions had a descending pattern with a mean RSD of -9.7 and 26 (25.5%) of 102 benign lesions had ascending enhancement with a mean RSD of 11.0% ($p < 0.001$). In contrast, 48 (47.1%) showed no enhancement. These results are comparable with our study in which 9 (60.0%) of 15 descending pattern lesions were infiltrating carcinomas with a mean RSD of -22.8% , while 9 (56.2%) of 16 lesions with an ascending pattern were benign, with a mean RSD of 13.1% . We believe that the differences in the mean quantitative RSD values between our results (-22.8%) and the results (-9.7%) of Liu et al.¹⁰ are because their population included infiltrating ($n = 26$) and non-infiltrating carcinomas ($n = 17$). In contrast, our population included only infiltrating carcinomas ($n = 13$) with a more pronounced descending

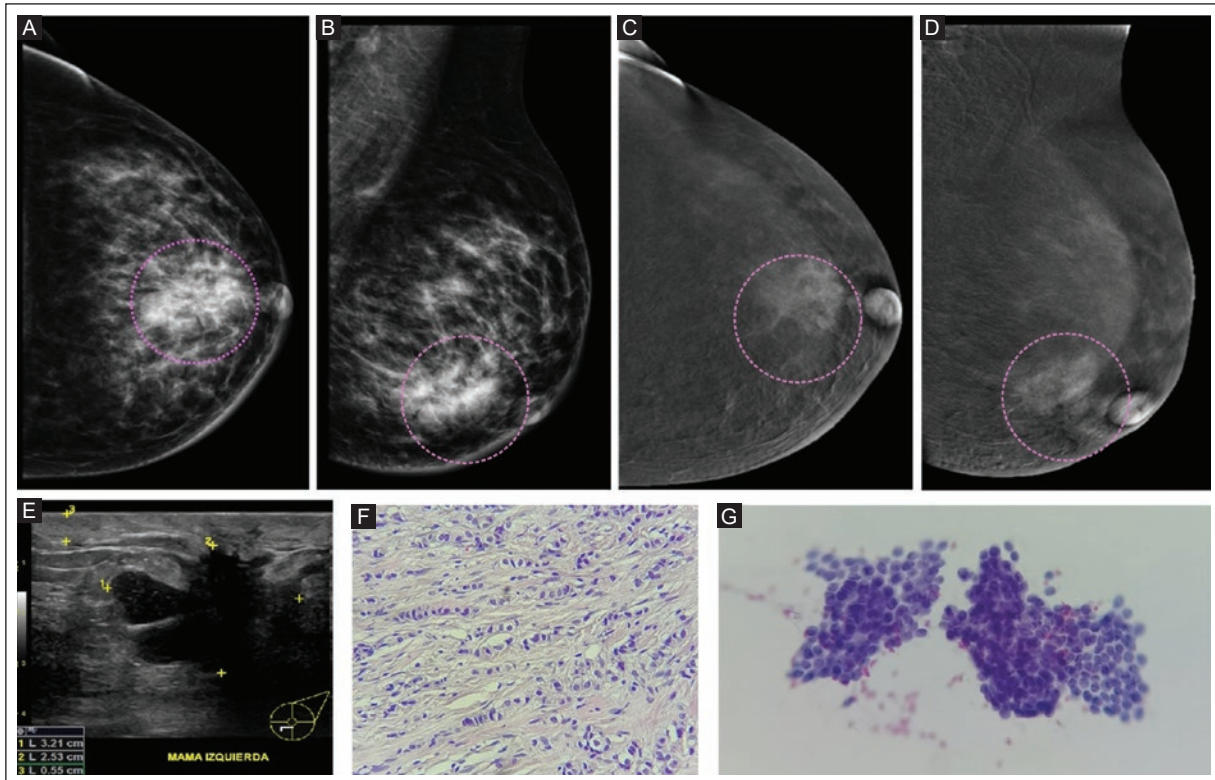


Figure 2. CEM of a 48-year-old woman with a palpable mass in the retroareolar region of the left breast. **A:** LE CC view. **B:** LE MLO view showing breast type C and with retroareolar focal asymmetry (circle). The contralateral breast has no abnormal imaging findings (not shown). **C:** RC CC view. **D:** RC MLO view with asymmetry in the retroareolar region and heterogeneous internal enhancement. The mammographic lesion is completely enhanced with moderate conspicuity. The measurements in pixels in the CC view were as follows: LS of 2091.46, BS of 1985.76, SD of 12.399 with ROI 1.1 cm², and MLO with LS of 2070.51, BS of 1985.68, SD of 12.58 with ROI 1.1 cm². The quantitative CNR was 8.5 in the CC view and 6.7 in the MLO view. A descending enhancement pattern was detected with an RSD value of -20.9%. **E:** Breast US in grayscale, in an anti-radial plane, showing an irregular, parallel mass with an indistinct margin, hypoechoic with posterior acoustic shadowing causing skin retraction and thickening (5 mm). **F:** CNB H&E 40x: infiltrating epithelial malignant neoplasm composed of medium-sized cells arranged in "Indian file" and some in ducts. **G:** CNB H&E 40x: smear with malignant epithelial cells and lymphocytes. The histopathologic diagnosis was an infiltrating ductal lobular carcinoma.

BS: background signal; CC: craniocaudal view; CEM: contrast enhanced mammography; CNB: core needle biopsy; CNR: contrast-to-noise ratio; MLO: medio-lateral oblique; LE: low energy; LS: lesion signal; RC: recombined; ROI: H&E hematoxylin and eosin; RSD: relative signal difference; SD: standard deviation; US: ultrasound.

pattern. In CEM, malignant lesions tend to show enhancement washout (descending pattern), and most benign lesions show non-enhancing or persistent enhancement (ascending pattern). In terms of enhancement patterns, a large proportion of malignant lesions show descending patterns. In contrast, most benign lesions do not show enhancing or ascending patterns, which is a finding that may help distinguish benign and malignant breast lesions.

CEM enhancement can be found in malignant, BWUP, and benign breast lesions¹². Rudnicki et al.⁹ examined 120 (61.5%) infiltrating carcinomas, 16 (8.2%) non-infiltrating carcinomas, and 59 (30.3%) benign lesions in 167 patients with 195 breast lesions. Only 13

(6.7%) did not show enhancement (benign). They found a significant difference in %RS between infiltrating and non-infiltrating carcinomas and between infiltrating and benign lesions, with no significant difference between benign and non-infiltrating breast carcinomas. Enhancement was similar in the CC and MLO projections. The mean %RS values correlated with the type of enhancement lesion, with infiltrating carcinomas having the highest values and benign lesions having the lowest values. Liu et al.¹⁰ demonstrated that enhancement quantified by CNR was significantly higher in malignant lesions than in benign lesions ($p < 0.001$). In contrast, the difference between infiltrating and non-infiltrating malignant lesions was insignificant.

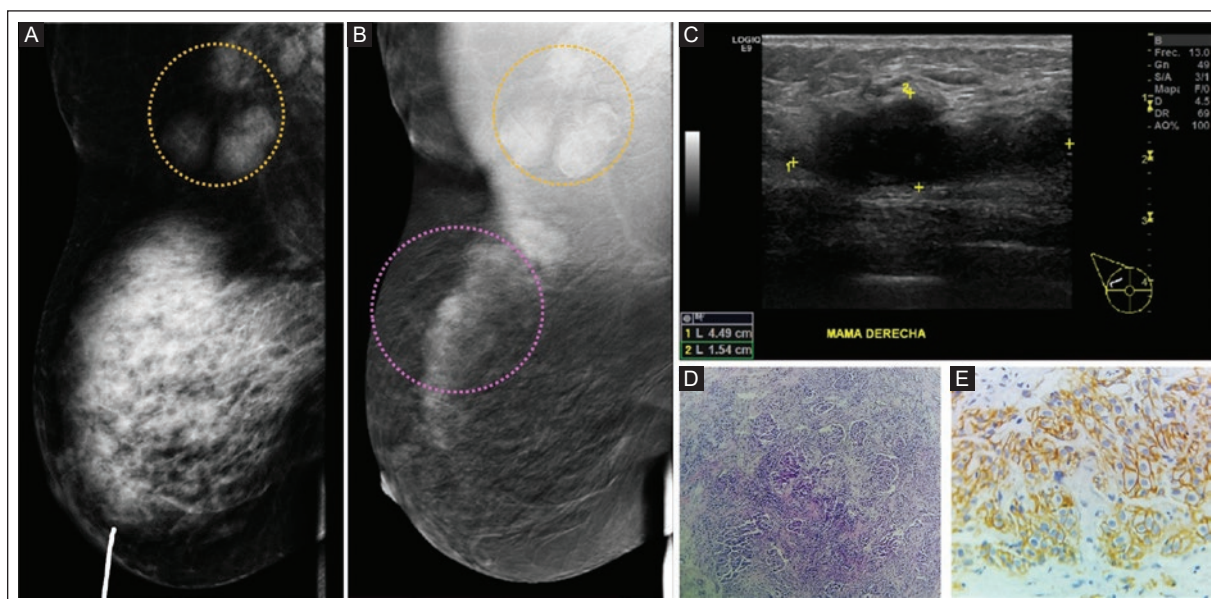


Figure 3. CEM in an asymptomatic 60-year-old woman. **A:** LE MLO view showing breast type D and lymph nodes with loss of morphology and fatty hilum (yellow circle). **B:** RC MLO view with no mass lesion in the upper outer quadrant and heterogeneous internal enhancement pattern with moderate conspicuity in the upper quadrant. Lymph nodes with enhancement (yellow circle). The measurements in pixels in the CC view were as follows: LS of 2081.31, BS of 2016.92, SD of 8.89 with ROI 0.64 cm² and MLO with LS of 2113.46, BS of 2029.03, SD of 26.27 with ROI 0.64 cm². The quantitative CNR was 7.2 in the CC view and 3.2 in the MLO view. A descending enhancement pattern was detected with an RSD of -55.6%. **C:** Breast US in grayscale, antiradial axis, showing an irregular, parallel, spiculated, hypoechoic mass with posterior acoustic enhancement. **D:** CNB H&E 40×: infiltrating epithelial malignant neoplasm composed of medium-sized cells arranged in “Indian file” and some in ducts. **E:** CNB H&E 20×: infiltrating epithelial malignant neoplasm composed of medium-sized cells. Immunohistochemistry HER 2/neu positive with membrane staining in more than 10% of the cells. The histopathologic diagnosis was an infiltrating ductal lobular carcinoma.

BS: background signal; CC: craniocaudal view; CEM: contrast enhanced mammography; CNB: core needle biopsy; CNR: contrast-to-noise ratio; H&E: hematoxylin and eosin; LE: low energy; RC: recombined; LS: lesion signal; MLO: mediolateral oblique; RSD: relative signal difference; SD: standard deviation; US: ultrasound.

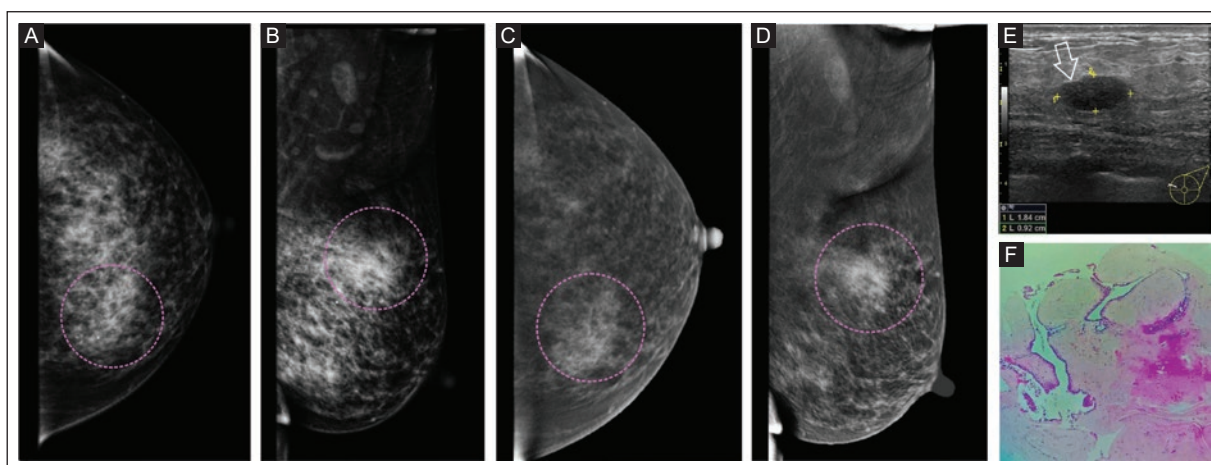


Figure 4. CEM in an asymptomatic 46-year-old woman. **A:** LE CC view. **B:** LE MLO view with focal asymmetry in the upper inner quadrant (circle) with a heterogeneous internal enhancement pattern. The contralateral breast has no abnormal imaging findings (not shown). **C:** RC CC view. **D:** RC MLO view with focal asymmetry in the upper inner quadrant, with heterogeneous internal enhancement. The mammographic lesion is completely enhanced, with high conspicuity. The measurements in pixels in the CC view were as follows: LS of 2067.41, BS of 1686.87, SD of 17.02 with ROI 0.78 cm² and MLO view with LS of 2118.26, BS of 2014.05, SD of 16.68 with ROI 0.78 cm². The quantitative CNR was 4.7 in the CC view and 6.2 in the MLO view. An ascending enhancement pattern was detected with an RSD value of 32.0%. **E:** breast US in grayscale, antiradial axis, showing an oval, parallel, circumscribed, hypoechoic mass (hollow arrow). **F:** CNB H&E 40×: biphasic neoplasm composed of ductal proliferation in a largely fibrous stroma. The histopathologic diagnosis was fibroadenoma.

BS: background signal; CC: craniocaudal view; CEM: contrast enhanced mammography; CNB: core needle biopsy; CNR: contrast-to-noise ratio; H&E: hematoxylin and eosin; LE: low-energy; LS: lesion signal; MLO: mediolateral oblique; RC: recombined; RSD: relative signal difference; SD: standard deviation; US: ultrasound.

The enhancement of infiltrating carcinomas ($n = 26$) showed a CNR_CC of 7.6 and a CNR_MLO of 6.4. Our study found comparable results in infiltrating carcinomas ($n = 13$) with a CNR_CC of 6.5, which was higher than in benign lesions with a CNR_CC of 4.9. In contrast, the CNR_MLO showed comparable values between malignant and benign lesions (4.5 and 5.0, respectively). Quantitative CNR and %RS enhancement analysis in CEM provides useful information for predicting breast malignancy⁸⁻¹⁰.

The strengths of the study were the evaluation of images in two projections, which allowed the acquisition of data in both early and late stages and facilitated understanding of the enhancement pattern in CEM in malignant, BWUP, and benign breast lesions. In addition, all cases were confirmed by histologic analysis. Limitations were the small sample size, the retrospective analysis, and the fact that this is a single-center study. We excluded lesions that did not show enhancement, which precludes a specific comparison with the results of other studies that included these lesions.

CONCLUSION

The descending pattern of enhancement in CEM showed a significant association with infiltrating breast cancer, whereas the ascending pattern was more common in benign breast lesions and BWUP. Although both benign and malignant breast lesions may show some enhancement, the pattern proves to be a feature that allows adequate characterization of malignant lesions. Quantitative analysis of patterns of CEM enhancement features is feasible for clinical practice¹⁰. The need for a larger number of multicenter patient studies is evident to determine the role of quantitative analysis of CEM enhancement in accurately distinguishing malignant and benign breast lesions.

Acknowledgments

The authors thank Professor Ana M. Contreras-Navarro for her guidance in preparing and writing this scientific paper.

Funding

This research received no external funding.

Conflicts of interest

The authors declare that they have no conflicts of interest.

Ethical disclosures

Protection of Individuals. This study complied with the Declaration of Helsinki (1964) and its amendments.

Confidentiality of Data. The authors declare that they followed their center's protocol for sharing patient data.

Right to privacy and informed consent. Informed consent was not required for this observational study of information collected during routine clinical care.

Use of artificial intelligence. The authors did not use generative artificial intelligence to prepare this manuscript and/or create tables, figures, or figure legends.

REFERENCES

1. Zamora K, Allen E, Hermecz B. Contrast mammography in clinical practice: Current uses and potential diagnostic dilemmas. *Clin Imaging*. 2021;71(1):126-135. doi:10.1016/j.clinimag.2020.11.002.
2. Sogani J, Mango V, Keating D, Sung J, Jochelson M. Contrast-enhanced mammography: past, present and future. *Clin Imaging*. 2021;69: 269-279. doi:10.1016/j.clinimag.2020.09.003.
3. Jochelson MS, Lobbes MBI. Contrast-enhanced Mammography: State of the Art. *Radiology*. 2021;299(1):36-48. doi: 10.1148/radiol.2021201948.
4. Sensakovi W, Carnahan M, Czaplicki C, Fahrenheit S, Panda A, Zhou Y, et al. Contrast-enhanced Mammography: How Does It Work? *Radiographics*. 2021;41(3):829-839. doi.org/10.1148/rg.2021200167.
5. Cho SH, Park SH. Mimickers of breast malignancy on breast sonography. *J Ultrasound Med*. 2013;32(11):2029-2036. doi: 10.7863/ultra.32.11.2029.
6. Lee C, Phillips J, Sung J, Lewin J, Newell M. Breast Imaging Reporting and Data System: ACR BI-RADS breast imaging atlas. Contrast Enhanced Mammography (CEM) (A supplement to ACR BI-RADS® Mammography 2013). 5th Edition. Reston: American College of Radiology, 2022.
7. Perez-Montemayor DF, Rios-Rodriguez TA, Garcia-Alvarez KG. Clinical application of the first version of the BI-RADS lexicon for contrast enhanced mammography: a pictorial essay. *J Mex Fed Radiol Imaging*. 2023;2(1):61-71. doi: 10.24875/jmexfri.m23000042.
8. Deng CY, Juan YH, Cheung YC, Lin YC, Lo YF, Lin G, et al. Quantitative analysis of enhanced malignant and benign lesions on contrast-enhanced spectral mammography. *Sci Rep*. 2018 ;9(10):9807. doi:10.1259/bjr.20170605.
9. Rudnicki W, Heinze S, Niemiec J, Kojs Z, Sas-Korczynska B, Hendrick E, et al. Correlation between quantitative assessment between contrast enhancement in contrast-enhanced spectral mammography (CESM) and histopathology-preliminary results. *Eur Radiol*. 2019;29(11):6220-6226. doi:10.1007/s00330-019-06232-6.
10. Liu Y, Zhao S, Huang J, Zhang X, Qin Y, Zhong H, et al. Quantitative Analysis of Enhancement Intensity and Patterns on Contrast-enhanced Spectral Mammography. *Sci Rep*. 2020;10(1):9807. doi: 10.1038/s41598-020-66501-z.
11. Mendelson EB, Böhm-Vélez M, Berg WA, Whitman GJ, Feldman MI, Madjar H. ACR BI-RADS® Ultrasound. In: ACR BI-RADS® Atlas, Breast Imaging Reporting and Data System. Reston, VA, American College of Radiology; 2013.
12. Corona-Gonzalez CB, Gonzalez-Ulloa BE, Perez-Montemayor DF, Juarez-Lopez GE. High diagnostic performance of architectural distortion enhancement on CEM for predicting malignant breast lesions. *J Mex Fed Radiol Imaging*. 2023;2(3):172-183. doi: 10.24875/JMEXFRI.M23000053.

US duplex findings in chronic venous insufficiency of the lower limbs in 500 Mexican patients

Mauricio Figueroa-Sanchez^{1,2,3} , M. Fernanda Lopez-Mendoza^{1,2}, Simmons D. Gough^{1,2}, and J.M. Ignacio Lopez-Mendez^{2,4}

¹Radiology and Imaging Department, Antiguo Hospital Civil de Guadalajara “Fray Antonio Alcalde”; ²University Center of Health Sciences, Universidad de Guadalajara; ³Laboratorio Vascular S.C.; ⁴Department of Radiology and Imaging, Hospital de Especialidades Centro Medico Nacional de Occidente, Instituto Mexicano del Seguro Social. Guadalajara, Jalisco, Mexico

ABSTRACT

Introduction: There are few reports of ultrasound (US) duplex findings in patients with chronic venous insufficiency (CVI). The aims of this study were (1) to describe CVI ultrasound findings of the lower limbs in Mexican patients according to sex and age and (2) to propose a grade classification of CVI based on reflux velocity. **Materials and Methods:** Adult patients with clinically suspected lower limb CVI were studied in this cross-sectional study. The complete protocol was performed using the following US modalities: grayscale, duplex Doppler, color Doppler, power Doppler, and B-flow examination. The parameters examined were diameter, compressibility, permeability, direction, flow, and reflux velocity in the veins. The grade classification was based on the reflux velocity as grade 1, from 1 to ≤ 10 cm/s; grade 2, from 11 cm/s to 20 cm/s; and grade 3, > 20 cm/s. **Results:** A total of 500 patients were included. Based on the US duplex findings, 312 (62.4%) women and 131 (26.2%) men were diagnosed with CVI. Insufficiency of the perforating venous system and the age group of 40–49 years were most common in both genders, followed by insufficiency of the superficial venous system. The most frequent association was insufficiency of the superficial venous system with insufficiency of the perforating venous system. CVI grade 3 was more common in the superficial venous system, while similar frequencies were found for the three-reflux grade in deep venous insufficiency. **Conclusion:** This study shows a complete description of US duplex findings of lower limb CVI from the radiologist's perspective; for the first time, a grade classification based on reflux velocity is proposed.

Keywords: Chronic venous insufficiency. Ultrasound duplex. CVI types.

INTRODUCTION

Chronic venous insufficiency (CVI) of the lower limbs encompasses a broad spectrum of morphological and functional abnormalities characterized by venous hypertension caused by inadequate venous return due to valve damage^{1,2}. It is one of the most common health problems worldwide, affecting approximately 90% of the population in industrialized countries³ with a high

economic cost⁴. CVI risk factors include age, obesity, female gender, genetics, sedentary lifestyle, and occupations that require prolonged standing⁵. The clinical manifestations of CVI range from telangiectasis to venous leg ulceration⁶.

Ultrasound (US) duplex is the imaging modality of choice for diagnosing CVI. It directly demonstrates the patency and competence of venous valves, as well as flow direction and velocity^{4,7,8}. Several protocols have

*Corresponding author:

Mauricio Figueroa-Sanchez
E-mail: figueroa_sanchez@hotmail.com

Received for publication: 23-11-2023

Accepted for publication: 10-02-2024

DOI: 10.24875/JMeXFRI.M24000069

Available online: 22-03-2024

J Mex Fed Radiol Imaging. 2024;3(1):45-55

www.JMeXFRI.com

2696-8444 / © 2024 Federación Mexicana de Radiología e Imagen, A.C. Published by Permanyer. This is an open access article under the CC BY-NC-ND (<https://creativecommons.org/licenses/by-nc-nd/4.0/>).

been published that describe CVI findings with US duplex^{9,10,11}. However, there is no standardized examination. In the author's experience, CVI assessment and diagnostic imaging are the principal indications for evaluation in vascular laboratories, with an 8:1 ratio of venous to arterial examinations. However, there are few publications on US duplex findings in patients with CVI. In particular, there are no publications on the Mexican population. The aims of this study were (1) to describe ultrasonographic CVI findings of the lower limbs in Mexican patients by US duplex according to sex and age and (2) to propose a grade classification based on reflux velocity.

MATERIALS AND METHODS

This cross-sectional study was conducted between March 2004 and July 2023 at the Vascular Laboratory SC in Guadalajara, Jalisco, Mexico. Patients of both sexes over 18 years of age referred by angiologists with a clinical suspicion of CVI in the lower limbs were included. The pediatric population and patients with deep vein thrombosis due to neoplasms were excluded. Data were collected during routine medical care; therefore, informed consent was not required for data analysis and publication. The protocol was approved by the institutional research ethics and research committees.

Description of variables

The vein parameters assessed were diameter (mm), compressibility, permeability, direction, flow, and reflux velocity (cm/s).

Definitions

CVI: it is a condition that affects the veins of the lower limbs characterized by chronic venous hypertension^{1,12}.

Recanalization: color Doppler US shows a variable percent flow (10–90%) on longitudinal and transverse views. Pulsed US duplex shows variable flow velocity (author MFS suggested definition).

Venous reflux: it is a retrograde flow associated with dilation during the Valsalva maneuver. A spectral inversion > 1-s duration and a change from blue to red on the color Doppler US are demonstrated^{13–15}.

Insufficiency of the perforating venous system: it is the reversed flow from the deep venous system to the superficial venous system in a perforating vein with a diameter > 3 mm and/or duration > 1 s (author MFS suggested definition).

Insufficiency of the reticular venous system: The author (MFS) proposes the term reticular venous system to refer to the reticular veins, located in the epifascial compartment and allowing antegrade and retrograde flow depending on their position in relation to gravity¹⁶. The US duplex examination shows dilated reticular veins (diameter > 3 mm) with retrograde flow.

Post-thrombotic syndrome: US duplex shows reflux in the deep venous system with associated echogenic endothelial thickening and echogenic thickening (> 1 mm) of venous valves, the presence of septa, echogenic bands, and/or endoluminal echogenic material always associated with venous reflux (author MFS suggested definition).

Venous permeability: it is the capacity of the vein to allow a free flow within it. Color Doppler US and US duplex show endoluminal flow and direction (antegrade or retrograde).

Grades of reflux severity: a classification based on reflux velocity due to valve insufficiency was arbitrarily determined by the author (MFS) based on the fact that chronic venous hypertension is the cornerstone of the pathophysiology of superficial and deep CVI. The proposed classification is grade 1, from 1 to ≤ 10 cm/s; grade 2, from 11 cm/s to 20 cm/s; and grade 3, > 20 cm/s. The measurement of reflux velocity was performed with the correction of the insonation angle. US devices allow correction in post-processing.

Image acquisition protocol

All studies were performed by a radiologist (MFS) with 30 years of experience in vascular US. The equipment used was an Aloka SSD4000S with 10- and 13-MHz linear transducers and 2–6-MHz convex transducers (Aloka Co., Tokyo, Japan) and a LOGIG E9 (GE Co., Wisconsin, USA) with 10–16-MHz and 3–6-MHz convex transducers.

The complete US protocol of the venous system of the lower limbs was performed as previously described by Figueroa et al.¹⁰ using the duplex US modalities: gray-scale, duplex Doppler, color Doppler, power Doppler, and, more recently, B-flow examination. It began at the ostium of the vena cava, examined its entire course, and continued in the primitive and external iliac veins. In the deep venous system, the common femoral vein, the femoral vein, the deep femoral vein, the popliteal vein, the anterior tibial vein, the posterior tibial vein, the peroneal vein, and the gastrocnemius vein were examined. In the superficial venous system, the saphenous–femoral junction and the greater and lesser saphenous vein

Table 1. Frequency of lower limb CVI types according to US findings in Mexican patients with a suspected clinical diagnosis

Description	Total ^{a,b} (n = 500)	Women (n = 347)	Men (n = 153)
Perforating venous system insufficiency, n (%)	406 (81.2)	288 (82.9)	118 (77.1)
Superficial venous system insufficiency, n (%)	322 (64.4)	233 (67.1)	89 (58.1)
Deep venous system insufficiency, n (%)	98 (19.6)	58 (16.7)	40 (26.1)
Reticular venous system insufficiency, n (%)	75 (15.0)	57 (16.4)	18 (11.7)
Other findings without CVI ^c , n (%)	57 (11.4)	35 (10.0)	22 (14.4)

^aReferred by angiologists with a clinical suspicion of CVI. ^bTwo or more CVI types may occur in the same patient. ^cOther findings such as edema, panniculitis, tears, popliteal cysts, and cardiac failure. CVI: chronic venous insufficiency; US: ultrasound.

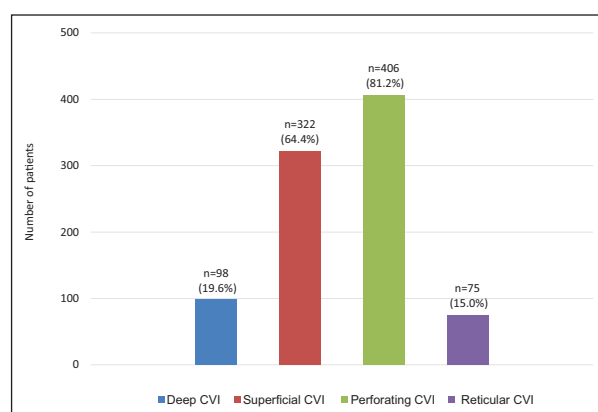


Figure 1. Frequency of lower limb CVI types according to US findings in 500 Mexican patients with a suspected clinical diagnosis referred by angiologists. Two or more CVI types may occur in the same patient. Of all patients examined, 57 (11.4%) patients without CVI were found to have other findings such as edema, panniculitis, tears, popliteal cysts, and cardiac failure.

CVI: chronic venous insufficiency; US: ultrasound.

were examined in their entire course, in addition to the perforating venous system (thigh, knee, and leg) and the reticular venous system.

Statistical analysis

Data are presented as frequencies and percentages using Microsoft Excel™ version 18.0 (Microsoft Corp., Seattle, WA, USA).

RESULTS

A total of 500 patients with clinically suspected CVI in the lower limbs were included; there were 347 (69.4%) women and 153 (30.6%) men with 183 bilateral and 317 unilateral examinations. A total of 683 legs

were examined. CVI was diagnosed by US duplex in 443 (88.6%) of 500 patients: 312 (62.4%) women and 131 (26.2%) men.

Types of CVI according to US duplex

The frequency of all CVI types varied according to the affected venous system. In 406 (81.2%) of 500 patients, insufficiency of the perforating venous system was the most common finding, with 288 (82.9%) of 347 women and 118 (77.1%) of 153 men (Table 1) (Figure 1). Insufficiency of the superficial venous system was the second most common finding, occurring in 322 (64.4%) of 500 patients, 233 (67.1%) of 347 women, and 89 (58.1%) of 153 men. Deep venous system insufficiency was the third, with 98 (19.6%) patients, 58 (16.7%) of 347 women, and 40 (26.1%) of 153 men, while 57 (16.4%) of 347 women and 18 (11.7%) of 153 men have insufficiency of the reticular venous system. Figure 2 shows an example of the insufficiency of the perforating venous system. Of all patients examined, 57 (11.4%) patients without CVI were found to have other findings such as edema, panniculitis, tears, popliteal cysts, and cardiac failure (Figure 3).

CVI types in relation to sex and age

Figure 4A shows the frequency of patients with different types of venous insufficiency by age in women. Of the 347 women with CVI, the highest frequency of all types of CVI was found in the 40–49 age group: 23 (6.6%) women had deep system insufficiency, 85 (24.5%) women had superficial system insufficiency, 104 (30.0%) had perforating system insufficiency, and 14 (4.0%) had reticular system insufficiency. Figure 4B shows the frequency of patients with the CVI types by

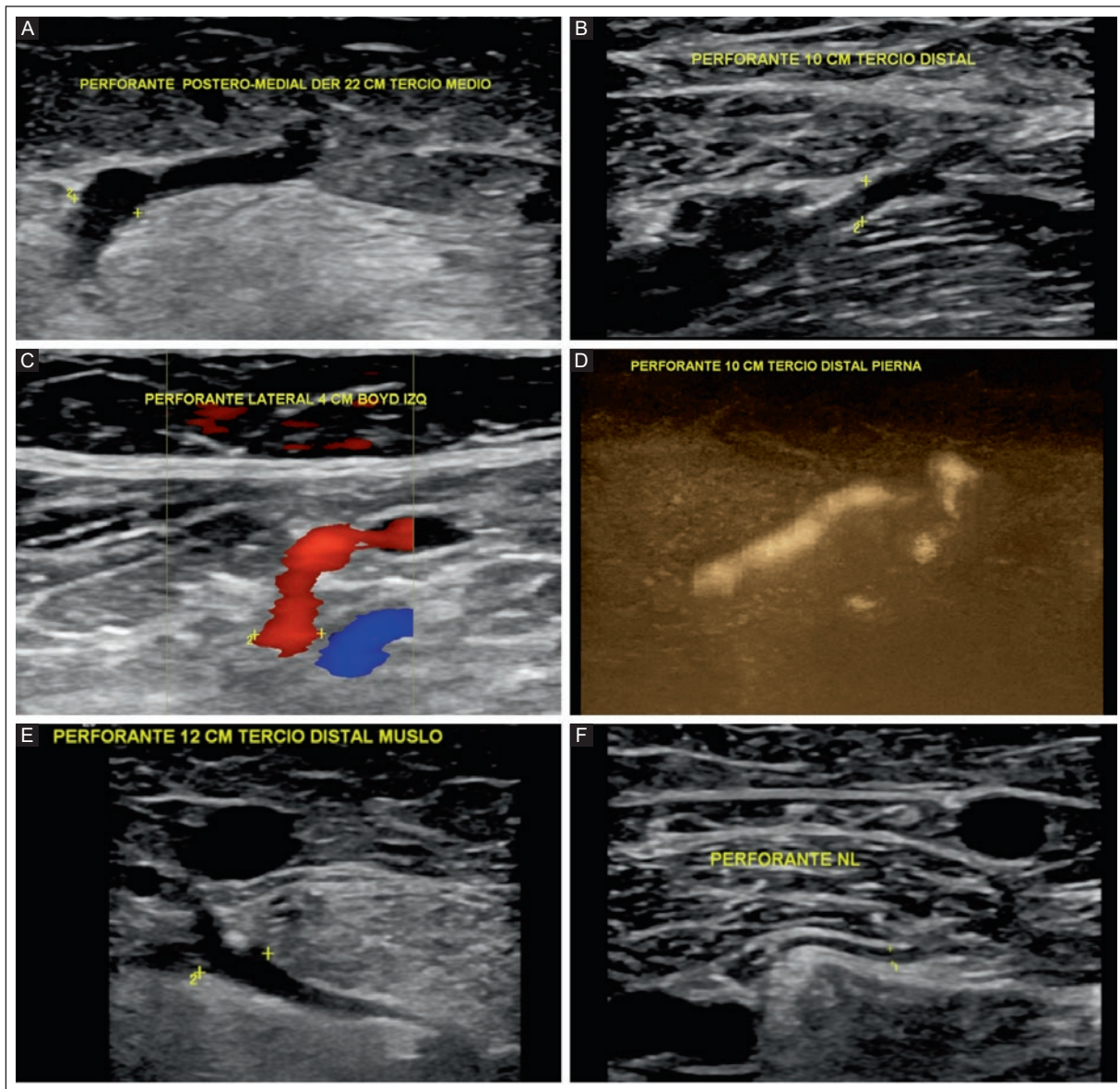


Figure 2. A 57-year-old woman with a diagnosis of CVI. **A:** grayscale US duplex, transverse view of the incompetent right posteromedial perforating vein with a diameter of 5.2 mm. **B:** grayscale US duplex, transverse view of the incompetent perforating vein in the distal third of the thigh with a diameter of 3.7 mm. **C:** color Doppler, transverse view with inversion from blue to red during the Valsalva maneuver in relation to the incompetent Boyd's perforating vein with a diameter of 5.1 mm. **D:** B-flow Doppler, transverse view of the incompetent perforating vein in the distal third of the leg. **E:** grayscale US duplex, transverse view of the incompetent perforating vein in the distal third of the thigh with a diameter of 4.5 mm. **F:** grayscale US duplex, transverse view of a normal perforating vein with a diameter of 1.3 mm. (Vein diameter measurements are not shown.)

CVI: chronic venous insufficiency; US: ultrasound.

age in men, showing similar behavior to women, with the highest frequency in the 40-49 age group: of the 153 men with CVI, 15 (9.8%) men had deep system insufficiency, 31 (20.3%) men had superficial system insufficiency, 39 (25.5%) men had perforating system insufficiency, and 4 (2.6%) men had reticular system insufficiency. Figure 5 shows examples of deep, superficial, and perforating system insufficiency.

Association between the different types of CVI

Table 2 shows the frequency of the different combinations of CVI types. The most common combination was superficial + perforating venous system insufficiency with 159 (45.8%) of 347 women and 52 (33.9%) of 153 men, followed by patients with deep venous + superficial +

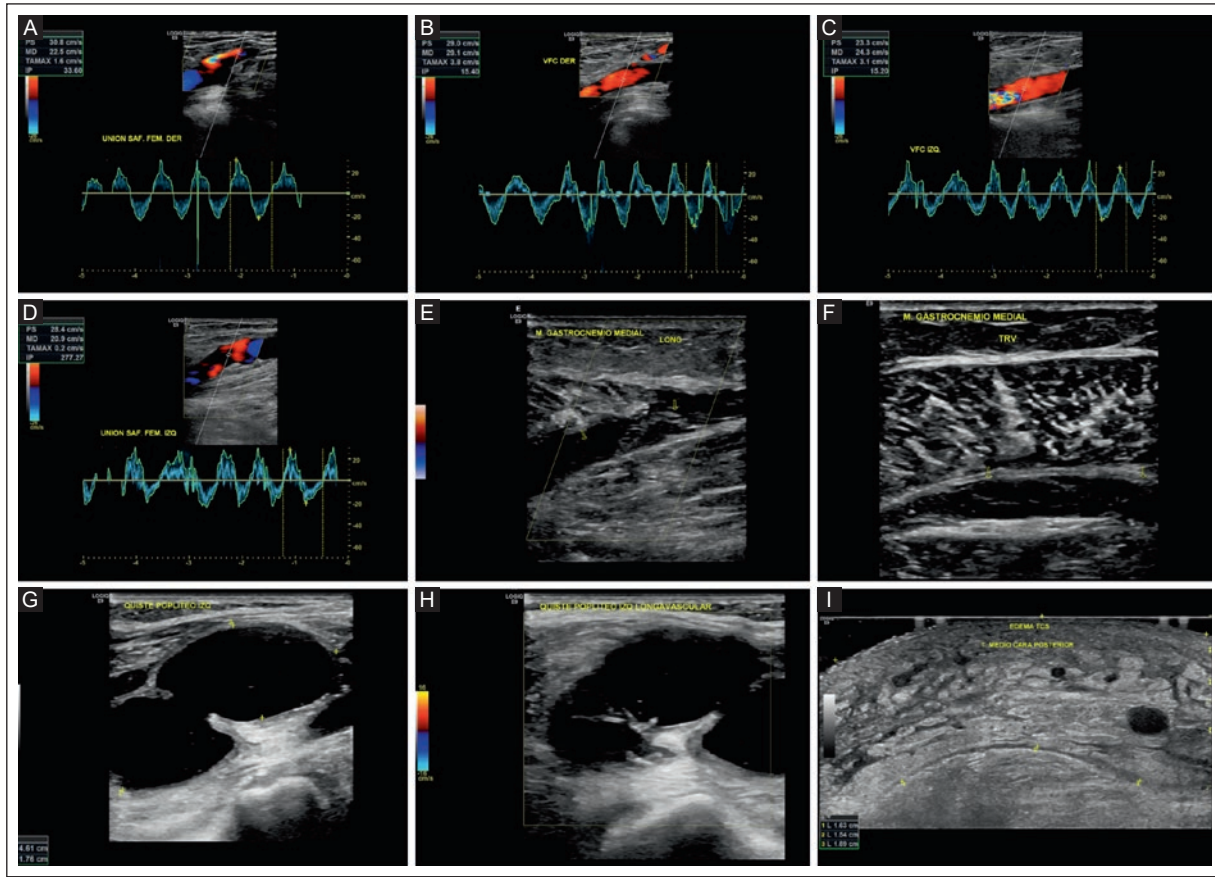


Figure 3. A 60-year-old woman with venous congestive heart failure. Duplex Doppler US of the **A:** right saphenous-femoral junction, **B:** right common femoral vein, **C:** left common femoral vein, and **D:** left saphenous-femoral junction showing alternating continuous antegrade and retrograde spectrum associated with venous congestive heart failure. A 54-year-old male with a clinical diagnosis of CVI. **E:** grayscale US duplex, longitudinal view, showing a tear of the medial gastrocnemius. **F:** grayscale US duplex, transverse view, showing a tear of the medial gastrocnemius. A 48-year-old female with a clinical diagnosis of CVI. **G:** grayscale US duplex, transverse view, showing popliteal cyst with a transverse diameter of 4.61 cm and an anteroposterior diameter of 1.76 cm. **H:** grayscale US duplex, longitudinal view, showing a popliteal cyst. **I:** grayscale US duplex, transverse view, posterior aspect of the thigh in the middle third, showing edema of the subcutaneous cellular tissue.

CVI: chronic venous insufficiency; US: ultrasound.

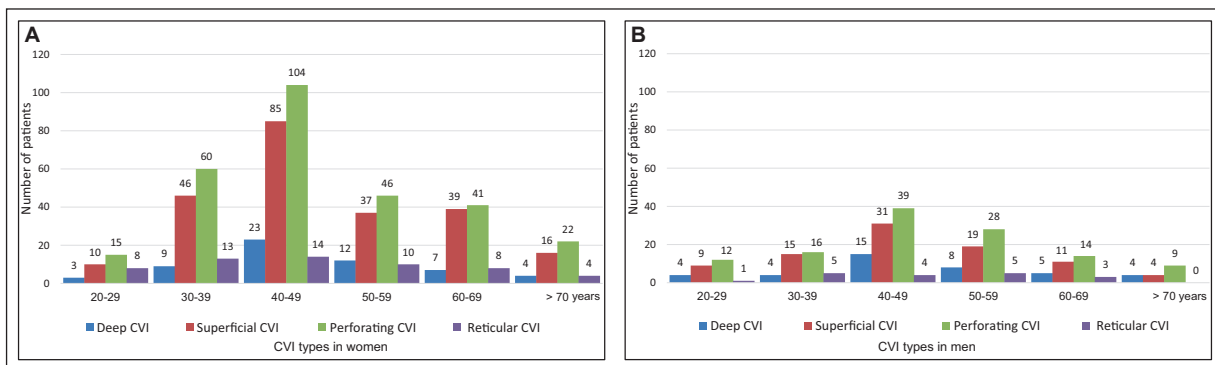


Figure 4. Distribution of the different types of CVI by sex and age. **A:** women have a higher frequency in the 40-49 years age group, followed by the 30-39 years age group. **B:** men have a higher frequency in the 40-49 years age group, followed by the 50-59 years age group.

CVI: chronic venous insufficiency.

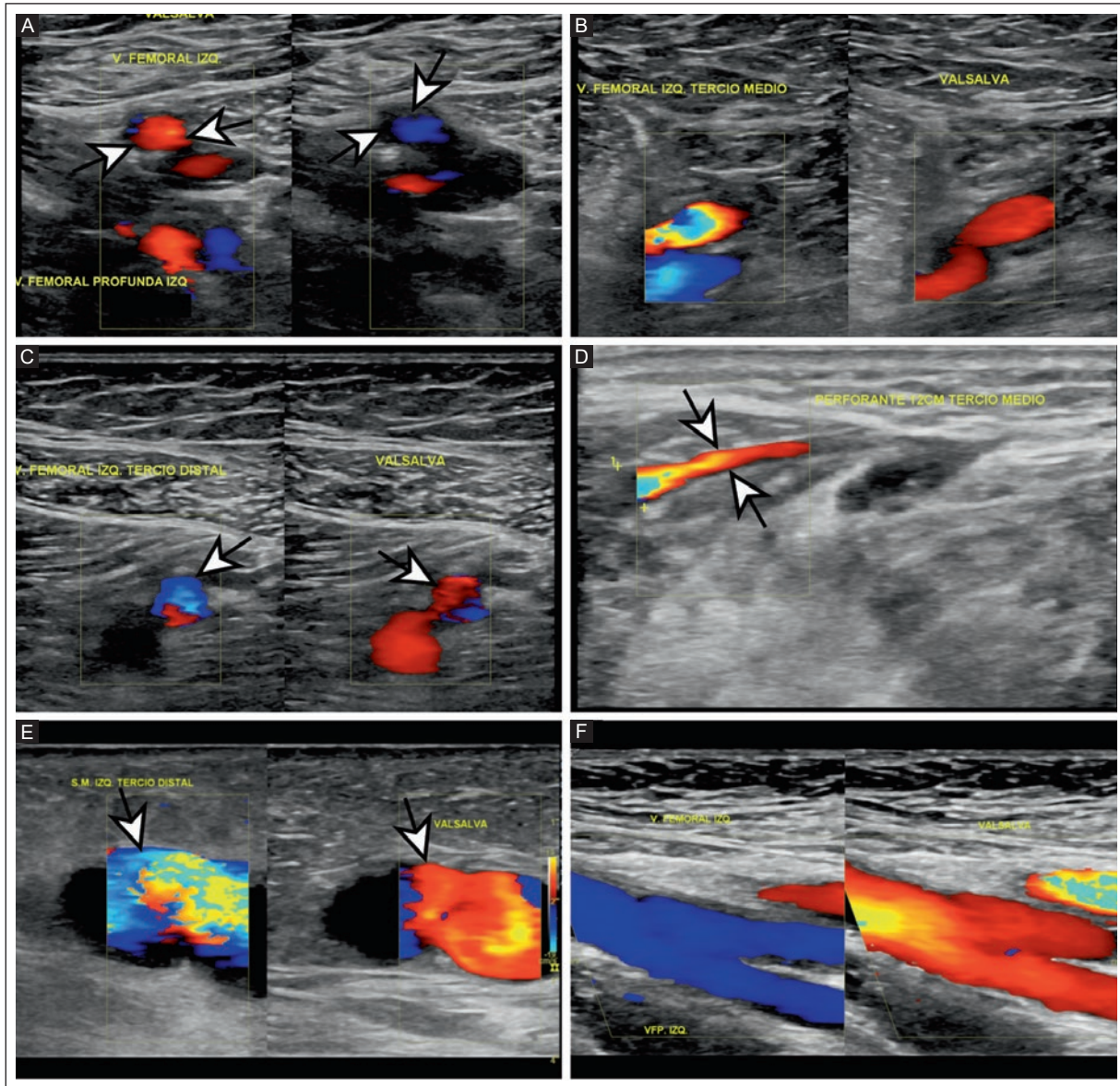


Figure 5. A 50-year-old man with a diagnosis of CVI. **A:** color Doppler US, transverse view of the femoral vein and the left deep femoral vein with inversion from blue to red during the Valsalva maneuver in relation to the reflux (arrows), with concentric endothelial thickening as a result of chronic thrombosis. **B:** color Doppler US, transverse view of the middle third of the left femoral vein with inversion from blue to red with the Valsalva maneuver in relation to reflux. **C:** color Doppler US, transverse view of the distal third of the left femoral vein with inversion from blue to red with the Valsalva maneuver in relation to the reflux (arrows). **D:** color Doppler US, transverse view showing reflux in a 4 mm diameter perforating vein 12 cm from the lower edge of the medial malleolus in the leg (arrows). **E:** color Doppler US, transverse view of the distal third of the left great saphenous vein with inversion from blue to red on the Valsalva maneuver, in relation to the reflux (arrows). **F:** color Doppler US, longitudinal view of the femoral vein and the left deep femoral vein, showing the inversion from blue to red with the Valsalva maneuver in relation to the reflux.

CVI: chronic venous insufficiency; US: ultrasound.

perforating venous system insufficiency with 28 (8.0%) of 347 women and 23 (15.0%) of 153 men. Figure 6 shows an example of the association between superficial and deep venous insufficiency. Only one type of CVI was found in 84 (16.8%) patients. The most common was insufficiency of the perforating venous system, followed by insufficiency of the superficial, reticular, and deep venous systems.

Three-grade classification of CVI according to reflux velocity using US duplex

Table 3 shows the grade classification of the superficial and deep venous system in relation to sex.

A higher frequency of grade 3 reflux velocity was found in the superficial venous system in 200 (62.1%)

Table 2. CVI types of the lower limbs with and without combinations according to US findings in Mexican patients with a suspected clinical diagnosis

Description	Total ^a (n = 500)	Women (n = 347)	Men (n = 153)
CVI types with combinations			
Superficial + perforating venous system insufficiency, n (%)	211 (42.2)	159 (45.8)	52 (33.9)
Deep + superficial + perforating venous system insufficiency, n (%)	51 (10.2)	28 (8.0)	23 (15.0)
Superficial + reticular + perforating venous system insufficiency, n (%)	33 (6.6)	27 (7.8)	6 (3.9)
Deep + perforating venous system insufficiency, n (%)	25 (5.0)	15 (4.3)	10 (6.5)
Reticular + perforating venous system insufficiency, n (%)	23 (4.6)	16 (4.6)	7 (4.6)
Deep + reticular + perforating venous system insufficiency, n (%)	6 (1.2)	4 (1.1)	2 (1.3)
Superficial + reticular venous system insufficiency, n (%)	4 (0.8)	3 (0.9)	1 (0.6)
Deep + superficial venous system insufficiency, n (%)	4 (0.8)	3 (0.9)	1 (0.6)
Deep + superficial + reticular + perforating venous systems insufficiency, n (%)	2 (0.4)	2 (0.5)	0
CVI types without combinations			
Deep venous system insufficiency, n (%)	7 (1.4)	4 (1.2)	3 (2.0)
Superficial venous system insufficiency, n (%)	17 (3.4)	12 (3.6)	5 (3.3)
Perforating venous system insufficiency, n (%)	52 (10.4)	34 (9.8)	18 (11.9)
Reticular venous system insufficiency, n (%)	8 (1.6)	5 (1.4)	3 (2.0)
Other findings without CVIb, n (%)	57 (11.4)	35 (10.1)	22 (14.4)

^aReferred by angiologists with a clinical suspicion of CVI. ^bOther findings such as edema, panniculitis, tears, popliteal cysts, and cardiac failure. CVI: chronic venous insufficiency; US: ultrasound.

of 322 patients, followed by grade 2 in 74 (23.0%) patients and grade 1 in 48 (14.9%) patients. The proportions of reflux velocity grades in superficial venous insufficiency were comparable in women and men.

In deep venous insufficiency, comparable frequencies were found for the three grades of reflux velocity, with 21 (36.2%) of 58 women having grade 1, 20 (34.5%) women having grade 2, and 17 (29.3%) women having grade 3. On the other hand, grade 1 was found in 13 (32.5%) of 40 men, grade 2 in 10 (25.0%) men, and grade 3 in 17 (42.5%) men. Figure 7 shows examples of the three grades of insufficiency according to the reflux velocity based on the US duplex findings.

DISCUSSION

This study is the first in Mexican patients to provide a complete description of US duplex findings of CVI of the lower limbs. The age of the highest CVI frequency was 40-49 years in both sexes, and the most common type was perforating venous system insufficiency and the association of superficial and perforating venous

system insufficiency. A classification into three grades of severity is proposed based on reflux velocity by US duplex, reflecting the degree of chronic venous hypertension. We hypothesize that reflux severity may be directly associated with the development of venous ulcers.

CVI peaks in the fifth decade of life, the productive age associated with increased related symptoms¹⁷. In relation to gender, in a meta-analysis of 32 English-language articles from six continents, Salim et al.¹⁸ found that women were more likely to suffer from CVI (OR 2.26, 95% CI 2.16-2.36, $p < 0.001$). This finding has been linked to biological and hormonal factors¹⁹. Similar to other reports, in our study of the Mexican population, the frequency was 2:1 in women and men, and the age with the highest frequency was between 40 and 49 years in both sexes. However, as women tend to visit health services more frequently than men, this finding may be related to its higher frequency²⁰. In our patients, perforating venous system insufficiency shown by US duplex was the most common in both sexes, followed by superficial venous system insufficiency. There are

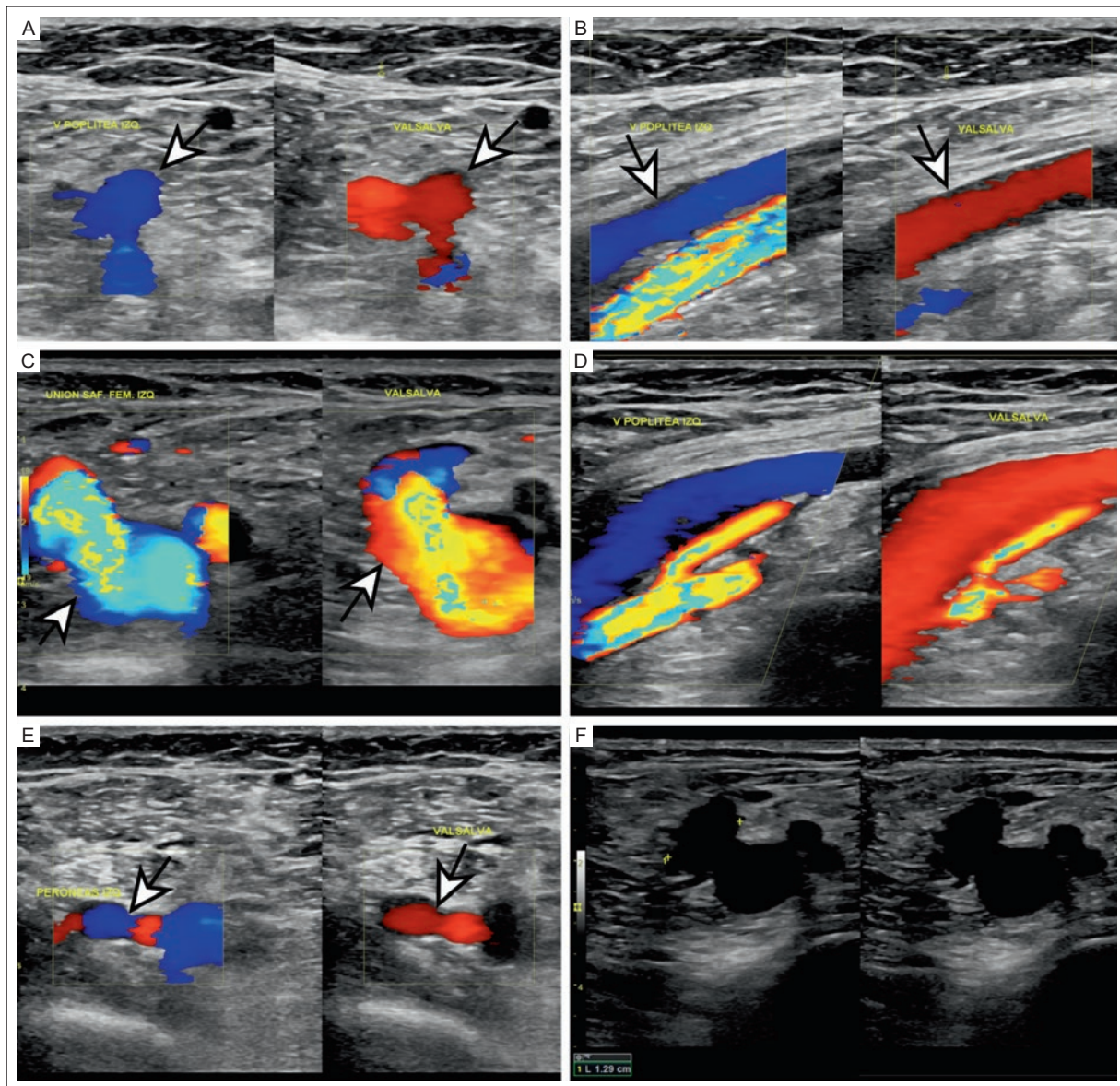


Figure 6. A 46-year-old woman with a diagnosis of CVI. The patient was examined in the decubitus position. **A:** color Doppler US, transverse view of the left popliteal vein with inversion from blue to red during the Valsalva maneuver in relation to reflux (arrows). **B:** color Doppler US, longitudinal view of the left popliteal vein with inversion from blue to red during the Valsalva maneuver in relation to reflux (arrows). **C:** color Doppler US, transverse view of the left saphenous–femoral junction showing inversion from blue to red during the Valsalva maneuver and aliasing in relation to reflux. **D:** color Doppler US, longitudinal view of the left popliteal vein, showing inversion from blue to red during the Valsalva maneuver in relation to reflux. **E:** color Doppler US, transverse view of the left peroneal veins, showing inversion from blue to red with the Valsalva maneuver in relation to reflux. **F:** grayscale US duplex, transverse view of the dilated saphenous–femoral junction with a diameter of 12.9 mm.

CVI: chronic venous insufficiency; US: ultrasound.

differences in the published reports, with superficial venous system insufficiency being the most common type of CVI in both sexes,²¹ in contrast to other reports showing that deep venous system insufficiency was more common in men^{15,18}.

The relationship between the four different venous systems by US duplex findings and their interrelationship in CVI have not been described. We found that the

combination of superficial venous and perforating venous system insufficiency was the most common association shown by US duplex, followed by the combination of deep, superficial, and perforating venous systems. The least common combination was superficial + deep + perforating + reticular venous systems. The association of the different types of CVI shown by US duplex findings indicates the variability of the interrelationships

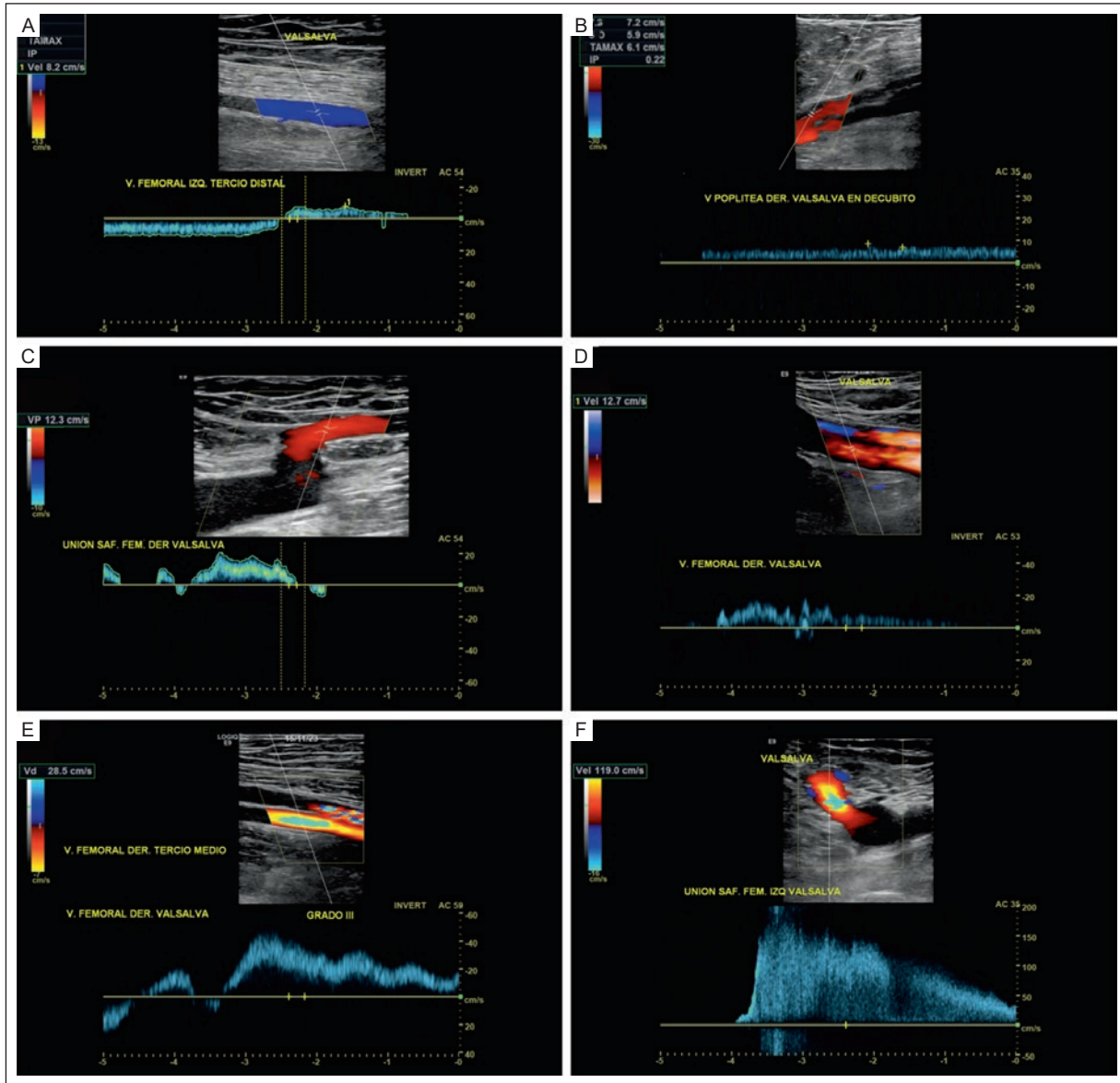


Figure 7. Classification of the three grades of CVI according to reflux velocity using US duplex, longitudinal view. **A:** the left femoral vein, distal third, showing spectral inversion with a velocity of 8.2 cm/s classified as grade 1 reflux. **B:** the right popliteal vein showing a spectral inversion with a velocity of 7.2 cm/s classified as grade 1 reflux. **C:** the right saphenofemoral junction showing spectral inversion with a velocity of 12.3 cm/s classified as grade 2 reflux. **D:** the right femoral vein showing spectral inversion with a velocity of 12.7 cm/s classified as grade 2 reflux. **E:** the right femoral vein showing spectral inversion with a velocity of 28.5 cm/s classified as grade 3 reflux. **F:** the left saphenofemoral junction showing spectral inversion with a velocity of 119 cm/s classified as grade 3 reflux.

CVI: chronic venous insufficiency; US: ultrasound.

of the four venous systems in the development of CVI. Radiologists should know the different combinations to correctly assess and report CVI.

The severity of CVI is traditionally described in terms of clinical characteristics. The Clinical-Etiology-Anatomy-Pathophysiology (CEAP) classification is an internationally recognized standard for describing CVI⁶. However, it does not include US findings, and there is

no severity classification based on US duplex examination. Venous incompetence with reflux has been associated with the development of venous ulcers^{5,21}. It has been proposed to quantify superficial venous reflux using US duplex examination, comparing vein diameter, duration of reflux, mean reflux velocity, peak reflux velocity, and total reflux volume at the three sites on the saphenous–femoral junction, great saphenous vein,

Table 3. Three-grade classification^a of superficial and deep CVI according to reflux velocity using US duplex in Mexican patients

Description	Superficial venous insufficiency			Deep venous insufficiency		
	Total (n = 322)	Women (n = 233)	Men (n = 89)	Total (n = 98)	Women (n = 58)	Men (n = 40)
Grade 1, n (%)	48 (14.9)	35 (15.0)	13 (14.6)	34 (34.7)	21 (36.2)	13 (32.5)
Grade 2, n (%)	74 (23.0)	55 (23.6)	19 (21.3)	30 (30.6)	20 (34.5)	10 (25.0)
Grade 3, n (%)	200 (62.1)	143 (61.4)	57 (64.0)	34 (34.7)	17 (29.3)	17 (42.5)

^aThe proposed classification is grade 1, from 1 to ≤ 10 cm/s; grade 2, from 11 cm/s to 20 cm/s; and grade 3, > 20 cm/s. The measurement of reflux velocity was performed with the correction of the insonation angle. CVI: chronic venous insufficiency; US: ultrasound.

and saphenous–popliteal junction which correlate with CEAP²². On the other hand, Nicolaides et al.⁵ examined the relationship between venous ulceration and ambulatory venous pressure measurements. They found that the changes ranged from 0% venous ulceration in patients with a postexercise venous pressure < 30 mm Hg to 100% in patients with a postexercise venous pressure > 90 mm Hg. These findings support the association between venous hypertension and venous ulceration in CVI. Therefore, we classified the severity of insufficiency based on reflux velocity, with grade 1 being up to 10 cm/s, grade 2 from 11 to 20 cm/s, and grade 3 above 20 cm/s. Reflux velocity is a parameter that is available at the time of the US examination. This classification by grades of deep and superficial CVI of the lower limbs according to reflux velocity by US duplex is based on the fact that chronic venous hypertension is the cornerstone of the pathophysiology of superficial and deep CVI. Therefore, the clinical manifestations of CVI may depend on the severity of chronic venous hypertension. Traditionally, only the presence or absence of reflux is reported in vascular studies by radiologists and experts in vascular US^{7,9,15}. Reflux velocity measurement is simple and reproducible and would give us relevant information about the severity of reflux in patients with CVI.

The strengths of the study are the large sample of patients, that the examination was performed by a single radiologist with expertise in vascular US, and the protocol was complete¹⁰. The study limitations include the retrospective cross-sectional design, the lack of a healthy control group, and the fact that ultrasonography is an operator-dependent method that requires formal training and thorough knowledge of the anatomy, pathophysiology, and hemodynamics of the venous system to perform an optimal assessment. No correlation between ultrasound findings and classification based on reflux velocity with CEAP was performed, and a clinical follow-up of CVI was not described.

CONCLUSION

Our study shows a complete description of the US duplex findings of the four venous systems: perforating, superficial, deep, and reticular in patients with CVI of the lower limbs, highlights the complexity of CVI, and emphasizes the need for a comprehensive examination using structured and standardized reporting¹⁰. Further studies on the proposed classification of grades of reflux and long-term follow-up of patients and their correlation with the CEAP classification are needed.

Acknowledgments

The authors thank Professor Ana M. Contreras-Navarro for her guidance in preparing and writing this scientific paper.

Funding

This research received no external funding.

Conflicts of interest

The authors declare no conflicts of interest.

Ethical disclosures

Protection of individuals. This study complies with the Declaration of Helsinki (1964) and its subsequent amendments.

Confidentiality of Data. The authors declare that they followed their center's protocol for sharing patient data.

Right to privacy and informed consent. Informed consent was not required for this observational study of information collected during routine clinical care.

Use of artificial intelligence. The authors did not use generative artificial intelligence to prepare this manuscript and/or create tables, figures, or figure legends.

REFERENCES

- Eklof B, Perrin M, Delis KT, Rutherford RB, Gloviczki P; American Venous Forum; European Venous Forum; International Union of Phlebology; American College of Phlebology; International Union of Angiology. Updated terminology of chronic venous disorders: the VEIN-TERM transatlantic interdisciplinary consensus document. *J Vasc Surg.* 2009;49(2):498-501. doi: 10.1016/j.jvs.2008.09.014.
- Brown KR, Rossi PJ. Superficial venous disease. *Surg Clin North Am.* 2013;93(4):963-982, ix-x. doi: 10.1016/j.suc.2013.04.007.
- Rabe E, Pannier-Fischer F, Broman K, Schuldt K, Stang A, Poncar C, et al. Vein Study by the German Society of Phlebology: Epidemiological study to investigate the prevalence and severity of chronic venous disorders in the urban and rural residential populations. *Phlebology.* 2003;32:1-14.
- Bergan JJ, Schmid-Schönbein GW, Smith PD, Nicolaides AN, Boisseau MR, Eklof B. Chronic venous disease. *N Engl J Med.* 2006; 355(5):488-498. doi: 10.1056/NEJMra055289.
- Nicolaides AN, Labropoulos N. Burden and Suffering in Chronic Venous Disease. *Adv Ther.* 2019;36(Suppl 1):1-4. doi: 10.1007/s12325-019-0882-6.
- Lurie F, Passman M, Meisner M, Dalsing M, Masuda E, Welch H, et al. The 2020 update of the CEAP classification system and reporting standards. *J Vasc Surg Venous Lymphat Disord.* 2020; 8(3):342-352. doi: 10.1016/j.jvsv.2019.12.075. Erratum in: *J Vasc Surg Venous Lymphat Disord.* 2021;9(1):288.
- De Maeseneer MG, Kakkos SK, Aherne T, Baekgaard N, Black S, Blomgren L, et al. Editor's Choice - European Society for Vascular Surgery (ESVS) 2022 Clinical Practice Guidelines on the Management of Chronic Venous Disease of the Lower Limbs. *Eur J Vasc Endovasc Surg.* 2022;63(2):184-267. doi: 10.1016/j.ejvs.2021.12.024. Erratum in: *Eur J Vasc Endovasc Surg.* 2022;64(2-3):284-285.
- Zalaquett E, Gunabushanam G, Vallejos A, Dahiya N. Ultrasound Evaluation of Chronic Venous Insufficiency. *Ultrasound Q.* 2023;39(1):2-9. doi: 10.1097/RUQ.0000000000000634.
- AIUM Practice Parameter for the Performance of a Peripheral Venous Ultrasound Examination. *J Ultrasound Med.* 2020;39(5):E49-E54. doi:10.1002/jum.15263.
- Figueroa-Sanchez M, Gough S, López-Mendoza M, Montero-Cedeño A. Standardized structured report for Doppler duplex ultrasound of lower extremity venous insufficiency and thrombosis: a technical note. *J Mex Fed Radiol Imaging.* 2023; 2(2):133-141. doi:10.24875/JMEXFRI.M23000045.
- Adler C, Mousa A, Rhee A, Patel MD. Varicose Veins of the Lower Extremity: Doppler US Evaluation Protocols, Patterns, and Pitfalls. *RadioGraphics.* 2022;42(7):2184-2000. doi:0.1148/rg.220057.
- Eberhardt RT, Raffetto JD. Chronic venous insufficiency. *Circulation.* 2014;130(4):333-346. doi: 10.1161/CIRCULATIONAHA.113.006898.
- Neglen P; Writing Group II of the Pacific Vascular Symposium 6; Eklof B, Kulwicki A, Davies A, Deschamps T, Garcia M, Gloviczki P, et al. Prevention and treatment of venous ulcers in primary chronic venous insufficiency. *J Vasc Surg.* 2010;52(5 Suppl):15S-20S. doi:10.1016/j.jvs.2010.05.069.
- Goel RR, Hardy SC, Brown T. Surgery for deep venous insufficiency. *Cochrane Database Syst Rev.* 2021;9(9):CD001097. doi: 10.1002/14651858.CD001097.
- Evans CJ, Allan PL, Lee AJ, Bradbury AW, Ruckley CV, Fowkes FG. Prevalence of venous reflux in the general population on duplex scanning: the Edinburgh vein study. *J Vasc Surg.* 1998;28(5):767-776. doi: 10.1016/s0741-5214(98)70051-5.
- Green D. Reticular veins, incompetent reticular veins, and their relationship to telangiectases. *Dermatol Surg.* 1998; 24 (10):1129-1141. doi: 10.1111/j.1524-4725.1998.tb04086.x.
- Stevens JP, Landon B. Opportunities to improve the quality of inpatient consultation: one hospital's investigation but an age-old struggle. *Isr J Health Policy Res.* 2022;11(1):7. doi:10.1186/s13584-022-00520-1.
- Salim S, Machin M, Patterson BO, Onida S, Davies AH. Global Epidemiology of Chronic Venous Disease: A Systematic Review with Pooled Prevalence Analysis. *Ann Surg.* 2021;274(6):971-976. doi: 10.1097/SLA.00000000000004631.
- Mansilha A, Sousa J. Pathophysiological Mechanisms of Chronic Venous Disease and Implications for Venoactive Drug Therapy. *Int J Mol Sci.* 2018;19(6):1669. doi:10.3390/ijms19061669.
- Wang Y, Hunt K, Nazareth I, Freemantle N, Petersen I. Do men consult less than women? An analysis of routinely collected UK general practice data. *BMJ Open.* 2013;3(8):e003320. doi: 10.1136/bmjopen-2013-003320.
- Carradice D. Superficial venous insufficiency from the infernal to the endothermal. *Ann R Coll Surg Engl.* 2014;96(1):5-10. doi: 10.1308/003588414X13824511650498.
- Konoeda H, Yamaki T, Hamahata A, Ochi M, Sakurai H. Quantification of superficial venous reflux by duplex ultrasound-role of reflux velocity in the assessment the clinical stage of chronic venous insufficiency. *Ann Vasc Dis.* 2014;7(4):376-382. doi: 10.3400/avd.0a.14-00047.

Unifocal, multifocal, or multicentric breast cancer distribution patterns on multiplanar breast MRI: a technical note

J.M. Ignacio Lopez-Mendez^{1,2} , Raul Delgadillo-Cristerna^{1,2} and Gerardo Rodriguez-Pulido^{1,2}

¹Department of Radiology and Imaging, Hospital de Especialidades CMNO, Instituto Mexicano del Seguro Social; ²CUCS, Universidad de Guadalajara, Guadalajara, Jalisco, Mexico

ABSTRACT

The distribution patterns of breast cancer using multiplanar contrast-enhanced breast magnetic resonance imaging (B-MRI) have been insufficiently addressed. This technical note describes and schematizes the distribution pattern of breast cancer with multiplanar B-MRI from a radiologist's point of view. Multiplanar B-MRI can determine the distribution pattern of breast cancer in the three orthogonal axes (axial, sagittal, and coronal) and define the quadrant(s) of location. The distribution patterns are unifocal (UF), multifocal (MF), and multicentric (MC), which can be presented as multicentric uniuadrant (MCUQ) or multicentric multiquadrant (MCMQ). The radiologist must differentiate the distribution patterns of breast cancer and highlight the MC variants (MCUQ and MCMQ) to avoid confusing MF with MCUQ lesions. It is important to point out that each breast cancer pattern has a different prognosis and therapy recommendations. We present a digital template that can be used for reporting breast cancer distribution patterns as complementary information to the structured and standardized report of B-MRI, allowing a clear understanding and communication of findings for multidisciplinary teams and patients. The images and schematics in this technical note have been developed for educational purposes from a radiologist's perspective.

Keywords: Breast neoplasms. Distribution patterns. Magnetic resonance imaging. Diagnostic breast imaging.

INTRODUCTION

Breast cancer is the most commonly diagnosed malignancy, with an estimated 2.3 million new cases worldwide in 2020¹. The number of breast cancer-related deaths increases every year. It is the fifth most common cancer-related death and is reported more frequently in developing countries². Contrast-enhanced breast magnetic resonance imaging (B-MRI) detects breast cancer with a sensitivity of 75.2–100% and a specificity of 83–98.4% and determines its location, size, and local extent^{3–5}.

B-MRI resolves problematic cases that cannot be defined with other methods, such as mammography and ultrasound. The indications for performing B-MRI

are local cancer staging, response to neoadjuvant treatment, axillary lymph node carcinoma of unknown origin with suspected breast cancer, and screening young patients at high risk (BRCA mutation)⁵. Multiplanar B-MRI is useful in determining the distribution pattern of breast cancer in the three orthogonal axes (axial, sagittal, and coronal) and defining the quadrant(s) of location⁶. The importance of distinguishing the distribution patterns is based on the fact that each is associated with a different prognosis, neoadjuvant/adjuvant and surgical therapy⁷.

Distribution patterns are described in BI-RADS lexicon⁸. However, the description of breast cancer distribution patterns has been insufficiently addressed from

*Corresponding author:

J.M. Ignacio Lopez-Mendez
E-mail: jemaiglome@hotmail.com

Received for publication: 03-01-2024

Accepted for publication: 12-01-2024

DOI: 10.24875/JMeXFRi.24000001

Available online: 22-03-2024

J Mex Fed Radiol Imaging. 2024;3(1):56-61

www.JMeXFRi.com

2696-8444 / © 2024 Federación Mexicana de Radiología e Imagen, A.C. Published by Permanyer. This is an open access article under the CC BY-NC-ND (<https://creativecommons.org/licenses/by-nc-nd/4.0/>).

Table 1. B-MRI distribution patterns and characteristics in 16 women with breast cancer

Case	Number of masses	KS	KS*	BI-RADS	Distribution pattern	Histologic diagnosis	Molecular subtype
1	1	7/11	10/11	6	UF	Invasive ductal carcinoma	Triple negative
2	2	10/11	-	6	MF	Invasive ductal carcinoma	Luminal B
3	2	11/11	-	6	MCUQ	Invasive ductal carcinoma	Luminal B
4	3	5/11	8/11	6	MCMQ	Invasive ductal carcinoma	Luminal B
5	1	7/11	10/11	6	UF	Invasive ductal carcinoma	Luminal B
6	4	11/11	-	6	MCMQ	Breast lymphoma	-
7	2	9/11	-	6	MCUQ	Invasive ductal carcinoma	Luminal B
8	4	10/11	-	6	MCUQ	Invasive ductal carcinoma	Luminal B
9	2	8/11	-	6	MCUQ	Invasive ductal carcinoma	Triple negative
10	2	8/11	-	6	MCUQ	Invasive ductal carcinoma	Triple negative
11	3	4/11	7/11	6	MF	Invasive ductal carcinoma	Triple negative
12	2	8/11	-	6	MCMQ	Primary neuroendocrine breast cancer	-
13	2	5/11	8/11	6	MF	Invasive ductal carcinoma	Luminal A
14	2	9/11	-	6	MCMQ	Invasive ductal carcinoma	Luminal B
15	3	6/11	9/11	6	MCMQ	Invasive ductal carcinoma	Luminal B
16	2	8/11	-	6	MCMQ	Invasive ductal carcinoma	Luminal B

UF: unifocal; MF: multifocal; MCUQ: multicentric uniuadrant; MCMQ: multicentric multiquadrant; KS: kaiser score; KS*: modified kaiser score; BI-RADS: Breast Imaging Report and Data System; B-MRI: breast magnetic resonance imaging.

a radiologist's point of view. This technical note is based on daily clinical radiological practice in the imaging assessment of patients treated by a multidisciplinary breast cancer committee. This technical note aims to describe and schematize the distribution patterns of breast cancer using multiplanar B-MRI for educational purposes from a radiologist's perspective. It provides a template that can be used for reporting distribution patterns of breast cancer as complementary information to the B-MRI report.

Distribution pattern definitions

Unifocal pattern (UF): a single lesion in a single breast regardless of its location^{9,10}.

Multifocal pattern (MF): ≥ 2 lesions in a single breast in a single quadrant with a distance < 5 cm^{9,10}.

Multicentric uniuadrant pattern (MCUQ): ≥ 2 lesions in a single breast in a single quadrant with a distance > 5 cm^{9,10}.

Multicentric multiquadrant pattern (MCMQ): ≥ 2 lesions in a single breast in ≥ 2 quadrants regardless of their distance^{9,10}.

Image acquisition and analysis protocol

A GETM resonator (Discovery 750w, 3.0T, 2011; General Electric Healthcare, Milwaukee, WI, USA) with a dedicated SentinelleTM breast antenna (Sentinelle Breast Coil Riser, 2019; In vivo Corp. Gainesville, FL, USA) was used. Multiplanar axial sequences in T1, T2 SPAIR (Spectral Attenuation Inversion Recovery), DWI (diffusion-weighted imaging), ADC (apparent diffusion coefficient), T1 volume imaging for breast assessment (VIBRANT) dynamic multiphase with contrast injection and subtractions were acquired for both mammary glands. Contrast injection for the dynamic T1 VIBRANT dynamic multiphase sequences was performed with a MEDRAD[®] injector (MEDRAD Spectris Solaris EP, 2019; Indianola, PA, USA) using gadolinium (*Gadovist*[®]) 0.1 mmol/kg at 3 mL/s with a consecutive push of normal saline (NaCl 0.9%) 20 mL at 4 mL/s.

Image analysis was performed on an AWTM workstation (Advanced Workstation 4.7, MRI BREAST, 2016, General Electric Healthcare, Milwaukee, WI, USA). Lesions were assessed according to the BI-RADS

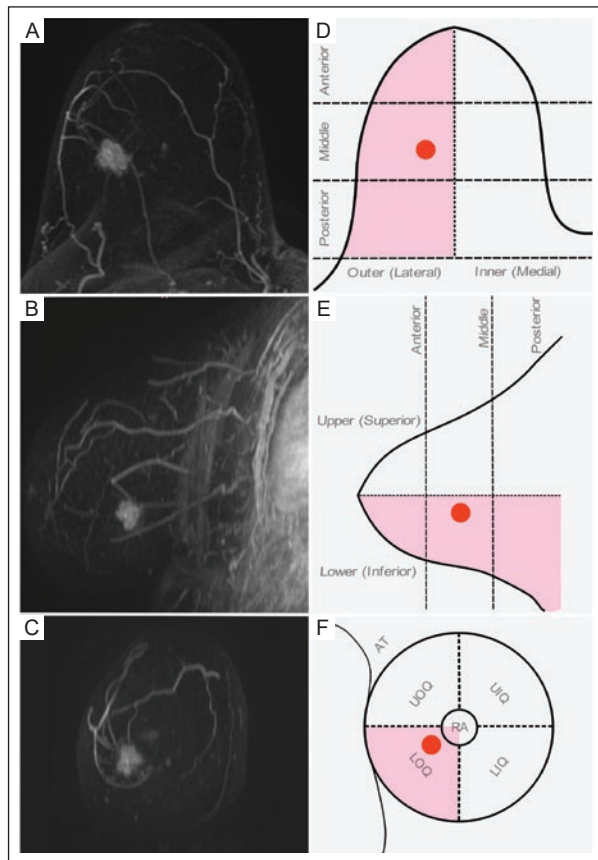


Figure 1. B-MRI of a 49-year-old woman with triple-negative molecular subtype IDC in the right breast with a unifocal distribution pattern. **A:** axial plane, **B:** sagittal plane, **C:** coronal plane showing an irregular spiculated mass with heterogeneous enhancement and AVS (KS 7/11, KS* 10/11) in the T1+C sequence (Sub Ph2, MIP) toward LOQ in the middle third. **D, E, and F:** schematic representation of the unifocal pattern. The lesion (red circle) is located in only one quadrant (pink). The unifocal pattern is only a single lesion in a single breast, regardless of its location (UOQ, UIQ, LOQ, LIQ, and RA).

AT: axillary tail; AVS: adjacent vessel sign; B-MRI: breast magnetic resonance imaging; IDC: invasive ductal carcinoma; KS: Kaiser score; KS*: modified Kaiser score; LIQ: lower inner quadrant; LOQ: lower outer quadrant; MIP: maximum intensity projection; RA: retroareolar; Sub Ph2: subtraction of the second contrast phase; T1+C: T1 sequence with multiphase contrast; UIQ: upper inner quadrant; UOQ: upper outer quadrant.

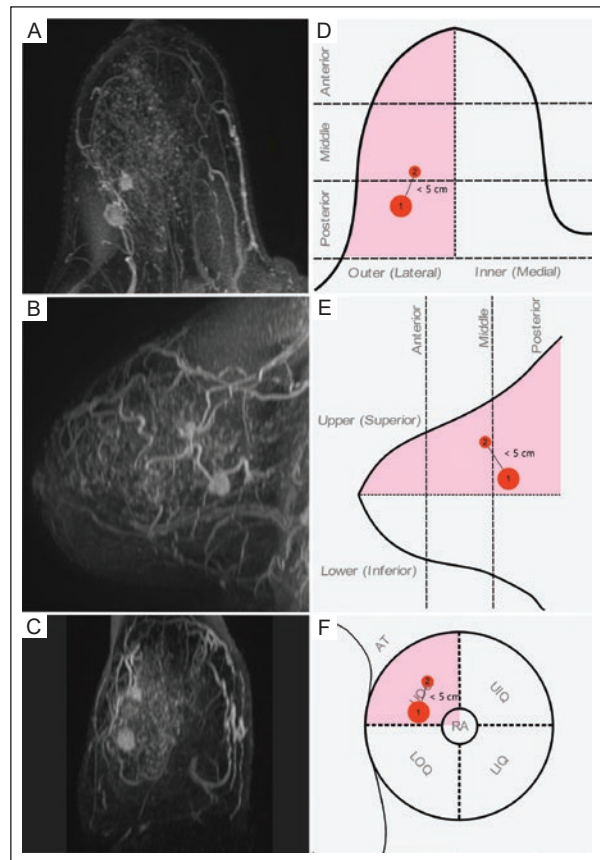


Figure 2. B-MRI of a 56-year-old woman with luminal molecular subtype B IDC in the right breast with a multifocal distribution pattern. **A:** axial plane, **B:** sagittal plane, **C:** coronal plane showing two irregular spiculated masses with heterogeneous enhancement and AVS (KS 10/11) in the T1+C sequence (Sub Ph2, MIP) toward the UOQ in its middle/posterior third. **D, E, and F:** schematic representation of the multifocal pattern. Note that the lesions (red circles) are located in a single quadrant (pink color) at a distance of < 5 cm from each other. The term multifocal pattern is ≥ 2 lesions in a single breast in a single quadrant (UOQ, UIQ, LOQ, and LIQ) with a distance < 5 cm. The masses were numbered for multiplanar identification.

AT: axillary tail; AVS: adjacent vessel sign; B-MRI: breast magnetic resonance imaging; IDC: invasive ductal carcinoma; KS: Kaiser score; LIQ: lower inner quadrant; LOQ: lower outer quadrant; MIP: maximum intensity projection; RA: retroareolar; Sub Ph2: subtraction of the second contrast phase; T1+C: T1 sequence with multiphase contrast; UIQ: upper inner quadrant; UOQ: upper outer quadrant.

categories, the Kaiser score, and the modified Kaiser¹¹ by a breast imaging radiologist (RDC) with 25 years of experience.

Description of the clinical cases

The characteristics and distribution patterns of lesions by B-MRI in 16 women with breast cancer are shown in Table 1. The number of masses, Kaiser score, modified

Kaiser score, BI-RADS, distribution pattern, histological diagnosis, and the molecular subtype were recorded. The breast cancer quadrant location was determined by multiplanar B-MRI (axial, sagittal, and coronal) using Sub Ph2 sequences in maximum intensity projection (MIP). Then, the type of distribution pattern was defined. A representative case of each distribution pattern was selected to develop the diagrams depicting each breast cancer distribution pattern in a multiplanar B-MRI view.

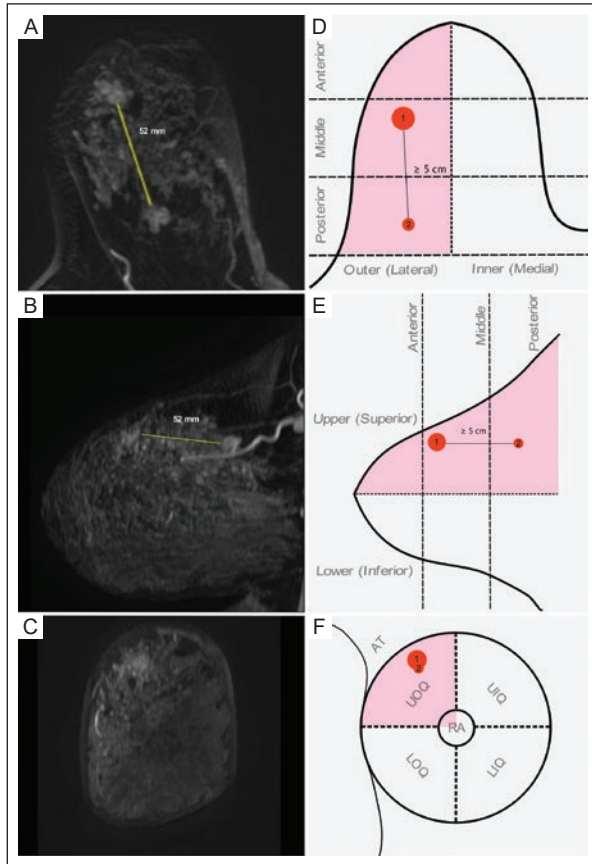


Figure 3. B-MRI of a 41-year-old woman with luminal B molecular subtype IDC in the right breast with a multicentric uniquadrant distribution pattern. **A:** axial plane, **B:** sagittal plane, **C:** coronal plane showing two spiculated masses with heterogeneous enhancement (KS 11/11) and a distance of 52 mm (yellow line) in the T1+C sequence (Sub Ph2, MIP) toward the UOQ in the middle and posterior third. **D, E, and F:** schematic representation of the multicentric uniquadrant pattern. Note how the lesions (red circles) lie in a single quadrant (pink color) but are separated by ≥ 5 cm. This pattern is ≥ 2 lesions in a single quadrant of a single breast (UOQ, UIQ, LOQ, and LIQ) separated by ≥ 5 cm. The masses were numbered for multiplanar identification.

AT: axillary tail; B-MRI: breast magnetic resonance imaging; IDC: invasive ductal carcinoma; KS: Kaiser score; LIQ: lower inner quadrant; LOQ: lower outer quadrant; MIP: maximum intensity projection; RA: retroareolar; Sub Ph2: subtraction of the second contrast phase; T1+C: T1 sequence with multiphase contrast; UIQ: upper inner quadrant; UOQ: upper outer quadrant.

Unifocal (UF) pattern

Case 1 is a 49-year-old woman with invasive ductal carcinoma (IDC), with a molecular subtype triple-negative. B-MRI showed an irregular spiculated mass with heterogeneous enhancement in the lower outer quadrant of the right breast, middle third (Figure 1A, B, and C). Multiplanar diagrams illustrate the characteristics of the UF distribution pattern (Figures 1D, E, and F). The unifocal pattern is only a single lesion in a single breast, regardless of its location.

Multifocal (MF) pattern

Case 2 is a 56-year-old woman with an IDC, with a molecular subtype luminal B. B-MRI showed two irregular spiculated masses with heterogeneous enhancement in the right breast toward the upper outer quadrant, middle third (Figures 2A, B, and C). Multiplanar diagrams illustrate the characteristics of the MF distribution pattern (Figures 2D, E, and F). A multifocal pattern is ≥ 2 lesions in a single breast in a single quadrant with a distance of < 5 cm. Masses were numbered for multiplanar identification.

Multicentric uniquadrant (MCUQ) pattern

Case 3 is a 41-year-old woman with an IDC, with a molecular subtype luminal B. B-MRI showed two irregular spiculated masses with heterogeneous enhancement in the right breast extending toward the upper outer quadrant in the middle and posterior third, separated by 52 mm from each other (Figures 3A, B, and C). The multiplanar diagrams illustrate the characteristics of the MCUQ distribution pattern (Figures 3D, E, and F). The multicentric uniquadrant pattern is ≥ 2 lesions located in a single quadrant of a single breast, separated by ≥ 5 cm. Masses were numbered for multiplanar identification.

Multicentric multiquadrant (MCMQ) pattern

Case 4 is a 35-year-old woman with an IDC, with a molecular subtype luminal B. B-MRI showed three irregular masses with heterogeneous enhancement in the right breast in the upper outer, upper inner, and lower outer quadrants (Figure 4A, B, and C). The multiplanar diagrams illustrate the characteristics of the MCMQ distribution pattern (Figure 4D, E, and F). A multicentric multiquadrant pattern is ≥ 2 lesions in ≥ 2 quadrants of a single breast. Masses were numbered for multiplanar identification.

Template of breast cancer distribution patterns

We provide a digital template (supplementary material) that can be downloaded and used for reporting breast cancer distribution patterns as complementary information to the structured and standardized report of the B-MRI to allow clear communication of findings to the multidisciplinary team who can offer the patient the best available therapy.

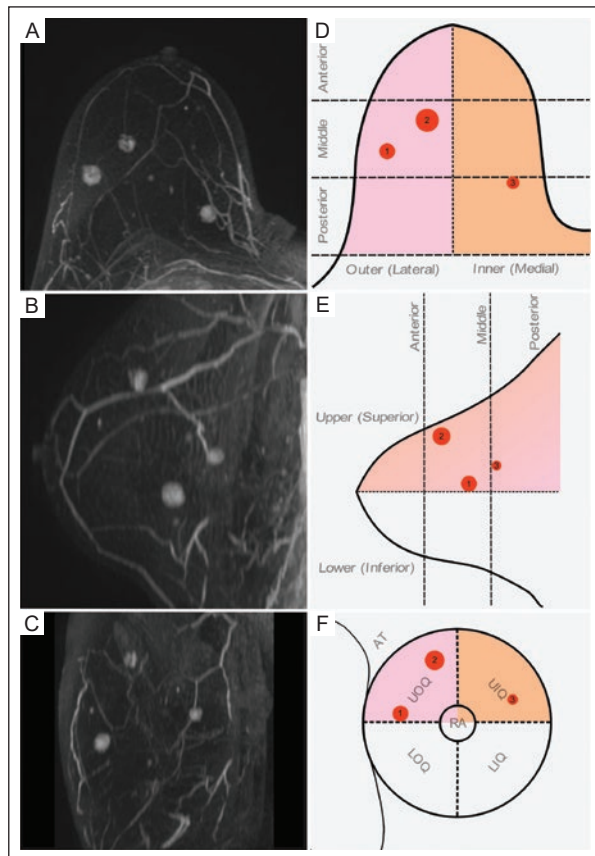


Figure 4. PB-MRI of a 35-year-old woman with luminal molecular subtype B IDC in the right breast with a multicentric multiquadrant distribution pattern. **A:** axial plane, **B:** sagittal plane, **C:** coronal plane showing three irregular masses with heterogeneous enhancement and AVS (KS 5/11, KS* 8/11) in the T1+C sequence (Sub Ph2, MIP) toward UOQ and UIQ in the middle/posterior third. **D, E, and F:** schematic representation of the multicentric multiquadrant pattern showing how the lesions (red circles) are localized in more than one quadrant (pink and orange). A multicentric multiquadrant distribution pattern is ≥ 2 lesions located in ≥ 2 quadrants of a single breast. The masses were numbered for multiplanar identification.

AT: axillary tail; AVS: adjacent vessel sign; B-MRI: breast magnetic resonance imaging; IDC: invasive ductal carcinoma; KS: Kaiser score; KS*: modified Kaiser score; LIQ: lower inner quadrant; LOQ: lower outer quadrant; MIP: maximum intensity projection; RA: retroareolar; Sub Ph2: subtraction of the second contrast phase; T1+C: T1 sequence with multiphase contrast; UIQ: upper inner quadrant; UOQ: upper outer quadrant.

DISCUSSION

The B-MRI images and template in this technical note facilitate recognizing breast cancer distribution patterns from a radiologist's point of view and allow correct identification by multidisciplinary teams and patients. The radiologist must differentiate the distribution patterns of breast cancer, emphasizing the two presentations of the MC pattern (MCUQ and MCMQ) to avoid confusion of the MF pattern with an MCUQ pattern.

According to Bendifallah et al.¹², the description of distribution patterns dated back to 1977 when Lagios, a pathologist specializing in breast pathology, described the MF distribution pattern as tumor foci in the same quadrant of the same breast and the MC distribution pattern as tumor foci in different quadrants or more than 5 cm in the same breast. Most MF and MC distribution pattern publications can be found in pathology, oncology, and surgical oncology journals, from the perspective of these specialties⁹. In a recently published systematic review and meta-analysis, Zhang et al.⁹ selected 31 studies published in oncology and/or oncosurgery journals. Of these, only 5 studies included imaging and pathology methods for detecting tumor foci and determining lesion distribution patterns, but none addressed the radiologist's perspective in determining the type of distribution pattern⁹. Thus, this technical note provides graphical representations of breast cancer distribution patterns on B-MRI as a standardized and complete description for radiologist that optimizes the radiological report using a template. The radiologist's point of view in reporting breast cancer distribution patterns is critical for therapeutic decisions that impact prognosis. In countries where resources are limited, conservative surgery should be avoided in MC breast cancer¹³.

MF and MC pattern descriptions vary considerably in the literature, particularly in relation to the distance between foci¹⁴. The ACR BI-RADS fifth edition only cites the MF and MC patterns in the MRI section but does not list specific schemas of these entities⁸. Only O'Brien¹⁰, an oncological breast cancer surgeon, showed a simplified scheme in the coronal plane that illustrates the MF and MC patterns without showing their multiplanar (axial or sagittal) translation¹⁰. In a case-based review published in 2011, Dueñas et al.¹⁵ a group of radiologists, defined the MF and MC distribution pattern from an imaging perspective but without diagrams illustrating their multiplanar features¹⁵. A systematic review and meta-analysis by Zhang et al.⁹ provided homogeneity in the definitions of MF and MC. Their descriptions are important, as these lesions are more biologically aggressive and pose a higher risk of mortality and metastasis, with a combined incidence ranging from 6% to 60%⁹. Radiologists must use these standardized definitions for MF and MC pattern, using a homogeneous lexicon in clear and complete B-MRI descriptions.

CONCLUSION

The images and schematics in this technical note have been developed for educational purposes from a

radiologist's perspective. The use of the structured and standardized reporting template for the distribution pattern of breast cancer on multiplanar B-MRI can (a) impact patient care by facilitating clear communication of the distribution pattern to the treating oncologists, surgeons, and pathologists; (b) be a visual guide for radiology trainees; (c) be useful for data comparison and reproducibility in research; and (d) help patients understand their disease.

Acknowledgments

The authors thank Professor Ana M. Contreras-Navarro for her guidance in preparing and writing this scientific paper.

Funding

This paper received no external funding.

Conflicts of interest

The authors declare no conflicts of interest.

Ethical disclosures

Protection of individuals. This study was conducted in compliance with the Declaration of Helsinki (1964) and its subsequent amendments.

Data confidentiality. The authors declare that they followed their center's protocol for sharing patient data.

Right to privacy and informed consent. Informed consent was not required to analyze and publish routinely acquired clinical and imaging data.

Use of artificial intelligence. The authors state that they did not use generative artificial intelligence to prepare this manuscript and/or create tables, figures, or figure legends.

Supplementary material

The digital blank template of the multiplanar B-MRI diagrams of the right and left breast is provided as complementary material for use in clinical practice, teaching, or research.

Supplementary data are available online in the Journal online DOI: 10.24875/JMEXFRI.24000001. These data are provided by the corresponding author and published online for the reader's benefit. The contents of supplementary data are the sole responsibility of the authors.

REFERENCES

1. Sung H, Ferlay J, Siegel RL, Laversanne M, Soerjomataram I, Jemal A, et al. Global Cancer Statistics 2020: GLOBOCAN Estimates of Incidence and Mortality Worldwide for 36 Cancers in 185 Countries. *CA Cancer J Clin.* 2021;71(3):209-249. doi:10.3322/caac.21660.
2. Łukasiewicz S, Czezelewski M, Forma A, Baj J, Sitarz R, Stanisławek A. Breast Cancer-Epidemiology, Risk Factors, Classification, Prognostic Markers, and Current Treatment Strategies-An Updated Review. *Cancers (Basel).* 2021;13(17):4287. doi:10.3390/cancers13174287.
3. Steinhof-Radwańska K, Lorek A, Holecki M, Barczyk-Gutkowska A, Grażyńska A, Szczudło-Chraścina J, et al. Multifocality and Multicentricity in Breast Cancer: Comparison of the Efficiency of Mammography, Contrast-Enhanced Spectral Mammography, and Magnetic Resonance Imaging in a Group of Patients with Primarily Operable Breast Cancer. *Curr Oncol.* 2021; 28(5):4016-4030. doi:10.3390/curroncol28050341.
4. Xiao J, Rahbar H, Hippe DS, Rendi MH, Parker EU, Shekar N, et al. Dynamic contrast-enhanced breast MRI features correlate with invasive breast cancer angiogenesis. *NPJ Breast Cancer.* 2021;7(1):42. doi: 10.1038/s41523-021-00247-3.
5. Mann RM, Cho N, Moy L. Breast MRI: State of the Art. *Radiology.* 2019;292(3):520-536. doi: 10.1148/radiol.2019182947.
6. Thomassin-Naggara I, Trop I, Lalonde L, David J, Pélouquin L, Chopier J. Tips and techniques in breast MRI. *Diagn Interv Imaging.* 2012;93(11):828-839. doi:10.1016/j.diii.2012.06.004.
7. Li S, Wu J, Huang O, He J, Chen W, Li Y, et al. Association of Molecular Biomarker Heterogeneity with Treatment Pattern and Disease Outcomes in Multifocal or Multicentric Breast Cancer. *Front Oncol.* 2022;12:833093. doi:10.3389/fonc.2022.833093.
8. Morris EA, Comstock CE, Lee CH, Lehman CD, Newstead GM, Tozaki M, et al. ACR BI-RADS® Magnetic Resonance Imaging. In: D'Orsi CJ, editor. *ACR BI-RADS® Atlas, Breast Imaging Reporting and Data System.* 5th ed. 5th ed. Reston, VA (USA). American College of Radiology; 2013. p. 377, 442.
9. Zhang Y, Liu F, Gao Q, Chai Y, Ren Y, Tian H, et al. Comparing the outcome between multicentric/multifocal breast cancer and unifocal breast cancer: A systematic review and meta-analysis. *Front Oncol.* 2022;12:1042789. doi:10.3389/fonc.2022.
10. O'Brien MJ. Invasive/Infiltrating Lobular Carcinoma (ILC) [Internet]. Melbourne Breast Cancer Surgery; 2018 [cited 2023 July 03]. Available from: <https://www.melbournebreastcancersurgery.com.au/wp-content/themes/ypo-theme/pdf/infiltrating-lobular-carcinoma-18th-july-p1.pdf>.
11. Zhou XZ, Liu LH, He S, Yao HF, Chen LP, Deng C, et al. Diagnostic value of Kaiser score combined with breast vascular assessment from breast MRI for the characterization of breast lesions. *Front Oncol.* 2023;13:1165405. doi:10.3389/fonc.2023.
12. Bendifallah S, Werkoff G, Borie-Moutafoff C, Antoine M, Chopier J, Gligorov J, et al. Multiple synchronous (multifocal and multicentric) breast cancer: clinical implications. *Surg Oncol.* 2010;19(4):e115-123. doi: 10.1016/j.suronc.2010.06.001.
13. Cardenas-Sanchez JC, Bargallo-Rocha JE, Cervantes-Sanchez G, Arce-Salinas C, Bautista-Piña V, Chavez-MacGregor MC, et al. Mexican Consensus on diagnosis and treatment of breast cancer [Internet]. Version 10. Mexico City (Mexico); [cited 2023 July 03]; p. 79. Available from: http://consensocancermamario.com/documentos/FOLLETO_CONSENSO_DE_CANCER_DE_MAMA_10aRev2023a.PDF
14. Avera E, Valentic L, Bui L. Current understanding and distinct features of multifocal and multicentric breast cancers. *Cancer Rep (Hoboken).* 2023;6(9):e1851. doi: 10.1002/cnr2.1851.
15. Dueñas VP, Gopegui-Andreu MR, Hodge SM, Manrique AS. Breast Magnetic Resonance Imaging of Multicentric, Multifocal and Bilateral Cancer - A Case-based Review. *Eur Oncol.* 2011;7:24. doi: 10.17925/EOH.2011.07.01.24.

US findings of uterine and ovarian herniation through the Nuck canal: a case report

Daniel R. Cantu-Alejo^{ID}*, Claudia Y. Rodriguez-Garza, Caleb Tadeo-Mata, Gerardo E. Ornelas-Cortinas, and Alberto Montemayor-Martinez

Radiology and Imaging Service, University Center for Diagnostic Imaging, "Dr. Jose E. Gonzalez" University Hospital, Universidad Autonoma de Nuevo Leon. Monterrey, Nuevo Leon, Mexico

ABSTRACT

The processus vaginalis peritonei, a tubular fold of the peritoneum that invaginates into the inguinal canal, called the canal of Nuck, is normally obliterated in women. However, if the processus vaginalis remains open, the parietal peritoneum extends through the inguinal canal to the labia majora, resulting in a Nuck canal hernia (NCH). High-frequency ultrasound (US) is the initial method preferred for the diagnosis of NCH. The aim of this case report is to describe the US findings in a 2-month-old girl with pelvic swelling diagnosed as an NCH involving the uterus and ovary. A pelvic US of the left labia majora showed a hernia sac with fatty ovarian and partial uterine contents. The ovary measured 1.6 x 0.9 x 0.8 cm without adequate blood flow on color and power Doppler. Blood flow was visible in the pedicle. Fluid, edema, and increased adjacent soft tissue echogenicity were also noted in the hernia sac, findings consistent with NCH. Subsequent surgical reduction was performed to avoid complications due to the loss of blood supply to the ovary. This case report is the first from Mexico to highlight the findings of NCH of the uterus and ovary. It is presented for educational purposes.

Keywords: Nuck canal hernia. Labia majora. Sonography. Uterus. Ovary. Case report.

INTRODUCTION

The incidence of inguinal hernias ranges from 9% to 11% in preterm infants of any term to 30% in very low birth weight (less than 1000 g) preterm infants, and 15% to 20% of all Nuck canal hernias (NCH) in infancy occur with ovaries with or without fallopian tubes^{1,2}. The processus vaginalis is normally obliterated in the first year of life³. However, if the processus vaginalis remains open⁴, the parietal peritoneum extends through the inguinal canal to the labia majora, leading to an NCH⁵. It is a rare congenital condition that is more common in young girls in the first year of life⁶. It manifests as a swelling at the level of the labia majora^{7,8}.

NCH can potentially lead to irreversible complications; therefore, prompt recognition and intervention are critical to prevent the complications associated with this condition. Color and grayscale Doppler US are the imaging modalities of choice for evaluating soft tissue and superficial masses due to the rapid acquisition of images that define the composition of the mass, the complications characterized by blood flow changes or associated with a hydrocele, such as infection or hemorrhage, and the location and associated hernia contents and their characterization in differential diagnoses¹. Multimodality procedures, such as computed tomography or magnetic resonance imaging, are not recommended in most cases⁹. The aim of this case report is

*Corresponding author:

Daniel R. Cantu-Alejo
E-mail: daniel.cantualj@uanl.edu.mx

Received for publication: 21-12-2022

Accepted for publication: 31-01-2024

DOI: 10.24875/JMeXFRi.22000017

Available online: 22-03-2024

J Mex Fed Radiol Imaging. 2024;3(1):62-65

www.JMeXFRi.com

2696-8444 / © 2024 Federación Mexicana de Radiología e Imagen, A.C. Published by Permanyer. This is an open access article under the CC BY-NC-ND (<https://creativecommons.org/licenses/by-nc-nd/4.0/>).

to describe the US findings in a 2-month-old girl with pelvic swelling diagnosed as an NCH involving the uterus and ovary.

Clinical case description

The patient was a 2-month-old girl with no relevant clinical history. The mother had six prenatal examinations during her entire pregnancy. The child was delivered by cesarean section in the 34th week of pregnancy due to gestational hypertension. At birth, the infant weighed 1,690 kg and measured 42 cm. On admission to the hospital, the infant had a fever of 38°C. Vital signs were within the expected percentile for her age. No infectious focus was detected on physical examination. The fever may have been a reaction after recent BCG, hexavalent, pneumococcal, and rotavirus vaccinations.

Swelling was noted on the left labia majora at the pelvis level (Figure 1). A physical examination was performed, searching for a reduction in size, skin changes, or tenderness. A soft tissue US examination was performed to assess the nature and extent of the swelling of the left labia majora.

Imaging findings

The grayscale and color Doppler US images of the soft tissues were performed with a high-resolution 7 - 12 MHz¹¹ transducer and analyzed in a Picture Archiving and Communication (PAC) system on Philips Epiq 5qTM Affinity 50gTM equipment (Philips Medical Systems, Amsterdam, The Netherlands).

The US images showed a 1.1 cm hernia defect (Figure 2) located subcutaneously in the left inguinal region. The dimensions of this irreducible hernia sac were 3.4 x 2.6 x 1.7 cm. It contained fatty tissue, ovaries, and a partial uterine component with an endometrial-like appearance. The ovary measured 1.6 x 0.9 x 0.8 cm and did not have sufficient blood flow on color and power Doppler US (Figure 3); however, blood flow was evident in the pedicle. In addition, fluid, edema, and increased echogenicity were noted in the surrounding soft tissues of the hernia sac. These findings were consistent with NCH confirmed by hernioplasty.

Clinical outcome

Hernioplasty was performed to reduce the NCH surgically. The defect was corrected, and the pelvic structures returned to their original anatomical position without postsurgical complications.



Figure 1. A 2-month-old girl with swelling in the left inguinal region and genital labia majora (dotted circle).

DISCUSSION

The NCH in this case report involved important elements such as the uterus and ovary with findings and complications such as the absence of ovarian blood flow demonstrated by Doppler US and successfully treated surgically by left inguinal hernioplasty. This case report is the first in Mexico of a NCH involving the uterus and ovary. It is presented for educational purposes.

Color and grayscale Doppler US are useful tools in the preoperative evaluation of entities such as NCH, with a sensitivity of 93% and a specificity of 88%. They have been consistently shown to accurately diagnose contralateral patencies with a higher risk of developing into hernias⁴. In this case report, color Doppler ultrasound did not detect adequate flow within the hernia contents towards the left labia majora; therefore, hernioplasty was performed immediately.

The ultrasonographic findings of NCH described in the literature include patency of Nuck's canal, herniated contents, and evidence of an ischemic injury to these structures¹. In this case report, ultrasonography showed findings consistent with NCH, including the extent and structures involved, confirmed by surgery. Jedrzejewski et al.⁵ showed that 1 in 10 patients with surgically confirmed ovarian hernias in Nuck's canal also contained a uterus, with the latter occurring in 15 to 20% of hernias,

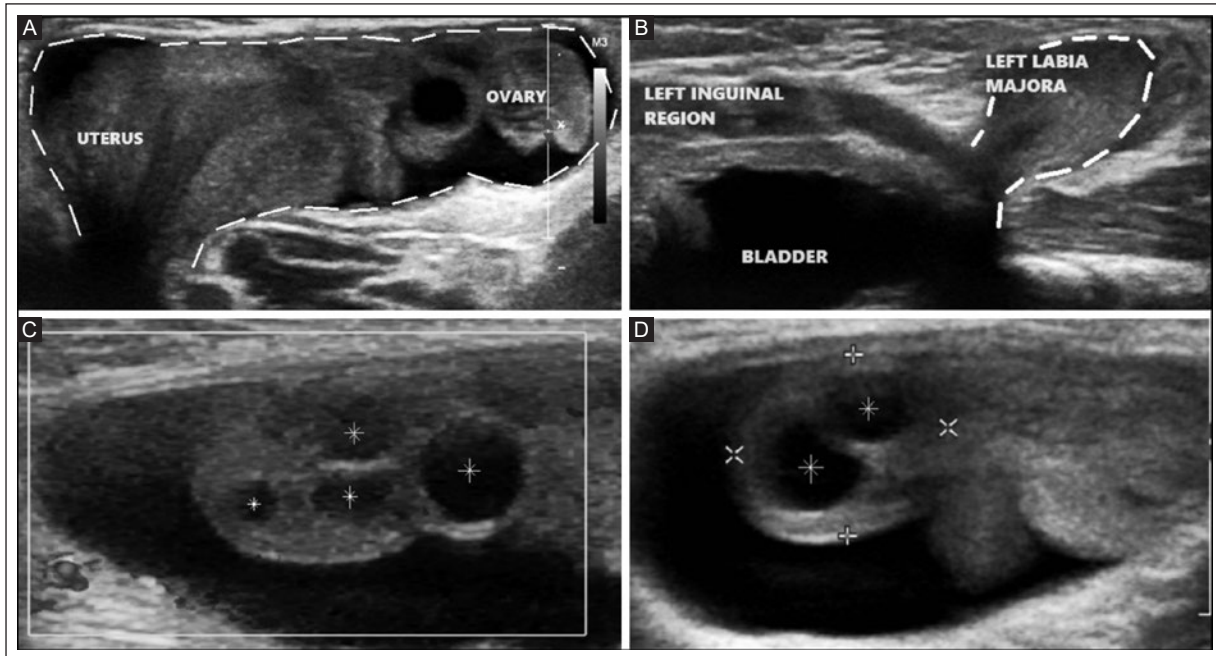


Figure 2. A 2-month-old girl with swelling in the left inguinal region and labia majora. **A:** grayscale US, sagittal view of the entire hernia sac (dashed line) with the presence of the uterus and ovary. **B:** grayscale US, sagittal view showing the relationship of the hernia sac (dashed line) to the bladder and left inguinal region. **C:** power US Doppler; a sagittal view of the left ovary inside the hernia sac showing lack of flow and characteristic follicles (asterisks). **D:** grayscale US; cross-sectional view of the ovary (calipers) with characteristic follicles (asterisks). US: ultrasound.

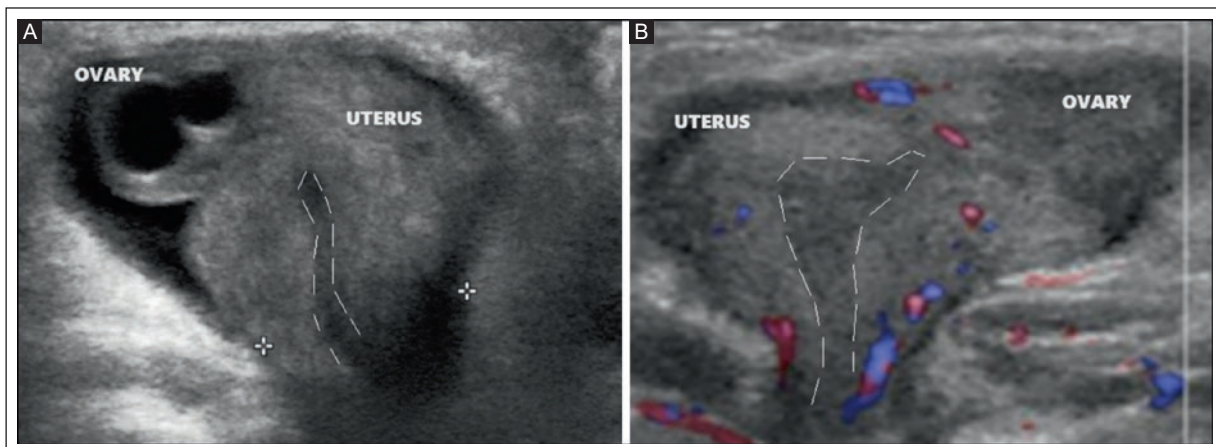


Figure 3. A 2-month-old girl with swelling in the left inguinal region and labia majora. **A:** grayscale US sagittal view of the hernia contents. Endometrial tissue is visible in the uterus (dashed line). An ovary can also be observed. **B:** power US Doppler, oblique sagittal view showing uterine vascularity. Endometrial tissue (dashed line) is visible in the uterus. US: ultrasound.

demonstrating its rarity. Physical examination and performing simple maneuvers such as reducing the lesion, skin changes, tenderness, and transillumination, in addition to laparoscopic exploration, can reduce the incidence of false-negative findings for patent processus

vaginalis in children¹⁰⁻¹². Therefore, radiologists must familiarize themselves with an NCH to accurately diagnose it and avoid complications.

The bowel, hydrocele, and pelvic structures, such as the ovaries, fallopian tubes, bladder, and uterus,

may be contained in the NCH. The presence of ovarian follicles or endometrium is useful for diagnosing pelvic structures in an NCH, including the uterus and ovary² In Mexico, this pathology has been previously described as involving pelvic-abdominal structures, such as the fallopian tubes and Nuck's canal cysts, only in adults¹³⁻¹⁵. Saguintaah et al.¹ mention that a hernia involving the uterus and ovary has been reported in at least 9 pediatric patients under 1 year of age. They describe a case of NCH involving the uterus, both ovaries, and a fallopian tube in a 3-month-old child who was born prematurely at 28 weeks of gestation with an irreducible hernia on the left side. No signs of ischemia were found during the preoperative examination. It is important to recognize the imaging findings early to avoid complications that affect the patient's quality of life⁵.

CONCLUSION

In this case report, US examination, the preferred imaging modality for NCH diagnosis, showed specific findings for the diagnosis of NCH to guide early surgical treatment and avoid complications due to a loss of blood supply to pelvic and other structures. Despite its low incidence, it is important to consider NCH as a differential diagnosis when approaching an inguinal mass in a female child.

Acknowledgments

The authors thank Professor Ana M. Contreras-Navarro for her guidance in preparing and writing this scientific paper.

Funding

This research received no external funding.

Conflicts of interest

The authors declare no conflicts of interest.

Ethical disclosures

Protection of human and animal subjects. The authors declare that the procedures were in accordance

with the regulations of the relevant clinical research ethics committee and those of the Code of Ethics of the World Medical Association (Declaration of Helsinki).

Confidentiality of data. The authors declare they followed the protocols of their work center on the publication of patient data.

Right to privacy and informed consent. Informed consent was not required for this case report of routinely acquired clinical data.

Use of artificial intelligence. The authors state that they did not use generative artificial intelligence to prepare this manuscript or create figures or figure legends.

REFERENCES

1. Saguintaah M, Eulliot J, Bertrand M, Prodhomme O, Béchard N, Bolivar-Perrin J, et al. Canal of Nuck Abnormalities in Pediatric Female Patients. *Radiographics*. 2022;42(2):541-558. doi: 10.1148/rg.210145.
2. Thomas AK, Teague CT, Jancelewicz T. Canal of Nuck hernia containing pelvic structures presenting as a labial mass. *Radiol Case Rep*. 2018;13:534-536. doi:10.1016/j.radcr.2018.02.007.
3. Shadbolt CL, Heinze SB, Dietrich RB. Imaging of groin masses: inguinal anatomy and pathologic conditions revisited. *Radiographics*. 2001;21 Spec No:S261-271. doi: 10.1148/radiographics.21.suppl1.g01oc17s261.
4. Brainwood M, Beirne G, Fenech M. Persistence of the processus vaginalis and its related disorders. *Australas J Ultrasound Med*. 2020;23(1):22-29. doi:10.1002/ajum.12195.
5. Jedrzejewski G, Osemlak P, Wieczorek AP, Nachulewicz P. Nuck Canal Hernias, Typical and Unusual Ultrasound Findings. *Ultrasound Q*. 2019;35(1): 79-81. doi:10.1097/RUQ.0000000000000409.
6. Sameshima YT, Yamanari MG, Silva MA, Neto MJ, Funari MB. The challenging sonographic inguinal canal evaluation in neonates and children: an update of differential diagnoses. *Pediatr Radiol*. 2017; 47(4):461-472. doi:10.1007/s00247-016-3706-8.
7. Nasser H, King M, Rosenberg HK, Rosen A, Wilck E, Simpson WL. Anatomy and pathology of the canal of Nuck. *Clin Imaging*. 2018; 51: 83-92. doi:10.1016/j.clinimag.2018.02.003.
8. Okada T, Sasaki S, Honda S, Miyagi H, Minato M, Todo S. Irreducible indirect inguinal hernia containing uterus, ovaries, and Fallopian tubes. *Hernia*. 2012;16(4): 471-473. doi: 10.1007/s10029-010-0764-y.
9. Rees MA, Squires JE, Tadros S, Squires JH. Canal of Nuck hernia: a multimodality imaging review. *Pediatr Radiol*. 2017;47(8):893-898. doi:10.1007/s00247-017-3853-6.
10. Yeap E, Pacilli M, Nataraja RM. Inguinal hernias in children. *Aust J Gen Pract*. 2020;49(1-2):38-43. doi: 10.31128/AJGP-08-19-5037.
11. Jansen CJ, Yelder PC. Evaluation of hernia of the male inguinal canal: sonographic method. *J Med Radiat Sci*. 2018;65(2):163-168. doi:10.1002/jmrs.275.
12. Tam YH, Wong YS, Chan KW, Pang KK, Tsui SY, Mou JW, et al. Simple maneuvers to reduce the incidence of false-negative findings for contralateral patent processus vaginalis during laparoscopic hernia repair in children: a comparative study between 2 cohorts. *J Pediatr Surg*. 2013;48(4): 826-829. doi: 10.1016/j.jpedsurg.2012.07.043.
13. Palomino Salas A, Ornelas Cortinas GE, Guillén Gutiérrez CY. Hernia complicada en el canal de Nuck en el puerperio inmediato. *An Radiol Mex*. 2022; 21: 68-73. doi.org/10.24875/arm.20000224.
14. Garteiz Martínez D, Nieto González SE, Bravo Torrelanca C, Sánchez AW. Quiste del canal de Nuck asociado con hernia inguinal recurrente. *Ginecol Obstet Mex*. 2013; 81: 52-56.
15. Jarquín Arremilla A, García Espinoza AJ, Tafoya Ramírez F, Lechuga García AN. Quiste de Nuck, una entidad clínica inusual. Informe de un caso y revisión de la literatura. *Cir Gen*. 2018; 40(1): 38-42.

CTA findings in chronic coarctation of the aorta

Dennis C. Nelson-Rubio¹ * and J. Miguel Gomez-Torres² 

¹Department of Radiology, Centro Medico Pensiones; ²Department of Computed Tomography, Clinica de Merida. Merida, Yucatan, Mexico

Case 1 is a 17-year-old male diagnosed with coarctation of the aorta (CoA) at birth. In 2023, he presented claudication of the lower limbs after mild exertion without cyanosis. In Figure 1A, computed tomography angiography (CTA) of the aorta shows coarctation of

the descending aorta. There is anastomosis of the internal mammary artery with the inferior epigastric arteries.

Case 2 is a 21-year-old male diagnosed with CoA 15 years ago. He returned in 2022 with acropauquia,

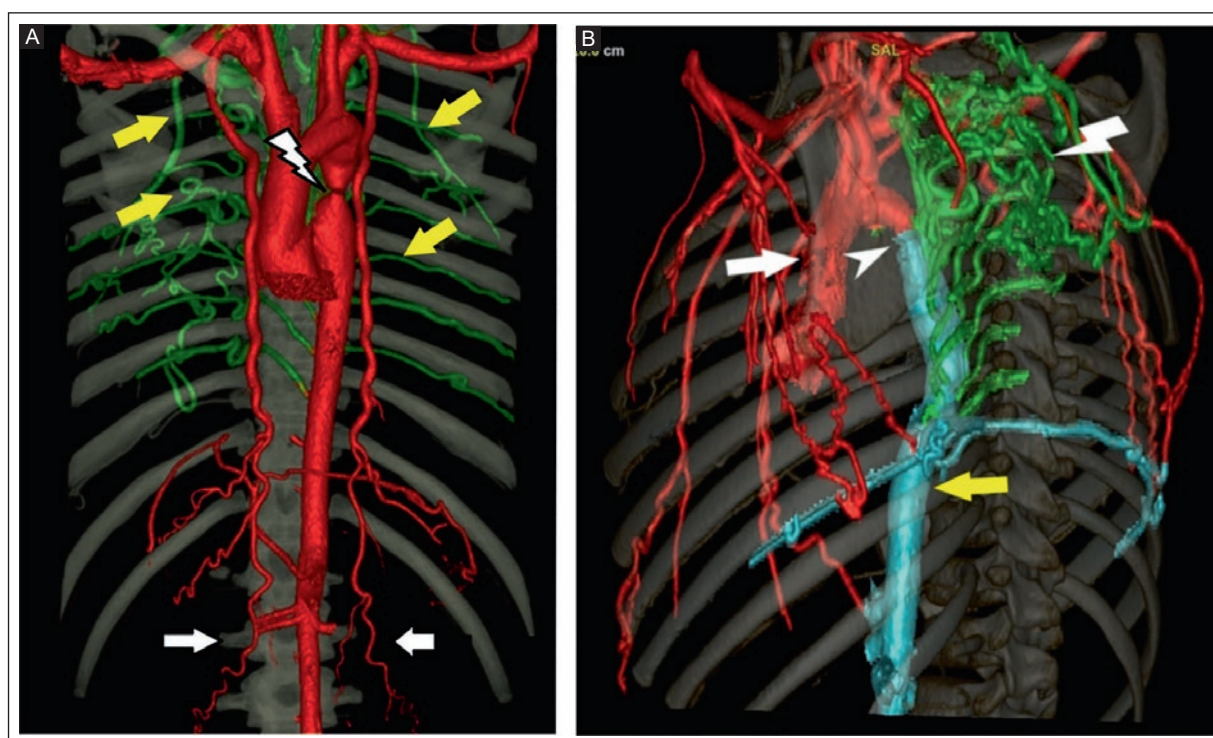


Figure 1. A: a segmented 3D reconstructed aortic CTA of a 17-year-old male showing CoA (lightning bolt) and anastomosis of the inferior epigastric arteries with the mammary arteries (white arrows). The posterior collateral vessels from the superior to the inferior aorta (yellow arrows) bypass the coarctation. **B:** a segmented 3D reconstructed aortic CTA of a 21-year-old male. Pre-coarctation aorta in red (white arrow), CoA (arrowhead), post-coarctation aorta in blue (yellow arrow), collateral vessels in green (lightning bolt) bypassing the coarctation from the pre-coarctation to the post-coarctation aorta.

CoA: coarctation of the aorta; CTA: computed tomography angiography.

*Corresponding author:

Dennis C. Nelson-Rubio
E-mail: dnelsonr@hotmail.com

Received for publication: 06-01-2024

Accepted for publication: 14-01-2024

DOI: 10.24875/JMeXFRI.M24000068

Available online: 22-03-2024

J Mex Fed Radiol Imaging. 2024;3(1):66-68

www.JMeXFRI.com

2696-8444 / © 2024 Federación Mexicana de Radiología e Imagen, A.C. Published by Permanyer. This is an open access article under the CC BY-NC-ND (<https://creativecommons.org/licenses/by-nc-nd/4.0/>).

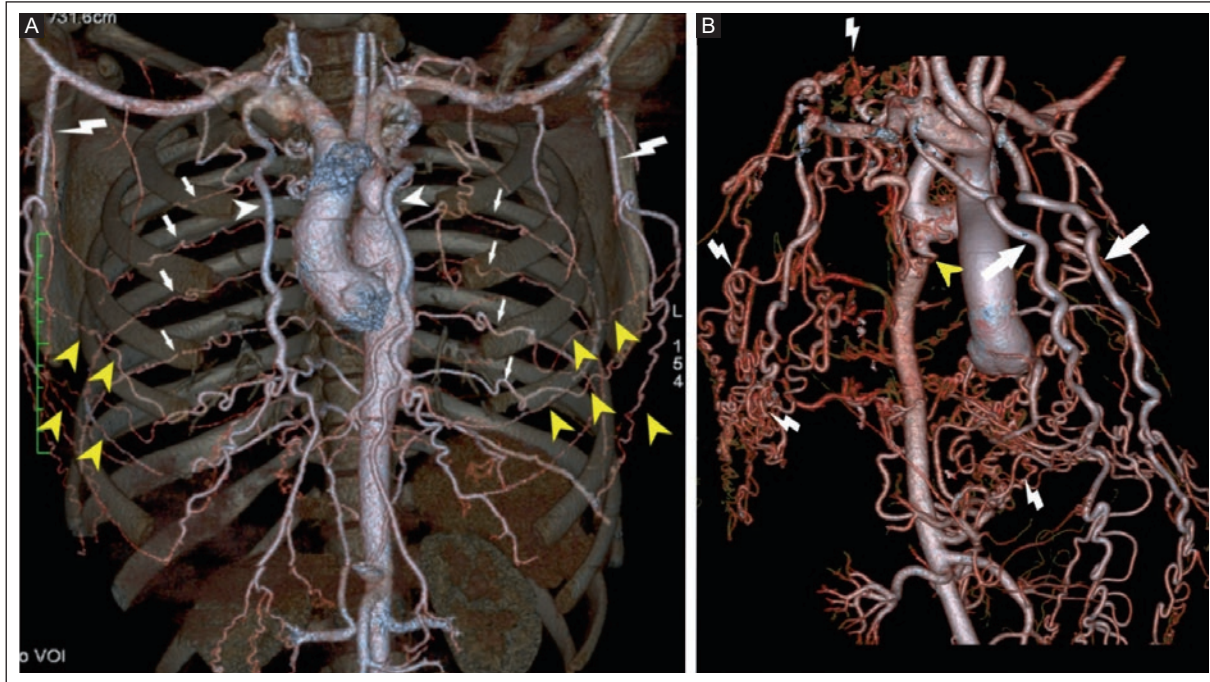


Figure 2. A: a segmented 3D reconstructed aortic CTA of an 18-year-old female. There is dilation of the intercostal arteries (arrows), the mammary arteries (arrowheads), and the axillary arteries (lightning bolts), with collateral vessels (yellow arrowheads) from the mammary and axillary arteries to the intercostal arteries. **B:** a segmented 3D reconstructed aortic CTA of a 20-year-old male. Re-stenosis of the CoA (yellow arrowhead), dilation of the mammary arteries (arrows), and numerous anterior and posterior collateral vessels (lightning bolts). CoA: coarctation of the aorta; CTA: computed tomography angiography.

dyspnea, and fatigue after mild physical activity. Figure 1B, the aortic CTA, shows many posterior collateral vessels connecting the pre-coarctation aorta to the post-coarctation aorta.

Case 3 is an 18-year-old female with previously undiagnosed CoA. In 2023, she presented low body weight and short height for her age. Aortic CTA in Figure 2A shows CoA with collateral circulation from both axillary arteries to the intercostal arteries.

Case 4 is a 20-year-old male with CoA diagnosed at birth. He was treated with balloon angioplasty. Aortic CTA in Figure 2B shows re-stenosis of the CoA with extensive anterior and posterior collateral vessels.

CoA is a congenital localized narrowing of the aortic lumen. If left untreated, numerous arterial collaterals that compensate for the lack of flow to the distal aorta can develop¹. These collateral vessels can make treatment of the coarctation stenosis difficult and less effective. Therefore, early diagnosis and treatment and correct identification of collateral vessels during follow-up are important². There does not appear to be an increased risk of coronary artery disease in adult patients with CoA³.

Acknowledgments

The authors thank Professor Ana M. Contreras-Navarro for her guidance in preparing and writing this scientific paper.

Funding

This paper received no external funding.

Conflicts of interest

The authors declare no conflicts of interest.

Ethical disclosures

Protection of individuals. This study complied with the Declaration of Helsinki (1964) and subsequent amendments.

Data confidentiality. The authors declare they followed their center's protocol for sharing patient data.

Right to privacy and informed consent. Informed consent was not required to analyze and publish routinely acquired clinical and imaging data.

Use of artificial intelligence. The authors state that they did not use generative artificial intelligence in preparing this manuscript or creating figures or figure legends.

REFERENCES

1. Leo I, Sabatino J, Avesani M, Moscatelli S, Bianco F, Borrelli N, et al. On Behalf of the Working Group on Congenital Heart Disease Cardiovascular Prevention in Pediatric Age of the Italian Society of Cardiology Sic. Non-Invasive Imaging Assessment in Patients with Aortic Coarctation: A Contemporary Review. *J Clin Med.* 2023;13(1):28. doi: 10.3390/jcm13010028.
2. Haramati LB, Glickstein JS, Issenberg HJ, Haramati N, Crooke GA. MR Imaging and CT of Vascular Anomalies and Connections in Patients with Congenital Heart Disease: Significance in Surgical Planning. *RadioGraphics.* 2002;22(2):337–349. doi:10.1148/radiographics.22.2.g02mr09337.
3. Egbe AC, Rihal CS, Thomas A, Boler A, Mehra N, Andersen K, et al. Coronary Artery Disease in Adults With Coarctation of Aorta: Incidence, Risk Factors, and Outcomes. *J Am Heart Assoc.* 2019;8(12):e012056. doi:10.1161/JAHA.119.012056.